Theoretical study on the f–f transition intensities of lanthanide trihalide systems

A Dissertation Submitted to Keio University

in Partial Fulfillment of the Requirement

for the Degree of Doctor of Philosophy

March 2011

Miho HATANAKA

Acknowledgements

The study presented in this dissertation is the summary of the author's works at the Prof. Yabushita laboratory in the School of Fundamental Science and Technology, Graduate School of Keio University.

First of all, the author would like to extend her cordial gratitude to Professor Satoshi Yabushita for his kind guidance, precise discussion and continuing support during the research activities.

Secondly, the author would like to acknowledge Professor Masahiko Hada, Professor Tetsuhiko Isobe, Professor Atsushi Nakajima and Professor Naoki Yoshioka for their constructive criticism to this dissertation.

Thirdly, the author would like to express her appreciation to Dr. Michihiko Sugawara, Dr. Masoto Morita, Dr. Tomoko Kinoshita and Ms. Satomi Kowashi for their kind discussion and friendly talking.

The author would like to acknowledge the Hayashi Memorial Foundation for Female Natural Scientists for supporting her research activities.

Lastly, the author would like to express her heartfelt thanks to all the people who have supported her and her research activities.

Miho Hatanaka

Keio University, Yokohama
February 14, 2011

Contents

Chapter 1

General Introduction

1.1. Computational Simulation as Theoretical Experiment

To predict and control natural phenomena is an ultimate aim of science. However, chemistry is traditionally a science developed by the accumulation of experience and experimental results, and predictions could be proposed only by experimental rules for a long time. Theoretical chemistry is one of the methods to be able to predict natural phenomena with computer simulation. This method has mainly two advantages. One is to be able to predict natural phenomena safely and inexpensively even if the experimental condition is too hard or appurtenances of experiments are too expensive. The other is to be able to observe invisible properties from experiments.

These predictions and analyses can be obtained by the wavefunctions, which can be obtained by solving the Schrödinger equation for the target systems. However, according to Dr. P. A. M. Dirac [1], '*The underlying physical laws necessary for the*

mathematical theory of a large part of physics and the whole of chemistry are thus completely known, and the difficulty is only that the exact application of these laws leads to equations much too complicated to be soluble.' To resolve this grave dilemma, many theoretical chemists have made a great effort to solve the Schrödinger equation using adequate approximations and algorithms. Many theoretical analysis methods have been developed for us to predict natural phenomena and observe invisible properties. Even in the present day, there still are many problems that have not been resolved.

In this dissertation, the author focuses on photo-absorption and emission intensity of lanthanide systems, which are one of the most difficult systems to solve their Schrödinger equation exactly. Additionally, the origin of intensities is the property that cannot be observed with experiment. The author has developed a computational method to calculate intensities with reducing the amount of computational efforts and established methods of analysis of the origin of photo-absorption and emission intensities.

1.2. General Background of this Dissertation

Firstly, a brief introduction on chemical properties, especially optical properties, of lanthanide systems is given. Secondly, the chemical properties which should be contained in the *ab initio* calculations of these systems are explained.

1.2.1. Lanthanide Chemistry

Lanthanide systems have attracted increasing attention from their potential applications as various materials [2]-[4]: optical or magnetic devices, catalysts of chemical reactions, metal alloys for hydrogen storage and so on. The lanthanide series consist of the 14 elements with atomic number 58 through 71, from cerium to lutetium. They are contained in the f-block elements. All the electronic configurations of lanthanide trivalent ions are $1s^2 2s^2 2p^6 3s^2 3p^6 3d^{10} 4s^2 4p^6 4d^{10} 4f^N 5s^2 5p^6$ and only the number of 4f electrons *N* increases as the atomic number increases as shown in Table 1-1. The radial distributions of 4f, 5s, 5p, and 5d orbitals of praseodymium and europium trivalent ion (Pr^{3+} and Eu^{3+}) are shown in Figure 1-1. As is clear from Figure 1-1, open-shell 4f electrons are shielded by the closed-shell 5s and 5p electrons from outside. Therefore, the 4f electrons behave as core-like electrons and are affected little from surrounding environment. This is the most important point that determines the character of lanthanide systems.

Table 1-1 : Electronic configurations of lanthanide trivalent ions

Atomic Number	Name	Ln	Electronic configurations of neutral Ln	Number of 4f electrons of Ln^{3+}
58	Cerium	Ce	$1s^2\cdots4f^15s^25p^65d^16s^2$	1
59	Praseodymium	Pr	$1s^2\cdots4f^35s^25p^66s^2$	2
60	Neodymium	Nd	$1s^2\cdots4f^45s^25p^66s^2$	3
61	Promethium	Pm	$1s^2\cdots4f^55s^25p^66s^2$	4
62	Samarium	Sm	$1s^2\cdots4f^65s^25p^66s^2$	5
63	Europium	Eu	$1s^2\cdots4f^75s^25p^66s^2$	6
64	Gadolinium	Gd	$1s^2\cdots4f^75s^25p^65d^16s^2$	7
65	Terbium	Tb	$1s^2\cdots4f^95s^25p^66s^2$	8
66	Dysprosium	Dy	$1s^2\cdots4f^{10}5s^25p^66s^2$	9
67	Holmium	Ho	$1s^2\cdots4f^{11}5s^25p^66s^2$	10
68	Erbium	Er	$1s^2\cdots4f^{12}5s^25p^66s^2$	11
69	Thulium	Tm	$1s^2\cdots4f^{13}5s^25p^66s^2$	12
70	Ytterbium	Yb	$1s^2\cdots4f^{14}5s^25p^66s^2$	13
71	Lutetium	Lu	$1s^2\cdots4f^{14}5s^25p^65d^16s^2$	14

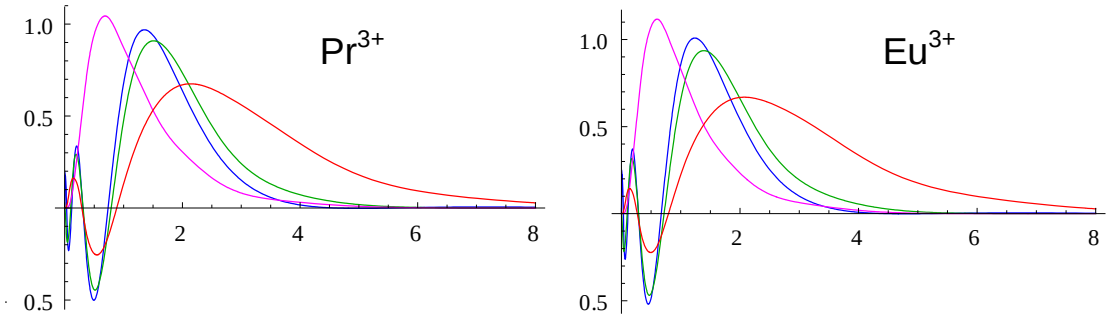

Figure 1-1 : Plots of the radial functions $rR(r)$ vs r (in a.u.) for Pr^{3+} and Eu^{3+}. Pink, blue, green, and red lines are those of 4f, 5s, 5p and 5d orbitals, respectively.

One of the characteristic properties of lanthanides is “lanthanide contraction” [5]. For each consecutive atom the nuclear charge increases by one unit, accompanied by a corresponding increase in the number of electrons present in the 4f orbitals surrounding the nucleus. The 4f electrons shield very imperfectly each other from the increased positive charge of the nucleus, so that the effective nuclear charge attracting each electron steadily increases through the lanthanide elements, resulting in successive reductions of the atomic and ionic radii. Therefore, it is generally observed in lanthanide systems that the distance between lanthanide and ligands and also the ionic radius decrease as the atomic number of lanthanide increases. The similarity in ionic radius between adjacent lanthanide elements makes it difficult to separate them from each other in naturally occurring ores and other mixtures.

Another character is similarity of chemical properties. Because 4f electrons cannot bind to ligands directly due to the small size, lanthanide complexes are usually held together by ionic bonds. This character causes the flexibility of the structures and the variety of coordination numbers of lanthanide complexes from 2 through 12, which is one of the reasons of difficulty in determination of the structures [5].

The last point to be emphasized here is the presence of unpaired 4f electrons. Due to the presence of unpaired electron spin, lanthanide systems have various spin multiplicities and are used extensively as magnetic materials. Additionally, the presence

of open-shell 4f electrons causes a number of $4f^N$ states whose absorption or emission wavelengths are present in the visible, near infrared, and near ultraviolet regions [5]. In recent years, these optical properties of lanthanide have been applied in multiple areas. However, their mechanisms have been discussed only on the base of the traditional crystal field theory, and they have not entirely been clarified. Therefore, the properties of electronic transitions between these $4f^N$ states are explained in the following sections.

1.2.2. f-f Transition

As mentioned in the previous section, lanthanide systems have a number of $4f^N$ states. Intra-$4f^N$ electronic transitions are called "f-f transitions" and used for many optical materials, such as lasers, fibers, optical displays, biosensors and so on [2]-[4]. The typical oscillator strengths of f-f transitions are as small as 10^{-6} because these are Laporte forbidden transitions. However, f-f transitions have useful properties for optics because the absorption and emission spectra have peaks in visible, near infrared and near ultraviolet regions and the peaks are sharp even in crystal fields because 4f electrons are affected little by surrounding environment due to the shielding effect of 5s and 5p electrons.

The oscillator strengths of f-f transitions have long been investigated with semi-empirical theory called the Judd-Ofelt theory [6],[7], whose idea will be explained

in the following sections. According to the recent review [8], this theory has been used in about 800 investigations to report intensities of lanthanide systems. Since this theory is based on the traditional crystal field theory and the technique of angular momentum coupling scheme, it can be considered that the essential properties of f-f transition usually come from the crystal field generated by the surrounding environment.

1.2.3. Hypersensitive Transition

As mentioned in the previous section, 4f electrons are affected little by surrounding environment because they are well shielded by the closed-shell 5s and 5p electrons from outside. Therefore, the crystal-field splittings are smaller than the spin-orbit (SO) splittings, and the electronic states of lanthanide trivalent ion (Ln^{3+}) in crystal-fields are usually similar to those of free Ln^{3+}.

In spite of the shielding effect, there are some exceptional f-f transitions whose oscillator strengths are very sensitive to a small change of surrounding environment. These transitions have been called “hypersensitive transitions” by Jørgensen and Judd [9] and have been extensively studied [8]. It is well known from previous experimental studies that the hypersensitive transitions obey the selection rules as $|\Delta J| \le 2$, $|\Delta L| \le 2$ and $\Delta S = 0$, and that their oscillator strengths are usually enhanced greatly compared with those of Ln^{3+} in aqueous solution. Especially, Gruen et al. [10],[11] observed that

the oscillator strengths of hypersensitive transitions in gaseous lanthanide trihalide (LnX_3) molecules were much larger than those of Ln^{3+} in solutions or crystals, though their wavelengths were not changed very much. Because the original Judd-Ofelt theory could not explain this phenomenon, several models were proposed for explanation of hypersensitivity. Among them, dynamic-coupling (DC) model [12]-[15] could explain the oscillator strengths of hypersensitive transitions in LnX_3 molecules qualitatively. However, their mechanisms have been discussed even in recent years and still competed with one another. One of the reasons why the comprehensive explanation for the origin of hypersensitive transitions has not been proposed is because all the previous theoretical studies were based on the semi-empirical models, which could contain only particular effects selectively and artificially in ad hoc manner. Therefore, if all the effects can be considered simultaneously, the comprehensive mechanism of hypersensitive transitions must be consolidated. For resolving such a problem, theoretical chemistry, especially "*ab initio* calculation", which can be carried out without empirical parameters, must be a powerful and trusted tool.

1.2.4. Difficulty of Ab Initio Calculations in Lanthanide Systems

In spite of the increasing needs for theoretical prediction and analyses of the origin of f-f transitions, especially of hypersensitive transitions, there were only several *ab initio*

studies about structure of LnX_3 [16]-[21] or f-f and f-d transitions [22],[23], and no studies about hypersensitive transitions. One of the reasons is the difficulty of *ab initio* electronic state calculations of lanthanide systems. Because several approximations are applied even in "*ab initio*" methods, adequate methods must be selected to reproduce the physical picture in each case. The author focuses on especially two points that must be considered in the calculation of $4f^N$ states of lanthanide systems.

Firstly, lanthanide atoms are heavy atoms. They cause the difficulty of *ab initio* calculations because the numbers of electrons are from 58 to 71, which are too many to be calculated directly, and the relativistic effects cannot be neglected [24]. These problems can be resolved by applying the relativistic effective core potential (RECP) methods [24], which replace the complicated effects of the core electrons with effective potentials, the so-called pseudopotentials. This method has two advantages. One is to be able to reduce the computational efforts by reducing the number of electrons and the basis set size. The other is to be able to include relativistic and other effects in the pseudopotentials. In addition, the spin-orbit term H_{SO}, which is a part of the relativistic effects, is added to the Hamiltonian to allow the mixing of different spin multiplicity configurations.

Secondly, 4f orbitals are quasi-degenerate even in crystal fields because 4f electrons are affected little from surrounding environment due to the shielding effect from outer

5s and 5p electrons [5]. Therefore, electronic correlation, especially static correlation, must be considered because $4f^N$ wavefunctions cannot be described well only with a small number of Slater determinants. To contain these effects into *ab initio* calculations effectively, the author selects the multi-reference spin-orbit configuration interaction (MRSOCI) calculation [25] with RECP method in this study.

1.3. Concrete Subjects of this Dissertation

As can be seen from the previous sections, there is a growing need for *ab initio* study about f-f transition intensities, especially for *ab initio* analyses about the origin of f-f intensities and hypersensitivity. In this study, the author aims at "the first" quantitative *ab initio* calculations of oscillator strengths of f-f transitions and at identifying the origin of hypersensitivity. The author focuses attention on the f-f transitions of LnX_3 molecules (Ln = Pr, Nd, Pm, Sm, Eu, Tb, Dy, Ho, Er, Tm; X = Cl, Br, I), whose oscillator strengths of hypersensitive transitions are much larger than those of Ln^{3+} in aquo. To contain both the relativistic and the electronic correlation effects effectively, the MRSOCI method are employed in this study.

However, when the author started this subject of research, their computational efforts were too demanding to compute oscillator strengths with the existing program, though the target systems are only four-atom molecules. To solve this problem, the author

coded and attached a new program to compute the transition density matrix with the graphical unitary group approach (GUGA) to the COLUMBUS program package and succeeded to calculate the oscillator strengths quantitatively by using this program.

In chapter 3, the author examines the previous hypothesizes about the origin of f-f hypersensitive transition intensities based on the MRSOCI calculation results. Firstly, the author focuses on the hypothesis considering the effect of molecular vibrations and f-d mixing, and refutes them. Additionally, the author decomposes the oscillator strengths of f-f transitions to clarify which configurations affect the intensities mostly and notices that the effect mentioned in the DC model has a dominant contribution to the f-f intensities.

To examine the effect considered in the DC model more closely, the author focuses two kinds of Judd-Ofelt intensity parameters τ_λ(ab) and τ_λ(dc) in chapter 4. If the oscillator strengths can be explained only by the DC model, the JO intensity parameters τ_λ(ab), which can be extracted from *ab initio* data, must show an essentially the same behavior as τ_λ(dc), which is derived from the DC model. The results suggest that the overall behaviors of τ_λ(ab) can be understood roughly by the DC model and the polarization shielding effect.

Finally, the author observes the spatial distribution functions of the transition densities and the transition dipole moments and gives a comprehensive explanation for

the origin of f-f hypersensitive transitions using the time-dependent and time-independent languages in chapter 5. Furthermore, the relative phase between the contributions considered in the JO theory and the DC model are examined and the contribution from ligand-to-metal charge transfer, which was neglected in previous models, is also clarified for the first time.

Chapter 2

Theoretical Background

In this chapter, the author presents the explanation on the theoretical ideas and methods used in this study. A brief history of investigations for f-f transition and hypersensitive transition intensities based on semi-empirical method is given in the section 2.1. After that, the *ab initio* calculation method of oscillator strengths is explained in section 2.2 and the algorithm to reduce computational efforts significantly is outlined in section 2.3.

2.1. Previous Theories for f-f Transition and Hypersensitivity

2.1.1. Judd-Ofelt theory

2.1.1.1 $4f^N$ Wavefunction and Dipole Moment Matrix Element

Judd [6] and independently Ofelt [7] presented treatises about the calculation method for Laporte forbidden f-f transition intensities of lanthanide systems with coupling scheme of angular momentum. The basic idea is that f-f transitions can be allowed

because of the mixing of opposite parity configurations, such as $4f^{N-1}5d$ or $4f^{N-1}g$, to $4f^N$ states due to the presence of odd parity crystal field generated by the point charges on ligands. Here, the author presents a brief review of the Judd-Ofelt coupling scheme.

Firstly, a $4f^N$ state is written by

$$|A\rangle = \sum_M a_M \left| l^N \psi J M \right\rangle, \tag{1}$$

where A is a crystal-field level, l^N is configuration, ψ is the additional quantum numbers that are necessary to define a level uniquely, J is the total angular momentum, M is the quantum number of the projection J_z of J, and a_M are coefficients arising from crystal field mixing.

When odd parity crystal field V_{odd} is presented, this $4f^N$ state are perturbed as

$$\begin{aligned} |B\rangle &= |A\rangle + \sum_K |K\rangle \frac{\langle K|V_{\text{odd}}|A\rangle}{E(A)-E(K)} \\ &= \sum_M a_M \left| l^N \psi J M \right\rangle + \sum_K b(n'l'\psi''J''M'') \left| l^{N-1}(n'l')^1 \psi'' J'' M'' \right\rangle \end{aligned}, \tag{2a}$$

$$b(n'l'\psi''J''M'') = \frac{\left\langle l^{N-1}(n'l')^1 \psi'' J'' M'' \middle| V_{\text{odd}} \middle| A \right\rangle}{E(\psi J) - E(n'l'\psi''J'')}, \tag{2b}$$

where $|K\rangle$ are the opposite parity intra-Ln excitation configurations, such as $4f^{N-1}5d$ or $4f^{N-1}g$. Here, odd parity crystal field V_{odd} is expressed as

$$V_{\text{odd}} = \sum_{k,q} A_{kq} \hat{\mathbf{D}}_q^{(k)} = \sum_{k,q} A_{kq} \sum_j r_j^k Y_{kq}\left(\theta_j, \varphi_j\right), \tag{3}$$

where $\hat{\mathbf{D}}_q^{(k)}$ is tensor of odd rank k with components q ($q = 0, \pm 1, \cdots, \pm k$), A_{kq} is crystal-field coefficient, r_j^k is radial distance of electron j (to the k-th power) from the

lanthanide nucleus, and $Y_{kq}(\theta_j, \varphi_j)$ is a spherical tensor operator of rank *k* containing the angular coordinates of electron *j*.

Secondly, the transition dipole moment between perturbed wavefunctions *B* and *B'* can be written as

$$\begin{aligned}
&\left\langle B\middle|\hat{\mathbf{D}}^{(1)}_{\rho}\middle|B'\right\rangle \\
&= \sum_{M}\sum_{M'}\left\langle l^N\psi JM\middle|a_M\hat{\mathbf{D}}^{(1)}_{\rho}a'_{M'}\middle|l^N\psi' J'M'\right\rangle \\
&\quad + \sum_{K}\sum_{M}\sum_{M'}\left\langle l^N\psi JM\middle|a_M\hat{\mathbf{D}}^{(1)}_{\rho}b'(l'\psi''J''M'')\middle|l^{N-1}l'^1\psi''J''M''\right\rangle \\
&\quad + \sum_{K}\sum_{M}\sum_{M'}\left\langle l^{N-1}l'^1\psi''J''M''\middle|b(l'\psi''J''M'')\hat{\mathbf{D}}^{(1)}_{\rho}a'_{M'}\middle|l^N\psi' J'M'\right\rangle \\
&\quad + \sum_{K}\sum_{K'}\left\langle l^{N-1}l'^1\psi''J''M''\middle|b(l'\psi''J''M'')\hat{\mathbf{D}}^{(1)}_{\rho}b'(l'\psi''J''M'')\middle|l^{N-1}l'^1\psi''J''M''\right\rangle
\end{aligned} \tag{4}$$

Here, the first and the fourth terms cancel because they are the matrix elements between the same parity configurations. Thus, eq.(4) can be rewritten as

$$\begin{aligned}
&\left\langle B\middle|\hat{\mathbf{D}}^{(1)}_{\rho}\middle|B'\right\rangle \\
&= \sum_{K}\sum_{M}\sum_{M'}\sum_{k,q}a_M a'_{M'}A_{kq}\frac{\left\langle l^N\psi JM\middle|\hat{\mathbf{D}}^{(1)}_{\rho}\middle|l^{N-1}l'^1\psi''J''M''\right\rangle\left\langle l^{N-1}l'^1\psi''J''M''\middle|\hat{\mathbf{D}}^{(k)}_{q}\middle|l^N\psi' J'M'\right\rangle}{E(\psi' J') - E(n'l'\psi''J'')} \\
&+ \sum_{K}\sum_{M}\sum_{M'}\sum_{k,q}a_M a'_{M'}A_{kq}\frac{\left\langle l^N\psi JM\middle|\hat{\mathbf{D}}^{(k)}_{q}\middle|l^{N-1}l'^1\psi''J''M''\right\rangle\left\langle l^{N-1}l'^1\psi''J''M''\middle|\hat{\mathbf{D}}^{(1)}_{\rho}\middle|l^N\psi' J'M'\right\rangle}{E(\psi J) - E(n'l'\psi''J'')}
\end{aligned} \tag{5}$$

It is not easy to calculate eq.(5) which contains the summations: *M*, *M'*, *k*, *q*, *ψ''*, *J''*, *M''*, *n'*, *l'*. Therefore, several approximations are applied to evaluate eq.(5) in the following section.

2.1.1.2. Approximations

The main suggestion made by Judd and Ofelt is that the presence of $\left|l^{N-1}(n'l')^1\psi''J''M''\right\rangle\left\langle l^{N-1}(n'l')^1\psi''J''M''\right|$ makes it possible to apply "the closure procedure". It is a scheme of approximation that perturbing excitation configurations are regarded as degenerate. If the excitation energy of each perturbing configuration $l^{N-1}(n'l')$ can be regarded much larger than that of l^N, following two approximations can be applied: (i) the excitation energy of perturbing configuration $E(n'l'\psi''J'')$ is invariant with respect to n', l', ψ'' and J'' and (ii) the energy denominators of eq.(5) $E(\psi J)$-$E(n'l'\psi''J'')$ and $E(\psi'J')$-$E(n'l'\psi''J'')$ are replaced by the single energy difference $\Delta(n'l')$.

As the result of these approximations, eq. (5) can be expressed as

$$\left\langle B\left|\hat{\mathbf{D}}^{(1)}_{\rho}\right|B'\right\rangle = \sum_{k,q}\sum_{\lambda=even}(2\lambda+1)(-1)^{q+\rho}A_{kq}\begin{pmatrix}1 & \lambda & k\\ \rho & -q-\rho & q\end{pmatrix}\left\langle A\left|\hat{\mathbf{U}}^{(\lambda)}_{q+\rho}\right|A'\right\rangle\Xi(k,\lambda), \qquad (6)$$

where A_{kq} is the crystal-field coefficient as already defined in eq. (3), and

$$\Xi(k,\lambda) = 2\sum_{n',l'}(2l+1)(2l'+1)(-1)^{l+l'}\begin{Bmatrix}1 & \lambda & k\\ l & l' & l\end{Bmatrix}\begin{pmatrix}l & 1 & l'\\ 0 & 0 & 0\end{pmatrix}\begin{pmatrix}l & k & l'\\ 0 & 0 & 0\end{pmatrix}\frac{\left\langle l\left|\hat{\mathbf{r}}\right|l'\right\rangle\left\langle l\left|\hat{\mathbf{r}}^{k}\right|l'\right\rangle}{\Delta(n'l')}. \qquad (7)$$

The summation in eq. (7) runs over all values on n' and l' consistent with $l^{N-1}(n'l')$ being an excited configuration.

The matrix element in eq. (6) can be expressed as a sum over reduced matrix elements involving Russell-Saunders coupled states:

$$\left\langle A\left|\hat{\mathbf{U}}^{(\lambda)}_{q+\rho}\right|A'\right\rangle = \sum_{M,M'} a_M a'_{M'} \left\langle l^N \psi J M \left|\mathbf{U}^{(\lambda)}_{q+\rho}\right| l^N \psi' J' M' \right\rangle . \tag{8}$$

Application of the Wigner-Eckart theorem, which is one of the standard tensor operator techniques, results in

$$\begin{aligned} &\sum_{M,M'} a_M a'_{M'} \left\langle l^N \psi\, J\, M \left|\mathbf{U}^{(\lambda)}_{q+\rho}\right| l^N \psi' J' M' \right\rangle \\ &= \sum_{M,M'} a_M a'_{M'} (-1)^{J-M} \begin{pmatrix} J & \lambda & J' \\ -M & q+\rho & M' \end{pmatrix} \left\langle l^N \psi\, J \left\| \mathbf{U}^{(\lambda)} \right\| l^N \psi' J' \right\rangle . \end{aligned} \tag{9}$$

It is possible to carry out expansions of the type

$$\left| l^N \psi\, J \right\rangle = \sum_{\tau,S,L} h(\tau\, S\, L) \left| l^N \tau\, S\, L\, J \right\rangle . \tag{10}$$

where $h(\tau\, S\, L)$ are the expansion coefficients to express the reduced matrix element as

$$\begin{aligned} &\left\langle l^N \psi\, J \left\| \mathbf{U}^{(\lambda)} \right\| l^N \psi' J' \right\rangle = \left\langle l^N \tau\, S\, L\, J \left\| \mathbf{U}^{(\lambda)} \right\| l^N \tau' S' L' J' \right\rangle \\ &= (-1)^{S+L'+J+\lambda} [(2J+1)(2J'+1)]^{1/2} \begin{Bmatrix} L & \lambda & L' \\ J' & S & J \end{Bmatrix} \left\langle l^N \tau\, S\, L \left\| \mathbf{U}^{(\lambda)} \right\| l^N \tau' S' L' \right\rangle . \end{aligned} \tag{11}$$

The doubly reduced matrix elements $\left\langle l^N \tau\, S\, L \left\| \mathbf{U}^{(\lambda)} \right\| l^N \tau' S' L' \right\rangle$ have been tabulated by Nielson and Koster. Finally, the induced electric dipole matrix element between two states *B* and *B'* of the f^N configuration in eq. (5) can be written as

$$\begin{aligned} &\left\langle B \left| \mathbf{D}^{(1)}_{\rho} \right| B' \right\rangle \\ &= \sum_{M} \sum_{M'} a_M a'_{M'} \sum_{\tau,S,L} \sum_{\tau',S',L'} h(\tau\, S\, L) h'(\tau' S' L') \sum_{k,q} \sum_{\lambda=even} A_{kq} \Xi(k,\lambda) (-1)^{q+\rho+J-M+S+L'+J+\lambda} \\ &\times \begin{pmatrix} 1 & \lambda & k \\ \rho & -q-\rho & q \end{pmatrix} \begin{pmatrix} J & \lambda & J' \\ -M & q+\rho & M' \end{pmatrix} \begin{Bmatrix} L & \lambda & L' \\ J' & S & J \end{Bmatrix} (2\lambda+1)[(2J+1)(2J'+1)]^{1/2} \\ &\times (2\lambda+1)[(2J+1)(2J'+1)]^{1/2} \left\langle l^N \tau\, S\, L \left\| \mathbf{U}^{(\lambda)} \right\| l^N \tau' S' L' \right\rangle . \end{aligned} \tag{12}$$

2.1.1.3. Selection Rule for Induced Electric Dipole Transition

From the triangle conditions of 3-*j* symbol and 6-*j* symbol in eq. (7) and eq.(12), several selection rules for induced electric dipole transitions can be derived as follows:

(a) λ = 0, 2, 4, 6. According to the triangle condition for the triad indicated in underlined quantum numbers in $\begin{Bmatrix} 1 & \underline{\lambda} & k \\ \underline{l} & l' & \underline{l} \end{Bmatrix}$ in eq.(7), one has $|l-l'| \le \lambda \le |l+l'|$. The selection rule follows directly from the fact that λ is even and l = 3.

(b) k = 1, 3, 5, 7. According to the triangle condition for the triad indicated in underlined quantum numbers in $\begin{Bmatrix} \underline{1} & \underline{\lambda} & \underline{k} \\ l & l' & l \end{Bmatrix}$, one has $|\lambda - 1| \le k \le |\lambda + 1|$. Because k is odd and λ is even, it follows that $k = |\lambda \pm 1|$.

(c) $\Delta l = \pm 1$. According to the triangle condition for the triad indicated in underlined quantum numbers in $\begin{Bmatrix} \underline{1} & \lambda & k \\ l & \underline{l'} & \underline{l} \end{Bmatrix}$, one has $|l-1| \le l' \le |l+1|$. The perturbing configurations are thus of the type $4f^{N-1}n'd^1$ and $4f^{N-1}n'g^1$.

(d) $\Delta S = 0$, because both the crystal-field Hamiltonian and the electric dipole operator do not act on the spin part of the wavefunctions.

(e) $|\Delta J| \le \lambda \le J + J'$. This follows directly from the triangle condition in underlined quantum numbers in $\begin{Bmatrix} L & \underline{\lambda} & L' \\ \underline{J'} & S & \underline{J} \end{Bmatrix}$. Moreover, if $J = J' = 0$, the selection rule simplifies to $|\Delta J|$ = 0, 2, 4, 6. In other words, transitions with $J = 0 \rightarrow J' = 0$ are forbidden.

Because λ is even, transitions with $|\Delta J|$ = odd are forbidden in principle.

(f) $|\Delta L| \le \lambda \le L + L'$. This can be found from the condition for $\begin{Bmatrix} L & \lambda & L' \\ J' & S & J \end{Bmatrix}$. Because $\lambda \le 6$, the selection rule can be rewritten as $|\Delta L| \le 6$.

(g) $\Delta M = M' - M = -(q + \rho)$. The selection rule on M is derived from $\begin{pmatrix} J & \lambda & J' \\ -M & q+\rho & M' \end{pmatrix}$ in eq.(12).

It should be noted that the selection rules on ΔL and ΔS are only applicable in the Russell-Saunders coupling scheme. These selection rules can be relaxed because L and S are not good quantum numbers. Although J is a good quantum numbers, the selection rules on ΔJ may be relaxed by J-mixing, which is a weak effect. The selection rule on ΔM depends on the point group symmetry of the lanthanide site. Additionally, in the photo-absorption and emission spectra we can observe peaks caused by transitions that do not satisfy the above selection rules because there are magnetic dipole transitions whose selection rules are different from induced electric dipole transitions.

2.1.1.4. Oscillator Strength and Judd-Ofelt Intensity Parameters

The calculated oscillator strengths of a single spectral line is

$$P = \frac{4\pi m_e c}{\hbar} \Delta E \left| \left\langle B \left| \hat{\mathbf{D}}_{\rho}^{(1)} \right| B' \right\rangle \right|^2, \qquad (13)$$

where m_e, c, $\hbar$, ΔE are the electron mass, the light speed, the reduced Plank constant,

the excitation energy, respectively. Now, by summing over all crystal-field split levels of the ground state and over all those of the excited state, the oscillator strengths between initial and final multiplets can be written as follows,

$$f(\,^{S+1}L_J \rightarrow {}^{S'+1}L'_{J'}) = \frac{\Delta E}{2J+1}\sum_{\lambda=2,4,6}\tau_\lambda \left|\left\langle S\,L\,J\left\|\mathbf{U}^{(\lambda)}\right\|S'L'J'\right\rangle\right|^2 . \qquad (14)$$

Here, τ_λ (λ =2, 4, 6) are adjustable parameters called Judd-Ofelt intensity parameters, and can be expressed as

$$\tau_\lambda = \frac{4\pi m_e c\chi_{\mathrm{ed}}}{3\hbar}(2\lambda+1)\sum_k (2k+1)^{-1}\sum_q \left|A_{kq}\right|^2 \Xi^2(k,\lambda), \qquad (15)$$

where, χ_{ed} is the Lorentz field correction, whose value is unity in vapor. Because the reduced matrix elements $\left\langle S\,L\,J\left\|\mathbf{U}^{(\lambda)}\right\|S'L'J'\right\rangle$ can be calculated if the free-ion wavefunctions are available, the τ_λ parameters are determined semi-empirically from the experimental data. All the f-f transition oscillator strengths in a lanthanide system can be evaluated by using only three JO intensity parameters, because JO parameters are independent of excited levels. Oscillator strengths of many lanthanide systems have been successfully explained by the Judd-Ofelt theory.

However, there are still problems of so-called hypersensitive transition intensities. As long as the JO intensity parameters are treated as adjustable parameters obtained from experimental data, the JO theory gives good agreement between experimental and calculated dipole strengths for hypersensitive transitions. However, the original JO theory cannot give a theoretical explanation for the hypersensitivity effect. If the JO

parameters of LnX_3 molecules are evaluated with *ab initio* methods in terms of eq. (15), they are underestimated notably compared to those from experimental data [10],[11].

2.1.2. Other Models for Explanation of Hypersensitivity

To solve this problem, several theoretical models based on the original JO theory were proposed. One of them is hypothesis that hypersensitive transitions are not induced electric dipole transitions but quadrupole ones. As have already mentioned in the previous section 1.2.3, the hypersensitive transitions obey the selection rules as $|\Delta J| \le 2$, $|\Delta L| \le 2$ and $\Delta S = 0$, which are the same as those of a pure quadrupole transition. However, calculations have revealed that the intensities of hypersensitive transitions are several orders of magnitude too large for these transitions to have a quadrupole character [9].

Judd noticed that the matrix elements of $\mathbf{U}^{(2)}$ in eq.(14) were large for hypersensitive transitions and that the τ_2 parameters were sensitive to a small change of surrounding environment. Later, Judd included the crystal-field parameters in the expression for τ_2, and argued that the hypersensitivities occurred in certain limited point groups, such as C_s, C_1, C_2, C_3, C_4, C_6, C_{2v}, C_{3v}, C_{4v} and C_{6v} [26]. This theory could be confirmed by several experimental results [26],[27]. However, there are exceptions to the theory. The most significant one is the gaseous LnX_3 molecules [10],[11] mentioned above. They

have D_{3h} symmetry and notably large oscillator strengths for hypersensitive transitions. Therefore it cannot be the whole explanation although this theory can explain some aspects of hypersensitivity.

To explain the great enhancement of the oscillator strengths of hypersensitive transitions in gaseous LnX_3 systems, Gruen et al. [11] examined a number of mechanisms and explained that the hypersensitivity was attributable to the molecular vibration. The symmetries of these molecules can be lowered effectively because the frequencies of their out-of-plane bending vibrations are very small and the oscillator strengths were measured under the high temperature condition about 1000 K. Henrie et al. [28] explained their large oscillator strengths by means of a vibronic mechanism with the inclusion of covalency between lanthanide and ligands. However, the vibronic mechanism was criticized by many authors [29].

The covalency model mentioned above is one of the proposed models to explain the hypersensitivity. If the charge-transfer character is important in f-f intensities, the hypersensitivity to the surrounding ligands is understandable because the energies and intensities of the charge-transfer transitions are very sensitive to the kind of ligands and metals. Henrie et al. [30] modified the Judd-Ofelt theory by including charge-transfer states in addition to the opposite parity states $4f^{N-1}5d^1$. However, this mechanism was also criticized [14],[29].

2.1.3. Dynamic-Coupling Model

As shown in the previous sections, there had not been a theoretical model that could explain successfully the hypersensitivity. However, Mason and Peacock *et al*. succeeded in explaining the hypersensitive transition intensities of LnX_3 molecules in vapor phase with "dynamic-coupling model" [12]-[15], which was originally proposed in the theory of optical rotation [31],[32].

In what follows, a simple explanation of this model is provided by taking LnX_3 molecules as examples. Let put the Ln^{3+} cation on the origin and consider one of f electrons whose position vector is $\mathbf{r} = (x, y, z)$. The electron is under the influence of the static crystal field due to the three ligands X^-. If the molecule is put in an oscillating electric field, the electron receives additional perturbation fields, which contain not only the external electric field but also the newly created induced dipoles on the ligands. The latter field can act as a strong time-dependent crystal field, in modern terminology, an inhomogeneous near field.

The expression of such a crystal field due to the induced dipoles is related to the crystal field generated by the point charges q on the ligands. The latter field can be written as follows,

$$V_{\mathrm{CF}}^{q}(\mathbf{r}) = \frac{q}{4\pi\varepsilon_0}\sum_i \frac{1}{r_i} = \frac{q}{4\pi\varepsilon_0}\sum_i \left\{(x-a_i)^2 + (y-b_i)^2 + (z-c_i)^2\right\}^{-1/2} \quad , \tag{16}$$

where (a_i, b_i, c_i) is the coordinate of the i-th ligand, and $\mathbf{r}_i = (x-a_i, y-b_i, z-c_i)$ is

the relative vector from the ligand. Another crystal field generated by the identical induced dipole moment $\boldsymbol{\mu}_{\text{ind}}$ on all the ligands, that is, in the situation that all the dipole moments on the ligands are parallel with the same magnitude, is expressed as follows,

$$\begin{aligned} V_{\text{CF}}^{\mu}(\mathbf{r}) &= \frac{\boldsymbol{\mu}_{\text{ind}}}{4\pi\varepsilon_0}\cdot\sum_i \frac{\mathbf{r}_i}{r_i^3} \\ &= \frac{1}{4\pi\varepsilon_0}\sum_i \frac{\mu_x(x-a_i)+\mu_y(y-b_i)+\mu_z(z-c_i)}{r_i^3} \\ &= -\frac{\boldsymbol{\mu}_{\text{ind}}}{4\pi\varepsilon_0}\cdot\sum_i \nabla\frac{1}{r_i} \\ &= -\frac{\boldsymbol{\mu}_{\text{ind}}}{q}\cdot\nabla V_{\text{CF}}^{q}(\mathbf{r}) \quad . \end{aligned} \tag{17}$$

Therefore, the crystal field generated by the dipole moments $\boldsymbol{\mu}_{\text{ind}} = \alpha\mathbf{E}$ on the ligands induced by the oscillating external electric field **E** can be written as follows,

$$V_{\text{CF}}^{\mu}(\mathbf{r}) = -\frac{\alpha\mathbf{E}}{q}\cdot\nabla V_{\text{CF}}^{q}(\mathbf{r}) \quad , \tag{18}$$

where α is the polarizability of the ligand.

As seen in section 2.1.1, the crystal field V_{CF}^{q} generated by *n* ligands can be written in terms of spherical harmonics as follows,

$$V_{\text{CF}}^{q}(\mathbf{r}) = \sum_{k=0}^{\infty} r^k \sum_{m=-k}^{k} A_{km}^{q} Y_{km}(\theta,\phi) \, , \tag{19a}$$

$$A_{km}^{q} = \frac{4\pi}{2k+1}\frac{q}{R^{k+1}}\sum_{i=1}^{n} Y_{km}{}^{*}(\theta_i,\phi_i) \, , \tag{19b}$$

$$Y_{km}{}^{*}(\theta_i,\phi_i) = N_{km}\sin^{|m|}\theta_i \cdot \left(\frac{d}{d\cos\theta_i}\right)^{|m|} P_k(\cos\theta_i) e^{-im\phi_i} \, , \tag{19c}$$

where $P_k(\cos\theta_i)$ is the Legendre polynomial; and (r, θ, ϕ), (R, θ_i, ϕ_i) are the polar

coordinates of the f electron and ligands, respectively. In the case of LnX_3, which have D_{3h} structure, the three ligands are located on the polar coordinates (R, θ_i, ϕ_i) as

$$\left(R, \frac{\pi}{2}, 0\right), \left(R, \frac{\pi}{2}, \frac{2\pi}{3}\right), \left(R, \frac{\pi}{2}, \frac{4\pi}{3}\right), \tag{20}$$

and the crystal field acts on the central lanthanide only when the sum of the spherical harmonics in eq. (19b), which is expressed as

$$\begin{aligned} & Y_{km}^{*}\left(\tfrac{\pi}{2},0\right)+Y_{km}^{*}\left(\tfrac{\pi}{2},\tfrac{2\pi}{3}\right)+Y_{km}^{*}\left(\tfrac{\pi}{2},\tfrac{4\pi}{3}\right) \\ & = N_{km}\left(1+e^{-im\frac{2}{3}\pi}+e^{-im\frac{4}{3}\pi}\right)\left[\left(\frac{d}{d\cos\theta_i}\right)^{|m|}P_k(\cos\theta_i)\right]_{\theta_i=\frac{\pi}{2}}, \end{aligned} \tag{21}$$

has non-zero values. Here, k-$|m|$ must be even values because $\cos\theta_i$ is zero and $\left(\frac{d}{d\cos\theta_i}\right)^{|m|}P_k(\cos\theta_i)$ are polynomials of order k-$|m|$ and contain only even or odd terms. Additionally, $|m|$ must be 0, 3, 6,$\cdots$ due to the condition that $1+e^{-im\frac{2}{3}\pi}+e^{-im\frac{4}{3}\pi}$ have non-zero values. Therefore, the crystal field coefficients $A^q_{k|m|}$ in eq. (19b) are restricted to the following terms,

$$A^q_{00,}A^q_{20,}A^q_{33,}A^q_{40,}A^q_{53,}A^q_{60,}A^q_{66,}A^q_{73,}\cdots. \tag{22}$$

Since, only odd parity crystal field terms have non-zero matrix elements for the degenerated first-order perturbation treatment, the lowest order crystal field is A^q_{33} and it allows the f-d mixing in the Judd-Ofelt theory. When only the third-order terms are considered, the crystal field can be expressed as follows,

$$
\begin{aligned}
V_{\mathrm{CF}}^{q(3)}(\mathbf{r}) &= r^3\{A_{3,3}^q Y_{3,3}(\theta,\phi) + A_{3,-3}^q Y_{3,-3}(\theta,\phi)\} \\
&= C' r^3 \frac{q}{R^4}\sin^3\theta\{e^{3i\phi} + e^{-3i\phi}\} = Cr^3\frac{q}{R^4}\sin^3\theta\cos 3\phi \\
&= C\frac{q}{R^4}(x^3 - 3xy^2)\ .
\end{aligned}
\tag{23}
$$

In contract, the crystal field generated by the induced dipole moments on the ligands is the gradient of that in eq.(23). Therefore, it can be expressed as the second-order crystal field as follows,

$$
\begin{aligned}
V_{\mathrm{CF}}^{\mu}(\mathbf{r}) &= -\frac{\alpha}{q}\{E_x\cdot\frac{\partial}{\partial x} + E_y\cdot\frac{\partial}{\partial y} + E_z\cdot\frac{\partial}{\partial z}\}V_{\mathrm{CF}}^{q(3)}(\mathbf{r}) \\
&= -\frac{3\alpha C}{R^4}\{E_x\cdot(x^2 - y^2) - E_y\cdot 2xy\}\ .
\end{aligned}
\tag{24}
$$

where, E_x, E_y and E_z are the component of the oscillating electric field **E**. The two terms in Eq. (24) can be regarded respectively as the Coulombic interaction between the quadrupole component of x^2-y^2 on Ln and the induced dipole component x on the ligands, and the interaction between their components of xy and y, as schematically shown in Figure 2-1.

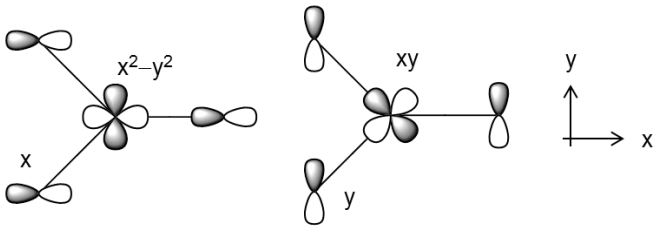

Figure 2-1. The non-zero Coulombic correlation between the metal ion quadrupole moments and the ligand dipole moments in D_{3h} LnX_3 molecules.

In the oscillating electric field, all the induced dipole moments are oriented to the same

direction as shown in Figure 2-1, and their directions are revised after a half cycle of the oscillation. Because the transition quadrupole moments between 4f orbitals of Ln are affected by the time-dependent crystal field Eq. (24), f-f transitions can be induced resonantly. This coupling between the transition quadrupole moment on the metal and the oscillating induced dipole moments on the ligands is called the dynamic-coupling (DC).

Additionally, the transition intensity can be considered from Fermi's Golden rule. According to this rule, the transition probability per unit time can be expressed as follows,

$$T^{IF} = \frac{2\pi}{\hbar}\left|\left\langle \Psi_F(\{\mathbf{r}_i\})\middle|H'\middle|\Psi_I(\{\mathbf{r}_i\})\right\rangle\right|^2 \delta(E_F - E_I - \hbar\omega)\,, \tag{25}$$

where *H'* is time-dependent perturbation Hamiltonian. In the DC model, the crystal field generated by the oscillating induced dipole moments on the ligands in eq. (24) is considered as the perturbing term and the transition probability can be written as follows,

$$\begin{aligned} T^{IF} &= \frac{2\pi}{\hbar}\left|\left\langle 4\mathrm{f}^{N,I}\middle|V_{\mathrm{CF}}^{\mu}(\mathbf{r})\middle|4\mathrm{f}^{N,F}\right\rangle\right|^2 \delta(E_F - E_I - \hbar\omega) \\ &= \frac{2\pi}{\hbar}\left(\frac{3\alpha C}{R^4}\right)^2 \left\{E_x{}^2\left\langle 4\mathrm{f}^{N,I}\middle|x^2 - y^2\middle|4\mathrm{f}^{N,F}\right\rangle^2 + E_y{}^2\left\langle 4\mathrm{f}^{N,I}\middle|2xy\middle|4\mathrm{f}^{N,F}\right\rangle^2\right\}\delta(E_F - E_I - \hbar\omega)\,. \end{aligned} \tag{26}$$

Mason *et al.* considered the mixing of intra-ligand excitation configurations into $4f^N$ states to include the effect of the induced-dipole moments on ligands [12]-[15]. $4f^N$ states in a two-system model of a lanthanide complex, neglecting overlap, is written by

$$\left|M_a L_g\right\rangle = \left|M_a L_g\right) + \sum_{c,e} \left|M_c L_e\right) \frac{\left(M_c L_e \left|V\right| M_a L_g\right)}{E_a + E_g - E_c - E_e},$$
$$\left|M_b L_g\right\rangle = \left|M_b L_g\right) + \sum_{c',e'} \left|M_{c'} L_{e'}\right) \frac{\left(M_{c'} L_{e'} \left|V\right| M_b L_g\right)}{E_b + E_g - E_{c'} - E_{e'}}, \quad (27)$$

where V is the electrostatic potential between charge distribution of the metal ion and that of each ligand, M_c and L_e are zero-order orthonormal eigenstates of metal ion and ligand subsystems. (where $c = a$, b and $e = g$ means the ground states of lanthanide and ligand sub-systems, respectively.) The electric transition dipole moment between the perturbed metal-ion states is represented by

$$\begin{aligned}
\left\langle M_a L_g \left|\mathbf{r}\right| M_b L_g\right\rangle &= \left\langle M_a L_g \left|\mathbf{r}(M) + \mathbf{r}(L)\right| M_b L_g\right\rangle \\
&= \sum_{c' \neq a} \left(M_a \left|\mathbf{r}(M)\right| M_{c'}\right) \frac{\left(M_{c'} L_g \left|V\right| M_b L_g\right)}{E_b - E_{c'}} \\
&+ \sum_{c \neq b} \left(M_c \left|\mathbf{r}(M)\right| M_b\right) \frac{\left(M_a L_g \left|V\right| M_c L_g\right)}{E_a - E_c} \\
&+ \sum_{e' \neq g} \left(L_g \left|\mathbf{r}(L)\right| L_{e'}\right) \frac{\left(M_a L_{e'} \left|V\right| M_b L_g\right)}{E_b + E_g - E_a - E_{e'}} \\
&+ \sum_{e \neq g} \left(L_e \left|\mathbf{r}(L)\right| L_g\right) \frac{\left(M_a L_g \left|V\right| M_b L_e\right)}{E_a + E_g - E_b - E_e},
\end{aligned} \quad (28)$$

where the first and second terms express intra-metal excitations considered in the original JO theory and the third and fourth terms express intra-ligand excitations introduced in the DC model. When the coulombic potential between non-overlapping charge distribution of the transitions $M_a \leftrightarrow M_b$ and $L_g \leftrightarrow L_e$, namely $\left(M_a L_{e'} \left|V\right| M_b L_g\right)$ and $\left(M_a L_g \left|V\right| M_b L_e\right)$ are expanded in terms of multipole expansion, the leading term is coulombic correlation of electric dipole moments in the ligand and

quadrupole moments in the metal ion. The f-f transition oscillator strengths derived from the third and fourth terms in eq.(28) can also be expressed in terms of JO type equation (eq.(14)). Only formula of intensity parameters τ_λ (λ = 2, 4, 6) is different as

$$\tau_\lambda = \frac{4\pi m_e c}{3\hbar}\chi(\lambda+1)\left\langle f\left\|C^{(\lambda)}\right\|f\right\rangle^2\left\langle 4f\left|r^2\right|4f\right\rangle^2\sum_{m=0}^{\lambda+1}(2-\delta_0^m)\left|\sum_L \alpha(L)R_L^{-\lambda-2}C_{-m}^{\lambda+1}(L)\right|^2, \quad (29)$$

where $\left\langle f\left\|C^{(\lambda)}\right\|f\right\rangle$ is the reduced matrix element of the λ-th rank Racah tensor connecting the f-orbital functions, $\left\langle 4f\left|r^2\right|4f\right\rangle$ is the squared radial expectation values of 4f orbital of Ln, $\alpha(L)$ is the mean polarizability of ligand L, R_L is the distance between Ln and ligand, $C_{-m}^{\lambda+1}(L)$ is the (λ+1)-th rank Racah tensor depending on the ligand structure. It should be noted that compared with the expression of the transition intensity by Fermi's Golden rule in (26), the JO intensity parameter τ_2, which is proportional to the TDM, also contains the square of quadrupole moments between 4f, that of the polarizability of the ligand $\alpha(L)$, and the minus eighth power of the distance between Ln and the ligands R_L^{-8}.

Here, as already pointed by Judd [26], it is noticed from the values for matrix elements of irreducible tensor operators [33]-[36] that the matrix elements of $\mathbf{U}^{(2)}$ have notably large values only in the hypersensitive transitions, whereas those of $\mathbf{U}^{(4)}$ and $\mathbf{U}^{(6)}$ are less sensitive to the transitions. An example of the matrix elements of $\mathbf{U}^{(\lambda)}$ for Pr^{3+} is shown in Table 2-1. As is clear from this table, matrix element of $\mathbf{U}^{(2)}$ has a large value only in

the hypersensitive transition ($^3H_4 \rightarrow {}^3F_2$), whereas those of $\mathbf{U}^{(4)}$ and $\mathbf{U}^{(6)}$ are less directly related to the hypersensitive transition.

Table 2-1: Matrix elements of $\mathbf{U}^{(\lambda)}$ (λ =2, 4, 6) for Pr^{3+} from $^3H_4$. [a]

States	$\mathbf{U}^{(2)}$	$\mathbf{U}^{(4)}$	$\mathbf{U}^{(6)}$
$^3H_5$	0.1095	0.2017	0.6109
$^3H_6$	0.0001	0.0330	0.1395
$\mathbf{^3F_2}$ [b]	**0.5089**	0.4032	0.1177
$^3F_3$	0.0654	0.3469	0.6983
$^3F_4$	0.0187	0.0500	0.4849
$^1G_4$	0.0012	0.0072	0.0266
$^1D_2$	0.0026	0.0170	0.0520
$^3P_0$	0	0.1728	0
$^3P_1$	0	0.1707	0
$^1I_6$	0.0093	0.0517	0.0239
$^3P_2$	~0	0.0362	0.1355
$^1S_0$	0	0.0070	0

[a] The values of matrix elements from Ref. [33].
[b] The final state of hypersensitive transition in Pr^{3+}.

From these reasons, it can be interpreted that the factors of hypersensitivity are concentrated on the term of λ = 2 in eq.(29), namely τ_2. In fact, the magnitude relation is $\tau_2 >> \tau_4, \tau_6$ in LnX_3 molecules in vapor phase [12] and these oscillator strengths can be evaluated only by the term of λ = 2 in eq.(14). Because of this reason, hypersensitive transitions have generally the largest oscillator strengths among possible final states, and are more sensitive to the change of τ_2 value than other transitions.

2.2. Theoretical Evaluation of Transition Intensity

2.2.1. Oscillator Strength and Transition Dipole Moment

When an atom or molecule absorbs light, a transition from one quantum state to another can occur, where the excitation energy corresponds to the wavelength of the light. The oscillator strength is a dimensionless quantity which expresses the strength of the transition from an initial state Ψ_I to a final state Ψ_F and is written as

$$f_{IF} = \frac{2m_e}{3\hbar^2}(E_F - E_I)\left\langle \Psi_I \left| \sum_{k=1}^{N} \mathbf{r}_k \right| \Psi_F \right\rangle . \tag{30}$$

Here, E_I and E_F are the electronic energies of Ψ_I and Ψ_F, respectively. $\left\langle \Psi_I \left| \sum_{k=1}^{N} \mathbf{r}_k \right| \Psi_F \right\rangle$ is the transition dipole moment from Ψ_I to Ψ_F, $\mathbf{r}_k$ is the position of k-th electron and N is the number of electrons in the system. In the second-quantized form [37], the transition dipole moment from a state Ψ_I to a state Ψ_F can be written as

$$\begin{aligned} \mathbf{M}_{IF} = \left\langle \Psi_I \left| \sum_{k=1}^{N} \mathbf{r}_k \right| \Psi_F \right\rangle &= \sum_{i,j}^{\mathrm{MO}} \left\langle \phi_i \left| \mathbf{r} \right| \phi_j \right\rangle \left\langle \Psi_I \left| \sum_{\sigma} a_{i\sigma}^{+} a_{j\sigma} \right| \Psi_F \right\rangle \\ &= \sum_{i,j}^{\mathrm{MO}} \left\langle \phi_i \left| \mathbf{r} \right| \phi_j \right\rangle \rho^{FI}(i,j) \quad . \end{aligned} \tag{31}$$

where ϕ is the molecular orbital (MO), $a_{i\sigma}^{+}$ and $a_{j\sigma}$ are the fermion creation and annihilation operators for an electron in MOs ϕ_i and ϕ_j respectively, with spin σ and $\rho^{FI}(i,j)$ is the transition density matrix element.

As mentioned before, the crystal field splittings of $4f^N$ states in lanthanide compounds are smaller than the spin-orbit (SO) splittings, and the electronic states of lanthanide

trivalent ion (Ln^{3+}) in crystal-fields are usually similar to those of free Ln^{3+}. Therefore, all the electronic states of LnX_3 correlated with ${}^{2S+1}L_J$ of Ln^{3+} are also named as ${}^{2S+1}L_J$. When the initial and final states are degenerate, the oscillator strength is defined by the sum over the final states and the average over the initial states. For example, the oscillator strength from initial multiplet ${}^{2S+1}L_J$ to final one ${}^{2S'+1}L'_{J'}$ can be expressed as

$$f({}^{2S+1}L_J \rightarrow {}^{2S'+1}L'_{J'}) = \frac{2m_e}{3\hbar^2(2J+1)} \sum_{v=1}^{2J+1} \sum_{w=1}^{2J'+1} (E_w - E_v) \langle v | \sum_{k=1}^{N} \mathbf{r}_k | w \rangle^2 , \qquad (32)$$

where *v* and *w* are all the states included in ${}^{2S+1}L_J$ and ${}^{2S'+1}L'_{J'}$, respectively.

2.3. Graphical Unitary Group Approach

2.3.1. Brief Survey

When *ab initio* calculations are carried out for large molecules with a high degree of accuracy, the computational efforts must increase. Therefore, many calculation methods and algorithms have been developed. “Graphical Unitary Group Approach (GUGA)” [38]-[40] is one of the methods which can reduce computational efforts significantly. In this section, the author makes a brief survey on the basis of GUGA. The relation between quantum mechanics and “the unitary group” is explained firstly, after that how to express electronic structure with the unitary group is mentioned. Finally, the method how to reduce computational efforts of configuration interaction calculation with

GUGA is explained.

2.3.1.1. Relation between Unitary Group and Quantum Mechanics

The unitary group $U(n)$ is the group containing all unitary matrices of order n. It is one of the continuous groups and Lie groups, whose elements can be generated by a finite set of operators, called "generators" [41]. The commutation properties of the generators of a Lie group define the group. In the case of the unitary group $U(n)$, the generators are a set of operators F_{ij} ($i, j = 0, 1, \cdots, n$) that satisfy the commutation relation as

$$F_{ij}F_{kl} - F_{kl}F_{ij} = \delta_{jk}F_{il} - \delta_{il}F_{kj} \quad . \tag{33}$$

Here, we focus attention on the spin-preserving substitution operator in the second-quantization method E_{ij}, which is expressed as

$$E_{ij} = \sum_{\sigma} a_{i\sigma}^{+} a_{j\sigma} = a_{i\alpha}^{+} a_{j\alpha} + a_{i\beta}^{+} a_{j\beta} \quad , \tag{34}$$

where $a_{i\sigma}^{+}$ and $a_{i\sigma}$ are the fermion creation and annihilation operators, respectively, for spatial orbital i with spin σ. It is well-known that these operators E_{ij} satisfy the commutation relation as

$$E_{ij}E_{kl} - E_{kl}E_{ij} = \delta_{jk}E_{il} - \delta_{il}E_{kj} \quad , \tag{35}$$

which is completely the same as that of generators F_{ij} of $U(n)$. This is the most important relation between the unitary group and quantum mechanics, especially electronic structure theory. In other words, it is considered that spin-free Hamiltonian in

the second-quantization, which is expressed as

$$H = \sum_{ij} \langle i|h|j \rangle E_{ij} + \frac{1}{2} \sum_{ijkl} \left\langle i(1)k(2) \left| \frac{1}{r_{12}} \right| j(1)l(2) \right\rangle e_{ij,kl} \quad , \tag{36}$$

can be represented with the generators of the unitary group. Because the Hamiltonian can be expressed with the generators of the unitary group, the wavefunctions, which are eigenfunctions of the Hamiltonian, must be expressed with the irreducible representation of this group. Therefore, we focus on irreducible representation of the unitary group in the following section.

2.3.1.2. Representation of Electronic Structure with Unitary Group Approach

The irreducible representations of the unitary group $U(n)$ are identified by "Young shapes" and the components of the irreducible representations are identified by "Weyl tableaux" [41]. Young shape is a graph with $N \leqq 2n$ boxes with the number of boxes in each row non-increasing downwards, such as

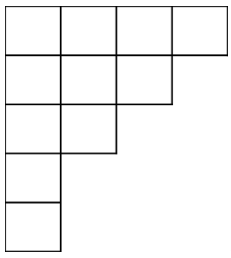

(37)

,

In the case of electronic structure calculations, Young shapes restrict those with at most two columns, such as

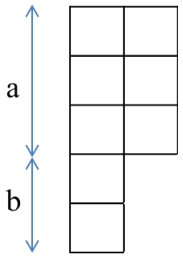

(38)

where a and b are the number of two-box and one-box rows, respectively. The dimension of the unitary group n represents the total number of molecular orbital (MO) basis, the number of boxes N ($= 2a+b$) represents the number of electrons, and the number of one-box rows b in the Young shape represents the double total spin quantum number $2S$.

The individual components of each irreducible representation are specified by populating the boxes with distinct "tokens", which is called Weyl tableaux, as

1	1
2	5
4	7
6	
7	

(39)

Each token represents the molecular orbital (MO) in their sequential order. Thus an MO is always represented by the same token. Here, the author describes an example how to represent the electronic structure with the Weyl tableaux by using eq. (39). Eq. (39) expresses one of the triplet eight-electron electronic configuration state functions (CSFs), because it has eight boxes and two one-box rows, which express $2S$. Here, MOs can be classified into 4 types and these types are named by step number d as follows: (i)

d = 0; MOs whose tokens do not appear in the Weyl tableau, which are defined as empty MOs, (ii) d = 1; those whose tokens appear once on the first (left-side) column, which are defined as singly occupied ones so as to raise S by 1/2, (iii) d = 2; those whose token appear once on the second (right-side) column, which are defined as singly occupied ones so as to lower S by 1/2, and (iv) d = 3; MOs whose tokens appear twice, which are defined as doubly occupied ones. By applying this definition, Eq. (39) can be rewritten as Table 2-2.

Table 2-2: Sequential orbital coupling

MO (i)	a_i	b_i	N_i	S_i	d_i
7	3	2	8	1	3
6	2	2	6	1	1
5	2	1	5	1/2	2
4	1	2	4	1	1
3	1	1	3	1/2	0
2	1	1	3	1/2	1
1	1	0	2	0	3
0	0	0	0	0	

As shown in Table 2-2, we begin with null entry at the bottom of the table, and proceed upwards. Adding the first MO, d_1 = 3 identifies a doubly occupied MO. Adding the second MO, d_2 = 1 identifies a singly occupied MO coupled to raise S_i by 1/2. Adding the third MO, d_3 = 0 identifies an empty MO and S_i does not change. The remaining rows (MOs) can be determined as the same manner. As shown above, the two-column Paldus *ab* tableau [38] fully specifies the Weyl tableau and is a compact and convenient

way to represent the spin-coupled function (CSF). Additionally the step vector **d** can also specify the Weyl tableau and is the most compact representation of the CSF. The incremental orbital coupling process is resemble to the Yamanouchi-Kotani spin-coupling scheme and corresponds to using the sequence of Unitary groups $U(1)$, $U(2)$, ..., $U(n)$, in the group subduction chain

$$U(n) \supset U(n-1) \supset \cdots \supset U(2) \supset U(1) \quad , \tag{40}$$

adapting the partial CSF to the corresponding irreducible representation at each stage.

The top (a, b) row of the Paldus tableau can identify the shape of Young shape, as well as the corresponding electronic state,

$$N = 2a + b,\ S = b/2 \quad . \tag{41}$$

Each Paldus tableau with the top row (a, b) specifies one of the CSFs of the full-CI expansion according to the incremental coupling scheme described previously. These tableaux can specify an orthonormal set of CSFs. Thus, we can specify the full-CI expansion set or any subset of it by the corresponding set of Paldus tableaus or the step vectors. As seen so far, the relation between these parameters are shown in Table 2-3. Here, Δ means the amount of change of each parameter or physical quantity.

Table 2-3: Relation between step numbers and quantum numbers

d_i	Δa_i	Δb_i	Δc_i	ΔN_i	ΔS_i
0	0	0	1	0	0
1	0	1	0	1	1/2
2	1	-1	1	1	-1/2
3	1	0	0	2	0

2.3.1.3. Graphical Representation

In the previous section, it was described that CSFs, which are the basis of CI expansion, can be specified by the compact representations, such as Paldus tableaus or step vectors. Next, the author draws a graphical representation of CSFs by using the step number vectors. An example is shown in Figure 2-1. It represents the graph for the full-CI expansion for $n = 6$, $N = 5$, $b = 2S = 1$.

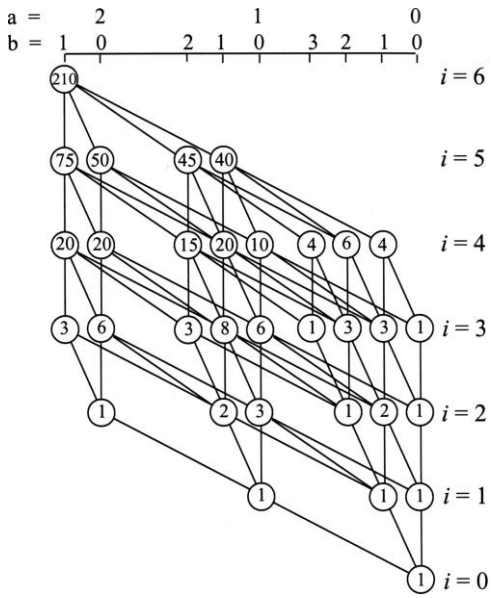

Figure 2-2 : Graphical representation of CSFs in GUGA

The DRT table, which contains Paldus tableau and step number vector, can be visualized in terms of a directed graph, in which each distinct row is represented by a "node", which means circle in Figure 2-2, and each link between two nodes is

represented by an arc pointing from the bottom of the link to its top. In this graph, different step numbers d_i are represented by arc of different slope.

In this graph, only two CSFs that have a closed-loop with specific shape can have non-zero contributions to the density matrix $\left\langle \Psi \middle| E_{ij} \middle| \Psi \right\rangle$. Therefore, once the graph is created, all the non-zero matrix elements of the density matrix can be listed and calculated without examined all the pairs of two CSFs, which is a special feature of GUGA used to significantly reduce computational efforts.

2.3.2. Application to the Calculation of Transition Density Matrix

As shown in eq. (31), the transition dipole moments can be represented as the trace of the products of dipole moment matrix elements and transition density matrix elements. To use the GUGA algorithm for calculation of transition density matrix, the author changed the original GUGA algorithm to be able to calculate the matrix elements between two MOs with different irreducible representations. Concretely speaking, in the numbering of CSFs, which is in the so-called lexical ordering scheme, all the CSFs including different irreducible representations are considered, while only the CSFs with the same irreducible representation were considered in the original GUGA scheme. After that, the loops, which express the coupling matrix elements between two MOs with all the CSFs, are generated. In this way, all the matrix elements between two MOs

in different irreducible representations can be evaluated automatically. The remaining calculations can be done as in the original GUGA scheme. In this study, the author coded and attached a program to compute transition density matrix with this scheme to the COLUMBUS program package and all the TDMs and oscillator strengths are calculated with this scheme.

Chapter 3

Calculation of f-f Oscillator Strength of PrX_3 and TmX_3

In this chapter, the oscillator strengths of both hypersensitive and non-hypersensitive transitions of PrX_3 and TmX_3 (X = Br, I), whose computational efforts are smallest among LnX_3, are evaluated with *ab initio* method using the program mentioned in the previous section 2.3. Furthermore, the origin of f-f transition intensities is examined focusing on the effects of molecular vibration, f-d mixing, and other configuration mixings.

3.1. Oscillator Strengths and Excitation Energies of Lanthanide Trihalides

3.1.1. Calculation Methods

Ab initio calculations were performed for LnX_3 (Ln = Pr, Tm; X = Br, I) by the SOCI method using the COLUMBUS program package [42]. The geometries of LnX_3 were D_{3h} with the experimental bond lengths [43], 5.08, 5.48, 4.88, 5.27 (Bohr) for $PrBr_3$, PrI_3, $TmBr_3$ and TmI_3, respectively. The model core potential (MCP) method, which

replaces the effects of the core electrons with MCPs, was used, and their integrals were evaluated with the GAMESS program [44]. The valence shells of the MCP methods are 4f5s5p5d6s for Ln [45], 3d4s4p for Br and 4d5s5p for I [46]. The author used (10s,7p,7d,6f)/[5s,3p,4d,4f] basis set [45],[47] for Ln, and (8s,7p,8d)/[3s,3p,3d] basis sets [46], [47] for halogens. The approximate one-body SO Hamiltonians [48] written as

$$H^{\mathrm{SO}} \approx \frac{\alpha^2}{2} \sum_{j}^{N} \sum_{A}^{Atom} \frac{Z_{\mathrm{eff}}(A)}{r_{jA}^3} \mathbf{l}_{jA} \cdot \mathbf{s}_j \quad , \tag{42}$$

were used and the values of Z_{eff} for Ln were determined to reproduce the experimental SO splittings of low-lying $4f^2$ excited states of the trivalent ions [49] and those of halogens were determined to reproduce the experimental SO splittings between $^2P_{3/2}$ and $^2P_{1/2}$ of the neutral atoms [50]. Molecular orbitals (MOs) were determined by the state-averaged SCF method optimized for the averaged state of all the configurations derived from $4f^N$.

For the SOCI calculations, configuration state functions (CSFs) with all the possible spin multiplicities derived from the $4f^N$ reference CSFs were generated in the first-order CI scheme, in which all the one-electron excitations from/to the reference CSFs were generated. The doubly occupied orbital spaces consisting of $5s^25p^6$ for $Ln^{3+}$and $(ns^2np^6)_3$ for $(X^-)_3$ (n = 4 for Br and n = 5 for I), and the external space consisting of all the SCF virtual orbitals were fully considered, so that all the relevant one-electron

excitations for Ln f-d mixing, LMCT, and intra-ligand excitations could be simultaneously accounted for. To calculate the oscillator strengths, the GUGA program mentioned in section 2.3.2 were used to calculate the transition density matrixes. The dipole length form was used as in eq. (32).

3.1.2. Praseodymium and Thulium Trihalides

Table 3-1 shows the oscillator strengths of PrX_3 and Table 3-2 shows those of TmX_3. The hypersensitive transitions reported in experimental studies [11] are as follows; from $^3H_4$ to $^3F_2$ for Pr^{3+}, from $^3H_6$ to $^3F_4$ and to $^3H_4$ for Tm^{3+}. As shown in Tables 3-1 and 3-2, the oscillator strengths of both hypersensitive transitions and non-hypersensitive transitions are evaluated quantitatively, even though the values are as small as 10^{-6} to 10^{-5}.

Table 3-1: Oscillator strengths ($f \times 10^6$) of PrX_3 from $^3H_4$.

States	$PrBr_3$		PrI_3	
	Calc.	Expt.[a]	Calc.	Expt.[a]
$^3H_5$	1.16	-	2.21	-
$^3H_6$	0.12	20.0 [b]	0.13	40.0 [b]
$^3F_2$	28.08		52.91	
$^3F_3$	3.62	1.0 [c]	7.08	13.4 [c]
$^3F_4$	1.18		1.71	

[a] Experimental oscillator strengths from Ref. [11].

[b] The sum of oscillator strengths to $^3H_6$ and $^3F_2$. [c] The sum of oscillator strengths to $^3F_3$ and $^3F_4$.

Table 3-2: Oscillator strengths ($f \times 10^6$) of TmX_3 from $^3H_6$.

States	$TmBr_3$		TmI_3	
	Calc.	Expt.[a]	Calc.	Expt.[a]
$^3F_4$	7.59	12.0	10.23	10.7
$^3H_5$	2.97	2.7	4.95	4.6
$^3H_4$	12.19	15.3	22.26	25.3
$^3F_3$	0.56	3.3 [b]	0.68	11.0
$^3F_2$	0.05		0.09	
$^1G_4$	4.48	4.5	7.39	-

[a] Experimental oscillator strengths from Ref. [11].

[b] The sum of oscillator strengths to $^3F_3$ and $^3F_2$.

Note that the molecular symmetry of D_{3h} is not a point group to which the selection rule by Judd [26] is applicable as was mentioned in section 2.1.2. The irreducible representations of the initial and final states, which carry the largest transition moments, were both E' and the components of these transition dipole moments were in the direction of the molecular plane ($x, y \in E'$). This result corresponds to the interpretation of the DC model that suggested the components of induced dipole of the halide ligands are the direction of the molecular plane [12].

3.2. Effect of Molecular Vibration on Oscillator Strength

3.2.1. Theory and Calculation Methods

If vibrational degrees of freedom are taken into consideration, photoabsorption intensity at a photon frequency ω consists of many vibronic transitions, each of which is

proportional to the squares of transition dipole moments between initial and final vibronic states, described as follows,

$$\sum_{\nu',\nu''}\left\langle \chi_{\nu'}^{F} \mid \mathbf{M}_{FI} \mid \chi_{\nu''}^{I} \right\rangle \cdot \left\langle \chi_{\nu''}^{I} \mid \mathbf{M}_{IF} \mid \chi_{\nu'}^{F} \right\rangle W_{\nu''}\, \delta(E_{\nu'}^{F} - E_{\nu''}^{I} - \omega) \quad , \tag{43}$$

where $\chi_{\nu''}^{I}$ and $\chi_{\nu'}^{F}$ are vibrational wavefunctions on the electronic states *I* and *F*, respectively. $E_{\nu''}^{I}, E_{\nu'}^{F}$ are their vibronic energies with symbolic vibrational quantum numbers ν" and ν', and $\mathbf{M}_{FI}$ is geometry dependent electronic transition dipole moment. $W_{\nu''}$ is the Boltzmann distribution factor of the initial electronic state.

As is well-known, 4f-electrons have a negligibly small contribution to chemical bonds, and relevant potential energy surfaces for the electronic states *I* and *F* in f-f transitions are very similar in shape, and their vertical energy difference is almost independent of molecular geometry. This characteristic allows the author to use the common normal coordinates **Q** for the electronic states *I* and *F* and to assume no photoabsorption intensity unless ν"≈ν'. With these considerations, eq. (43) can be simplified to the following expressions,

$$\begin{aligned}
&\delta(E_F - E_I - \omega)\sum_{\nu',\nu''}\left\langle \chi_{\nu'}^{F} \mid \mathbf{M}_{FI} \mid \chi_{\nu''}^{I} \right\rangle \cdot \left\langle \chi_{\nu''}^{I} \mid \mathbf{M}_{IF} \mid \chi_{\nu'}^{F} \right\rangle W_{\nu''} \\
&= \delta(E_F - E_I - \omega)\sum_{\nu',\nu''}\int \chi_{\nu'}^{F}(\mathbf{Q})^{*}\mathbf{M}_{FI}(\mathbf{Q})\chi_{\nu''}^{I}(\mathbf{Q})d\mathbf{Q}\cdot\int \chi_{\nu''}^{I}(\mathbf{Q}')^{*}\mathbf{M}_{IF}(\mathbf{Q}')\chi_{\nu'}^{F}(\mathbf{Q}')d\mathbf{Q}'\cdot W_{\nu''} \\
&= \delta(E_F - E_I - \omega)\sum_{\nu''}\int\int d\mathbf{Q}d\mathbf{Q}'\delta(\mathbf{Q}-\mathbf{Q}')\mathbf{M}_{FI}(\mathbf{Q})\chi_{\nu''}^{I}(\mathbf{Q})\cdot\chi_{\nu''}^{I}(\mathbf{Q}')^{*}\mathbf{M}_{IF}(\mathbf{Q}')\cdot W_{\nu''} \\
&= \delta(E_F - E_I - \omega)\int d\mathbf{Q}\,\mathbf{M}_{FI}(\mathbf{Q})\cdot\mathbf{M}_{IF}(\mathbf{Q})\sum_{\nu''}\chi_{\nu''}^{I}(\mathbf{Q})^{*}\chi_{\nu''}^{I}(\mathbf{Q})\cdot W_{\nu''}, \quad ,
\end{aligned} \tag{44}$$

where the contributions to all the vibrational states $\chi_{v'}^{F}(\mathbf{Q})$ on the final electronic state F are summed over and the completeness relation has been used. In order to estimate the impact of each normal vibration Q_i on the oscillator strength, The author evaluated the above integrals only along normal coordinate Q_i, with keeping $Q_j = 0\ (j \neq i)$, that is,

$$f_i^{FI} = \int dQ_i\, f_i'^{FI}(Q_i) \sum_{v''} \left| \chi_{v''}^{I}(Q_i) \right|^2 W_{v''} \quad , \tag{45}$$

where $f_i'^{FI}(Q_i)$ is the oscillator strength function calculated at normal coordinate Q_i. This integral f_i^{FI} can be interpreted as an averaged oscillator strength calculated with the weight of the existing probability function [51].

The author used this method to the oscillator strengths of $PrBr_3$. Full geometry optimization and vibrational analysis of $PrBr_3$ were carried out on the GAMESS [44] program system with the MCPs. The vibrational wavefunctions in eq. (45) were obtained by the finite difference grid method (FDM) [44]-[46] with a *Mathematica* program. The temperature value in the Boltzmann distribution factor was 1000 K corresponding to the experimental temperature in the vapor phase [11]. The oscillator strength function $f_i'^{FI}(Q_i)$ along each normal coordinate was calculated with SOCI method with the same calculation level mentioned in section 3.1. The total number of the grid points representing each potential function ranges from 10 up to 20. The vibrational states $\chi_{v''}^{I}$, whose populations were larger than 0.001, were included in eq.(45).

3.2.2. Application to Praseodymium tribromide

Full geometry optimization and vibrational analysis of $PrBr_3$ were carried out and the equilibrium structure and six normal coordinates Q_i were obtained as shown in Figure 3-1.

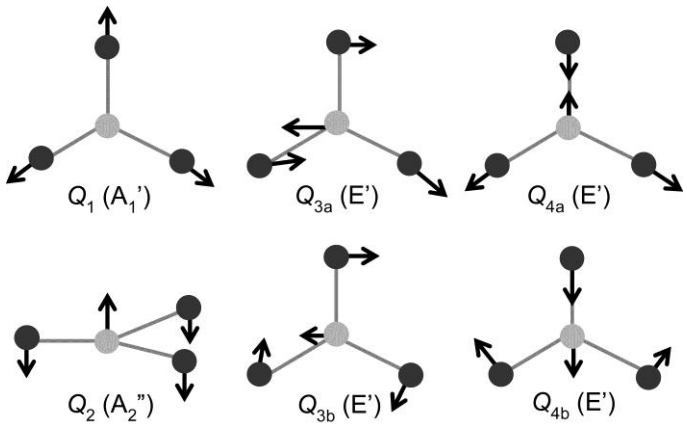

Figure 3-1. Normal vibrations of $PrBr_3$ molecule given by the vibrational analysis. Q_{na}(E') and Q_{nb}(E') (n = 3, 4) are doubly degenerate vibrations.

The optimized bond lengths of Pr-Br and the symmetry were 5.20 (Bohr) and D_{3h}, respectively, in good agreement with previously obtained results by Cundari et. al [16]. This bond length is also in reasonable agreement with a recent theoretical one, 5.15 (Bohr) with CASPT2 [21] and with experimental one [43], 5.08 (Bohr). The frequency of each normal vibration, as shown in Table 3-3, is also in reasonable agreement with experimental one [55].

Table 3-3: Oscillator strengths ($f \times 10^6$) of $PrBr_3$ in consideration of normal vibrations.

Modes	Q_1 (A_1')	Q_2 (A_2'')	Q_3(E')[a]	Q_4 (E')[a]
Frequencies[b]	196.4	35.4	245.7	45.8
Expt.[c]	193	31	236	45
$^3H_6$	0.11[d]	0.10	0.11	0.11
	(-0.18%)[e]	(-6.24%)	(1.11%)	(-0.64%)
$^3F_2$	27.29	26.41	27.29	26.33
	(0.05%)	(-3.15%)	(0.05%)	(-3.47%)
$^3F_3 + {}^3F_4$	4.52	4.49	4.53	4.49
	(-0.01%)	(-0.63%)	(0.11%)	(-0.62%)

[a] The average values of doubly degenerate components in each normal vibration.

[b] Frequencies (cm^{-1}) calculated by FDM.

[c] Experimental frequencies from Ref. [49].

[d] The upper stand shows oscillator strengths.

[e] The lower stand shows relative changes (%).

The molecular symmetry is lowered by the normal vibrations except for the totally symmetric stretching vibration $Q_1(A_1')$. The oscillator strengths including the vibrationally excited states of each normal vibration and their relative changes from those calculated at the equilibrium structure are shown in Table 3-3. The relative changes become larger as the frequency of normal vibration becomes smaller, yet they do not exceed about 6%. The out-of-plane bending vibration $Q_2(A_2'')$, the doubly degenerate stretching vibrations $Q_3(E')$, and the doubly degenerate bending vibrations $Q_4(E')$ can lower the molecular symmetry from D_{3h} to C_{3v}, C_s, C_{2v}, respectively, in which the hypersensitivities can be observed according to Judd [26] as mentioned in

section 2.1.2. Therefore it is confirmed again that the theory cannot give consistent explanation for LnX_3 systems. It turns out that the effect of molecular vibration on the f-f intensity is negligibly small and that molecular vibration cannot be a cause of hypersensitivity in contradiction to the previous interpretation by Gruen et al. [11] and Henrie et al. [28]

3.3. Shift of 5d Orbitals in Pr to Higher Energy Region

3.3.1. Model Core Potential Shift Operator

The atomic Hamiltonian for N_v valence electrons in the MCP method [45],[46]can be written as follows,

$$H_{\mathrm{mcp}} = \sum_{j=1}^{N_v}\left[-\frac{1}{2}\Delta_j + V_{\mathrm{mcp}}(r_j) + \sum_{c=1}^{n_{\mathrm{core}}} B_c \left|\psi_c\right\rangle\left\langle\psi_c\right|\right] + \sum_{i>j}^{N_v} r_{ij}^{-1} \quad , \tag{46}$$

where $\{\psi_c\}$, (c = 1s, 2s, …, n_{core}), denote core orbital functions. The projection operator $\sum B_c \left|\psi_c\right\rangle\left\langle\psi_c\right|$ is called energy shift operator because the energy levels of core orbitals are shifted. By including 5d orbital of Pr to this shift operator, the 5d orbital could be shifted to a higher energy region. Note that the purpose of this shift is different from that of the original MCP shift operators. The ψ_{5d} orbitals were expanded in terms of Gaussian-type functions [45] with an augmented d-polarization function (α_d = 0.45) to

reproduce the shape of the 5d orbitals calculated with all-electron HF method. The values of B_{5d} were set to 0.1, 0.5, 1.0, and 5.0 a.u.

3.3.2. Calculation of Oscillator Strength with Shift Operator

The author next tried to test the accepted theory by Judd and Ofelt [6],[7] that f-f intensity is induced by the mixing of the opposite parity configuration, such as $4f^{N-1}5d^1$, into the $4f^N$ states. If this interpretation is correct, the oscillator strength should become smaller as the mixing of the 5d component into 4f becomes smaller. The author focused attention on only 5d orbitals because the population of 5d orbitals was much larger than that of other virtual orbitals, such as 6s and 6p orbitals. To observe the decrease of the f-d mixing, The author shifted 5d orbitals to a higher energy region by adding MCP shift operators of the 5d orbitals to the Hamiltonian. By doing so, the mixing of the 5d components into the 4f orbitals, therefore the mixing of the configurations of $4f^{N-1}5d^1$ to the $4f^N$ states could be decreased. The oscillator strengths of $PrBr_3$ calculated in this way are shown in Table 3-4. With the 5d MCP shift operators, the oscillator strengths from $^3H_4$ to ^3P_J (J = 0, 1, 2) were decreased whereas those of the other transitions were increased contrary to the original expectation. From this result, it is clear that there exist other mechanisms than the f-d mixing for explaining f-f transitions including the hypersensitive transitions.

Table 3-4: The oscillator strength ($f \times 10^6$) of $PrBr_3$ with 5d shift operators with various B_{5d} values.

States	B_{5d} = 0	B_{5d} = 0.1	B_{5d} = 0.5	B_{5d} = 1.0	B_{5d} = 5.0
$^3H_5$	1.16	1.30 [c]	1.88	2.24	2.65
$^3H_6$	0.12	0.11	0.12	0.14	0.18
$^3F_2$	28.08	30.63	43.47	51.79	61.05
$^3F_3$	3.62	3.71	4.86	5.61	5.82
$^3F_4$	1.18	1.23	1.65	1.99	2.98
$^1G_4$	0.12	0.11	0.11	0.12	0.15
$^1D_2$	0.47	0.54	0.77	0.93	1.17
$^1I_6$	3.21	3.18	4.16	4.75	5.27
$^3P_0$	1.68	0.90	0.33	0.55	1.16
$^3P_1$	1.54	0.93	0.56	0.78	1.27
$^3P_2$	0.70	0.53	0.36	0.30	0.24

3.4. Decomposition of f-f Oscillator Strength

The author next examined the oscillator strengths in detail to find out electronic excitations which make dominant contributions to the oscillator strengths. The transition dipole moment is expressed with MO-basis transition density matrix as

$$\mathbf{M}_{FI} = \sum_{f,i} \left\langle \phi_f \left| \mathbf{r} \right| \phi_i \right\rangle \rho^{FI}(f,i) \equiv \sum_{f,i} \mathbf{m}'(f,i) . \tag{47}$$

Because MOs contain the components of both lanthanide and halogen, the author transforms MOs to atomic orbitals (AOs) to clarify which excitations, such as those from lanthanide to lanthanide or from ligands to lanthanide, contribute to the oscillator strengths. MOs are expressed in the linear combination of AOs as

$$\phi_i = \sum_s c_{si} \varphi_s^{\mathrm{AO}} , \quad \phi_f = \sum_r c_{rf} \varphi_r^{\mathrm{AO}} , \tag{48}$$

where φ^{AO} is AO and c is the expansion coefficient. Then eq. (47) can be written as

$$\begin{aligned}\mathbf{M}_{FI} &= \sum_{r,s}\left\langle \varphi_r^{\mathrm{AO}} \middle| \mathbf{r} \middle| \varphi_s^{\mathrm{AO}} \right\rangle \sum_{f,i} c_{rf} c_{si} \rho^{FI}(f,i) = \sum_{r,s}\left\langle \varphi_r^{\mathrm{AO}} \middle| \mathbf{r} \middle| \varphi_s^{\mathrm{AO}} \right\rangle P^{FI}(r,s) \\ &\equiv \sum_{r,s} \mathbf{m}''(r,s),\end{aligned} \tag{49}$$

where $P^{FI}(r,s)$ is the AO-basis transition density matrix. Here, the oscillator strength from initial states ${}^{2S+1}L_J$ to final states ${}^{2S'+1}L'_{J'}$ is written as the summation of the squares of the transition dipole moments all over the states correlated with the initial and final states. Eq. (49) can be rewritten by squaring both sides as

$$M_{FI}^2 = \mathbf{M}_{FI} \cdot \sum_{r,s} \mathbf{m}''(r,s), \tag{50}$$

and then the formula of the oscillator strengths is expressed as follows,

$$f({}^{2S'+1}L'_{J'} \leftarrow {}^{2S+1}L_J) = A\sum_{F,I} \omega_{FI} M_{FI}^2 = A\sum_{F,I}\sum_{r,s} \omega_{FI} \{\mathbf{m}''(r,s) \cdot \mathbf{M}_{FI}\} \equiv \sum_{r,s} \mu''(r,s), \tag{51}$$

where ω_{FI} is the excitation energy from a state I to a state F and A is $2/3(2J+1)^{-1}$. The values of $\mu''(r,s)$ and the relative intensities defined as

$$\frac{\mu''(r,s)}{f({}^{2S'+1}L'_{J'} \leftarrow {}^{2S+1}L_J)}, \tag{52}$$

were calculated for $PrBr_3$ and $TmBr_3$ and are shown in Figure 3-2. Here, the oscillator strengths were classified into four groups, such as $\mu''(\mathrm{Ln},\mathrm{Ln})$, $\mu''(\mathrm{X_3},\mathrm{Ln})$, $\mu''(\mathrm{Ln},\mathrm{X_3})$ and $\mu''(\mathrm{X_3},\mathrm{X_3})$, where Ln denotes all the AOs on lanthanide and X_3 denotes all the AOs on halogens.

As shown in Figure 3-2 (a-2), in the case of $PrBr_3$, the contributions of $\mu''(\mathrm{Ln},\mathrm{Ln})$ dominate the intensities of transitions from ${}^3H_4$ to ${}^3P_J$ (J = 0, 1, 2) whereas those of

$\mu''(X_3, X_3)$ dominate the intensities of other transitions including the hypersensitive transition from $^3H_4$ to $^3F_2$. In the case of $TmBr_3$, as shown in Figure 3-2 (b-2), those of $\mu''(X_3, X_3)$ dominate the intensities for almost all transitions including the hypersensitive ones from $^3H_6$ to $^3H_4$ and to $^3F_4$.

Recalling the observation in previous section 3.3.2 for the transitions from $^3H_4$ to ^3P_J (J = 0, 1, 2) of $PrBr_3$, the oscillator strengths became smaller as the f-d mixing became smaller. This observation is consistent with the dominant contributions of $\mu''(Ln, Ln)$, because these oscillator strengths are mainly described by the f-d mixing mechanism, that is, excitations between lanthanide atomic orbitals, especially from 4f to 5d, are important. However, there were other transitions whose oscillator strengths were increased with 5d shift operators. The formal charge in LnX_3 is described as $Ln^{3+}(X^-)_3$ and the Ln 5d orbitals are empty. In reality, however, there is non-negligible amount of charge transfer from ligand halogen atoms to the 5d orbitals (LMCT).

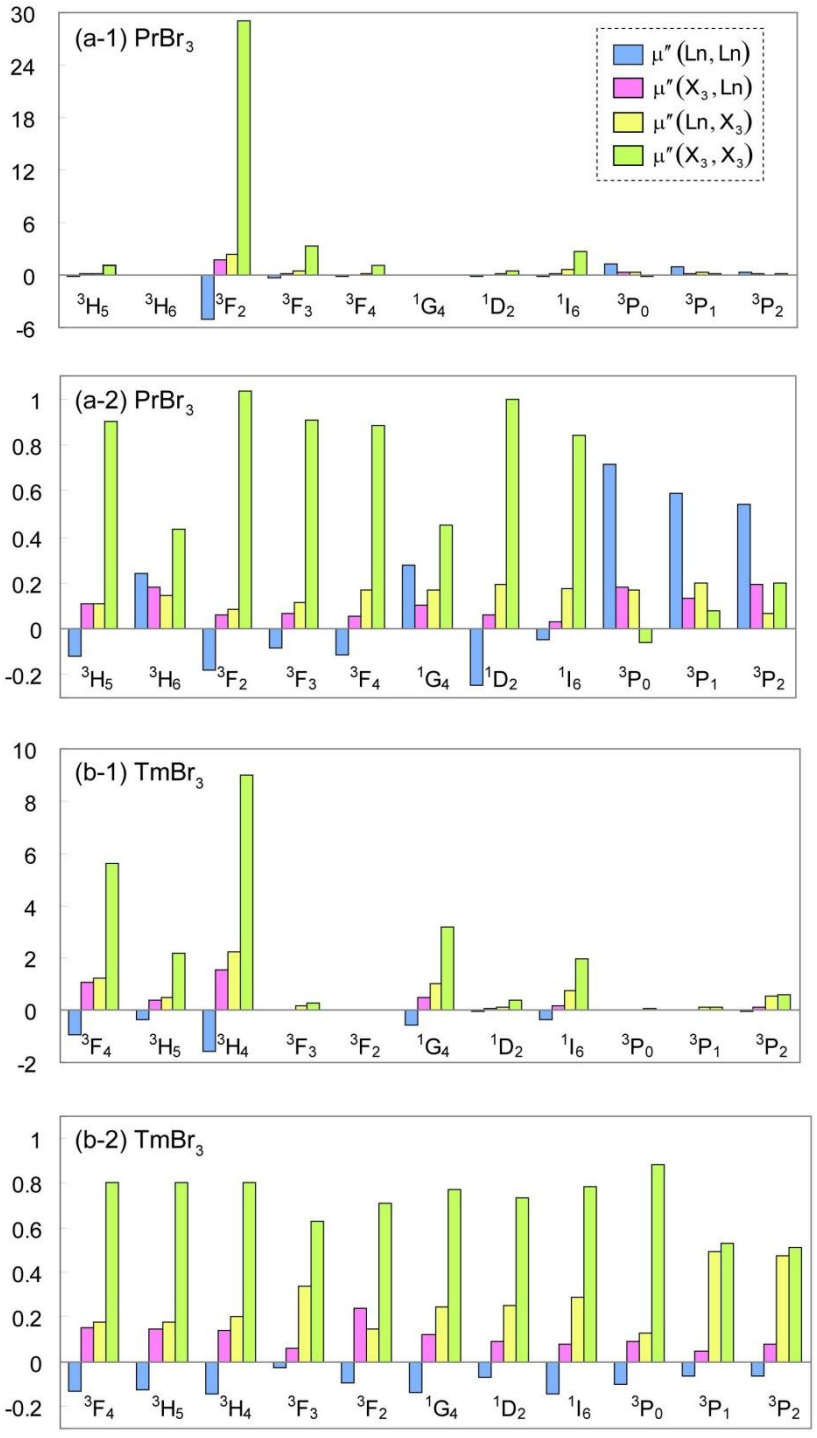

Figure 3-2: Calculation results of the values of $\mu''(r,s)$ in eq. (51) and the relative magnitudes in eq. (52). (a-1) and (a-2) are those for each transition from $^3H_4$ of $PrBr_3$. (b-1) and (b-2) are those for each transition from $^3H_6$ of $TmBr_3$. Blue, pink, yellow, and green bars are those for $\mu''(\mathrm{Ln},\mathrm{Ln})$, $\mu''(\mathrm{X_3},\mathrm{Ln})$, $\mu''(\mathrm{Ln},\mathrm{X_3})$, and $\mu''(\mathrm{X_3},\mathrm{X_3})$, respectively.

When 5d orbitals of lanthanide are shifted to a higher energy region, the LMCT would be less efficient, and the population in valence p orbitals of halogens is increased. If this is the case, the increase of the contributions of intra-ligand excitations is expected. As explained in what follows, these intra-ligand excitations dominate intensities of most of the f-f transitions, therefore the 5d shift operation would increase the oscillator strengths for these transitions. Moreover, for the transitions from $^3H_4$ to $^3H_6$ and to $^1G_4$ of $PrBr_3$ shown in Table 3-4, the oscillator strengths were decreased while the energy shift B_{5d} was small, however they were increased with larger B_{5d} values. This observation is consistent with the competing contributions of $\mu''(X_3, X_3)$ and other $\mu''(r,s)$, which are apparent in Figure 3-2 (a-2).

Next, the author examined which CSFs affect the values of $\mu''(X_3, X_3)$ most significantly. Because the present calculations include only single excitations from the reference CSFs, the pairs of CSFs which contribute to $\mu''(X_3, X_3)$ are restricted to the following five types,

$$((X_3(ns,np)\rightarrow Ln^*), (X_3(ns,np)'\rightarrow Ln^*)), \quad (53a)$$

$$((X_3(ns,np)\rightarrow X_3(ns,np)), (X_3(ns,np)'\rightarrow X_3^*)), \quad (53b)$$

$$((Ln(4f,5s,5p)\rightarrow X_3^*), (Ln(4f,5s,5p)\rightarrow X_3^{*\prime})), \quad (53c)$$

$$((X_3(ns,np)\rightarrow X_3^*), (X_3(ns,np)\rightarrow X_3^{*\prime})), \quad (53d)$$

$$(4f^N, (X_3(ns,np)\rightarrow X_3^*)) \text{ and } ((X_3(ns,np)\rightarrow X_3^*), 4f^N), \quad (53e)$$

where X_3(ns,np) and X_3* are occupied and virtual MOs of ligands, respectively, Ln(4f,5s,5p) and Ln* are occupied and virtual MOs of lanthanide, respectively, '$4f^N$'denotes the reference CSFs, and '(A→B*)' denotes the CSF that is obtained by one-electron excitation from an occupied MO 'A' to a virtual MO 'B*'.

In the present first-order CI scheme, an initial state and a final state can be expanded as follows,

$$\left|\Psi_I\right\rangle = \sum_l b_l \left|(\mathrm{Ln}^{\mathrm{N}})_l\right\rangle + \sum_n c_n \left|(\mathrm{X}_3 \rightarrow \mathrm{Ln}^*)_n\right\rangle + \sum_m d_m \left|(\mathrm{X}_3 \rightarrow \mathrm{X}_3^*)_m\right\rangle + \cdots, \tag{54}$$

$$\left|\Psi_F\right\rangle = \sum_{l'} b_{l'} \left|(\mathrm{Ln}^{\mathrm{N}})_{l'}\right\rangle + \sum_{n'} c_{n'} \left|(\mathrm{X}_3' \rightarrow \mathrm{Ln}^*)_{n'}\right\rangle + \sum_{m'} d_{m'} \left|(\mathrm{X}_3' \rightarrow \mathrm{X}_3^*)_{m'}\right\rangle + \cdots, \tag{55}$$

where b_l, c_n and d_m are CI coefficients for intra-metal excitations including $4f^N$ and f-d mixing CSFs, LMCT, and intra-ligand excitation CSFs, respectively, for the initial state, whereas $b_{l'}, c_{n'}$ and $d_{m'}$ are those for the final state. These LMCT and intra-ligand excitation CSFs represent respectively the contributions described by the covalency model [28] and the DC model [12]-[15] mentioned in the previous sections 2.1.2 and 2.1.3. For most lower lying $4f^N$ states, the magnitudes of the CI coefficients were found to be typically in the following order,

$$|b_l|, |b_{l'}| >> |c_n|, |c_{n'}| > |d_m|, |d_{m'}|, \tag{56}$$

that is, the magnitudes of CI coefficients for LMCT CSFs were typically larger than those of intra-ligand excitation CSFs. Additionally, the amounts of mixing of reference ($4f^N$) CSFs are more than 0.95. Therefore, a pair of CSFs in eq. (53e), which represent

reference and intra-ligand excitation CSFs, has a dominant contribution of order of $b_l d_{m'}$ and $b_{l'} d_m$ to the transition density matrix. In a similar manner, a pair of CSFs in eq. (53a), both of which represent LMCT, has a contribution of order of $c_n c_{n'}$ to the transition density matrix and has smaller contribution than that in eq. (53e). A pair of CSFs of eq. (53b) or eq. (53d), both representing intra-ligand excitations, has a much smaller contribution of order of $d_m d_{m'}$. A pair of CSFs in eq. (53c) represents metal to ligand charge transfer (MLCT) contributions, whose CI coefficients are in general much smaller than those for LMCT and their possible contributions to $\mu''(X_3, X_3)$ are also small.

From eq. (56), it may be expected that CSF pairs of $4f^N$ and LMCT have a large contribution to intensity in the forms of $\mu''(X_3, Ln)$ and $\mu''(Ln, X_3)$ in Figure 3-2. However, as shown in eq. (47), transition dipole moments are given by the trace of dipole matrix elements and transition density matrix elements. In the case of $PrBr_3$, the contributions of dipole matrix elements for these CSF pairs are very small because lower virtual Ln MOs and occupied X_3 MOs do not have a significant overlap. By comparing the results in Figure 3-2 and also those for PrI_3 and TmI_3 (not shown), in general, the contributions of $\mu''(X_3, Ln)$ and $\mu''(Ln, X_3)$ become increased for heavier Ln, and for heavier X. These tendencies are expected since the orbital overlap between

lower virtual Ln MOs and occupied X_3 MOs will be increased for heavier Ln due to the so-called lanthanide contraction, and for heavier X due to the increased size of X_3 MOs.

From the above consideration, it is understandable that the oscillator strengths of most f-f transitions including hypersensitive transitions arise from the intra-ligand excitations through their configuration mixings with the dominant configurations of $4f^N$. It is therefore interpreted that the reason of hypersensitive transitions in LnX_3 molecules is the significant contribution of this effect which does not work much in aqueous Ln^{3+} systems. It is also interpreted that the oscillator strengths of hypersensitive transitions are sensitive to the surrounding environment as a direct reflection of the sensitivity of these mixed states to small changes of ligands.

Recalling the observation in section 3.1.2, the components of large f-f transition dipole moments were in the direction of the molecular plane ($x, y \in E'$). Therefore the irreducible representation of the $X_3 \rightarrow X_3^*$ portion must be E' for the transition dipole moment between the pairs of CSFs (53e) to have a large value. This symmetry requirement limits both X_3 and X_3^* to have σ symmetry or π symmetry. Separate calculations on artificial molecule of $(X^-)_3$, whose structure was taken from LnX_3, showed that it had large transition dipole moments of e' symmetry for one-electron excitations from valence σ symmetry MOs (e') to lower unoccupied σ symmetry MOs (a_1', e') while those in the z direction were much smaller. These results are consistent

with the fact that the f-f transition dipole moments had large values only in the direction of molecular plane.

Next, the author compared the results with the DC model [12], which considers the effect of intra-ligand polarized type excitation. In the DC model, the oscillator strength is derived in the same way as the Judd-Ofelt theory by adding intra-ligand excitation configurations to the opposite parity configurations as follows,

$$\left|\Psi_{4f^N}\right\rangle = \left|(4f^N)_a\right\rangle + \sum_{b,l} \frac{\left\langle (4f^N)_b \otimes (X_3 \rightarrow X_3^*)_l \left| V \right| (4f^N)_a \right\rangle}{E_a - E_b - E_l} \left| (4f^N)_b \otimes (X_3 \rightarrow X_3^*)_l \right\rangle, \quad (57)$$

where V denotes the intersystem coulombic potential whose perturbation matrix element can be approximately expanded in the product of f-f transition quadrupole moment of lanthanide and transition dipole moment of ligand, and $(4f^N)_b \otimes (X_3 \rightarrow X_3^*)_l$ denotes the CSF that is obtained by one-electron excitation from an occupied MO of X_3 to a virtual MO of X_3^* with the $(4f^N)_b$ configuration. Comparing eq. (57) and eq. (54), it is obvious that the essential part of the DC model, that is, the coulombic correlation between the transition quadrupole moment of Ln and the transition dipole moment of the X_3 portion can be accounted for in the present first-order CI scheme. In the DC model, the expression of f-f transition dipole moments yields the squares of transition dipole moments of ligand, which can be further reduced to the components of the polarizability tensor of the ligand [12]. Therefore including the intra-ligand excitation

contributions in the present first-order CI scheme corresponds to considering the effect of the dynamical coupling between Ln and the X_3 portion, with ligand-polarization taken into account.

As Tables 3-1 and 3-2 show, the oscillator strengths of hypersensitive transitions are larger than those of others. Moreover, as Figure 3-2 shows, these hypersensitive transitions are dominated by $\mu''(X_3, X_3)$, and this dominance of $\mu''(X_3, X_3)$ can also be seen in most other transitions. This observation is consistent with the DC model. In this model, only the expression of τ_λ parameter is different from those of the original Judd-Ofelt theory. The τ_λ parameters of the DC model contain the polarizability of the ligand and the ligand-polarization contributions to these parameters are very large only for the τ_2 (i.e. $\Delta J \leq 2$). Therefore it is interpreted that the magnitude relation between transitions is caused by the magnitude relation of the matrix element of reduced tensor operator $\mathbf{U}^{(2)}$ [33], because τ_4 and τ_6 are very small. In other words, the mechanism of the DC model can be adapted to not only so-called hypersensitive transitions but also other transitions with $\Delta J \leq 2$. In this way, the semi-empirical DC model could explain the hypersensitivity of transitions with $\Delta J \leq 2$. However the author emphasizes the current *ab initio* calculations showed that the transitions with very large contributions of $\mu''(X_3, X_3)$ are not limited to the case of $\Delta J \leq 2$.

As Tables 3-1 and 3-2 show, the oscillator strengths of LnI_3 are larger than those of $LnBr_3$. In order to explain the difference between ligands, the author tested the effect of magnitude of the SO effect by changing the values of Z_{eff} and proved that the SO effect of X_3 on the oscillator strength was very small. Therefore considering the DC model containing the polarizability of the ligand in τ_λ and the results of these test calculations, it is interpreted that the magnitude order between ligands seen in Tables 3-1 and 3-2 is explained by that of the polarizability of the ligands. In summary, to contain all the effects in the evaluations of oscillator strengths, *ab initio* calculations should be carried out.

Chapter 4

Comparing ab initio calculation with the dynamic-coupling model for $LnBr_3$

In this chapter, the origin of f-f hypersensitive transition intensities is discussed by comparing the two Judd-Ofelt intensity parameters τ_2 evaluated with the dynamic-coupling model and those with the *ab initio* calculations for $LnBr_3$ (Ln = Pr, Nd, Pm, Sm, Eu, Tb, Dy, Ho, Er, Tm). The author focuses on the components of transition dipole moment divided by the atomic orbitals on Ln and Br_3.

4.1. Oscillator Strengths, Excitation Energies and Judd-Ofelt Intensity Parameters of $LnBr_3$

4.1.1. Calculation Methods

Ab initio calculations were performed for $LnBr_3$ (Ln = Pr through Tm except for Gd) by the multi-reference spin-orbit configuration interaction (MRSOCI) method [25] using the COLUMBUS program package [42]. The MCP method by Sakai et al. was

used as in the previous section 3. The author used the same basis sets for Ln [45],[47] and more diffuse MCP-DZP basis set with diffuse functions (9s,8p,8d)/[4s,4p,3d] for Br [46],[56] to calculate the excitation energies, oscillator strengths, τ_2(dc) and τ_2(ab). The bond lengths between Ln and Br in the D_{3h} structure, the effective nuclear charges Z_{eff}, MOs, and CI spaces were determined as in the previous section 3.The author carried out the "standard SOCI" [25] calculations where the total Hamiltonian including the SO term was diagonalized in the basis of all the CSFs for $PrBr_3$, $EuBr_3$, $TbBr_3$ and $TmBr_3$. For the remaining $LnBr_3$, however, the Davidson diagonalization algorithm with the standard SOCI method exhibited poor convergence, especially for higher lying excited states, where a large number of states are densely populated. For the rest of $LnBr_3$, the author therefore employed the "contracted SOCI" method where the total Hamiltonian including the SO term was diagonalized in the basis of spin-free CI eigenstates whose main configurations are $4f^N$ [57].

The JO intensity parameters τ_2(ab) were evaluated using the relation eq. (58) with the calculated excitation energies ω and the oscillator strengths f as follows,

$$\tau_2(ab) = f\,\frac{2J+1}{\omega}\left|\left\langle {}^{2S+1}L_J \left\| \mathbf{U}^{(\lambda)} \right\| {}^{2S'+1}L'_{J'} \right\rangle\right|^{-2} \qquad (58)$$

Here, the author considered only the dominant term of $\lambda = 2$ and neglected small terms of $\lambda = 4$, 6 in eq. (14). [12]. The matrix elements of $\mathbf{U}^{(2)}$ employed were those listed in Refs [33]-[36]. JO intensity parameters τ_2(dc) as derived from the DC model were

evaluated using eq. (29). The polarizability of Br^- was calculated with the corresponding first-order SOCI method and the values of $\langle 4f|r^2|4f\rangle^2$ were calculated with the same state-averaged SCF method as before with the same MCP basis set [45]-[47],[56] mentioned above.

4.1.2. Results and Discussion

Table 4-1 shows the excitation energies and oscillator strengths of hypersensitive transitions of $LnBr_3$. The excitation energies are slightly overestimated in comparison with the experimental ones [11], while the oscillator strengths are in reasonable agreement [11] though the values are as small as 10^{-6} to 10^{-4}. The JO intensity parameters τ_2(ab) and τ_2(dc) evaluated by the two methods are compared in Figure 4-1. The polarizability of Br^- used for τ_2(dc) was $\alpha(Br^-)$ = 37 a.u., in reasonable agreement with the empirical ones, 28 and 30 a.u. [58],[59]. It should be noted that the oscillator strengths of $PrBr_3$ and $TmBr_3$ in Table 4-1 are larger than those in chapter 3, which were underestimated by the previous smaller basis set for Br, with which a small polarizability $\alpha(Br^-)$ = 12 a.u. was produced.

Table 4-1 : Excitation energies ΔE (cm^{-1}), oscillator strengths ($f \times 10^6$), and JO intensity parameters τ_2(ab) of $LnBr_3$

Ln	Transitions [a]	ΔE		f		τ_2(ab)
		Calc.	Expl.[b]	Calc.	Expl.[b]	
Pr $4f^2$	$^3H_4 \rightarrow {}^3F_2$	5488	4800	36.1	20	11.7
Nd $4f^3$	$^4I_{9/2} \rightarrow {}^4G_{5/2}$	21748	17300	195.4	330	10.0
Pm $4f^4$	$^5I_4 \rightarrow {}^5G_2$	23074	--	125.3	--	6.8
Sm $4f^5$	$^6H_{5/2} \rightarrow {}^6F_{1/2}$	7329	6200	15.8	--	6.7
Eu $4f^6$	$^7F_0 \rightarrow {}^7F_2$	1132	--	9.2	--	5.9
	$^7F_0 \rightarrow {}^5D_2$	23991	21500	0.5	--	2.6
Tb $4f^8$	$^7F_6 \rightarrow {}^7F_5$	1885	--	6.0	--	7.7
Dy $4f^9$	$^6H_{15/2} \rightarrow {}^6F_{11/2}$	8739	7700	43.9	--	8.6
Ho $4f^{10}$	$^5I_8 \rightarrow {}^5G_6$	26380	22200	174.6	--	7.4
Er $4f^{11}$	$^4I_{15/2} \rightarrow {}^2H_{11/2}$	22591	19200	28.3	58	2.9
	$^4I_{15/2} \rightarrow {}^4G_{11/2}$	30842	26500	99.3	99	5.6
Tm$4f^{12}$	$^3H_6 \rightarrow {}^3H_4$	5814	5500	9.6	12	9.1
	$^3H_6 \rightarrow {}^3F_4$	12883	12600	15.6	15.3	2.9

[a] List of hypersensitive transitions is from Ref. [11]. those of Pm, Tb, and $^7F_0 \rightarrow {}^7F_2$ of Eu are added because the matrix elements of $\mathbf{U}^{(2)}$ have relatively large values [33]-[36].
[b] Experimental excitation energies are from Ref. [11].

As shown in Figure 4-1, the τ_2(dc) value decreases monotonically with the atomic number of Ln, because the value of $\left\langle 4f \left| r^2 \right| 4f \right\rangle^2$ in eq.(29) decreases monotonically reflecting the decrease in the size of 4f orbitals. (Note that the distance R_L between Ln and Br also decreases due to the lanthanide contraction. However, the rate of the decrease of $\left\langle 4f \left| r^2 \right| 4f \right\rangle^2$ is larger than that of the increase of R_L^{-8}.) In comparison with τ_2(dc), the τ_2(ab) values in general have smaller values and a different Ln dependence, especially between Eu and Tb, but they are still in the same order of

magnitude. Therefore, it may be conclude that the overall behavior of τ_2 of $LnBr_3$ can be roughly evaluated with the DC model. As mentioned above, the previous less diffuse basis set for Br in chapter 3 underestimated the oscillator strengths of $LnBr_3$ compared with the current one. This is understandable because the f-f oscillator strengths can be derived mainly by the DC model and their values depend directly on the polarizability of the ligand.

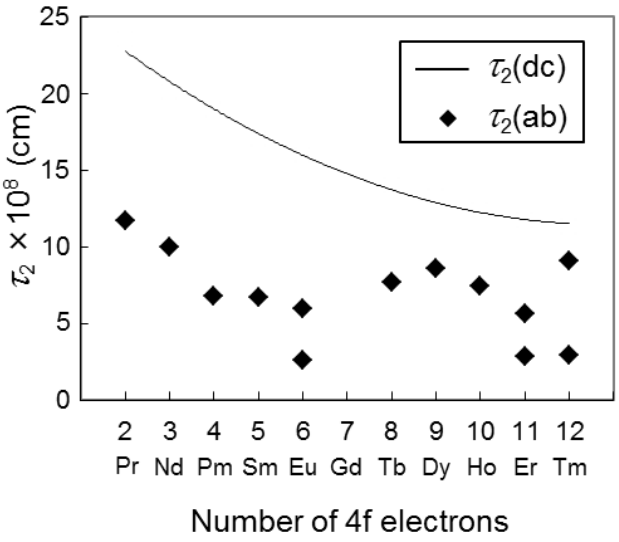

Figure 4-1: JO intensity parameters τ_2(dc) and τ_2(ab) as functions of the number of 4f electrons

Because $EuBr_3$, $ErBr_3$, and $TmBr_3$ have two hypersensitive transitions, the author has plotted each τ_2(ab) value simply as derived from eq. (58), though τ_2(ab) in the same molecule should have an identical value. The large splitting between two parameter values, especially in $^3H_4$ and $^3F_4$ of $TmBr_3$, can be explained by the significant

deviations of the final states from the LS coupling scheme [57], as assumed in the JO theory.

The author next focuses on the difference between τ_2(dc) and τ_2(ab). To investigate the reason for the different values, the author points out "the polarization shielding effect" [60],[61] which was not considered in the original DC model [12]-[15]. Because 5s and 5p electrons are the outermost shell of Ln^{3+}, they are distorted significantly by the crystal field of three Br^{-}. It was suggested later that this effect weakens the Coulombic correlation between the transient-induced dipoles of ligands and the transition quadrupole of Ln, and was sometimes called "the shielding effect" in the DC model [62],[63]. This effect was considered through the Coulombic interaction of the perturbing polarized configurations of Ln with the $4f^N$ configurations [60]. Therefore, this effect can be accounted for in the current CI calculations through one-electron excitation configurations from the 5s and 5p orbitals, denoted as 5s5pCSFs. To investigate the magnitude of this polarization shielding effect, the oscillator strengths of hypersensitive transition in $PrBr_3$ were calculated with the state-averaged SCF MOs, (a) including and (b) excluding 5s5pCSFs, and also with the natural orbitals derived from the averaged density matrices of the SOCI initial and final states, (c) including and (d) excluding 5s5pCSFs. Their results were: $f \times 10^6 = 36.1$ (a, see Table 4-1), 69 (b), 35 (c), and 30 (d). It is clear that the 5s and 5p polarizations have a significant effect on the

oscillator strengths, and the use of non-polarized 5s and 5p orbitals would result in a significant overestimation of the oscillator strengths. Additionally, a trend seen in Figure 4-1 that the size reductions of τ_2(ab) relative to τ_2(dc) for the early lanthanides exceed those for the late lanthanides is consistent with the decreasing tendency in this shielding parameter with the atomic number [64],[65]. Thus a part of the difference between τ_2(ab) and τ_2(dc) originates from the polarization shielding effect due to the 5s and 5p orbitals.

As seen so far, general behavior of τ_2(ab) of $LnBr_3$ can be roughly reproduced with the DC model. To verify the hypothesis that the intensities of hypersensitive transitions are considered essentially by the DC model, the author examines the type of dominant CSFs that contribute the values of τ_2(ab) in the following section.

4.2. Decomposition of Transition Dipole Moment in Hypersensitive Transition

4.2.1. Calculation Methods

In this section 4.2, to facilitate unambiguous decompositions of dipole matrix elements, some diffuse basis functions were removed from the above basis sets and only (8s,7p,7d,6f)/[3s,3p,4d,4f] basis sets for Ln and (8s,7p,7d)/[3s,3p,2d] for Br were kept. With these less diffuse basis sets, the excitation energies were increased by 10 – 100

cm^{-1}, whose magnitudes were smaller than typical crystal field splittings, and the oscillator strengths were reduced by 10 – 20%, which still keeps sufficient accuracy for the analysis of the mechanism of f-f intensities.

4.2.2. Results and Discussion

The author next focuses on TDMs, because τ_2(ab) is proportional to the "square" of TDM. Since TDMs are matrix elements of one-electron coordinate operators and the initial and final state wavefunctions in the f-f transitions typically have higher reference ($4f^N$) weights than 0.95, the TDM values can essentially be evaluated with the first-order wavefunctions; one can account for them by one-electron excitations from/to the reference CSFs. To find out the origin of hypersensitive transitions, the author looks for the dominant one-electron excitations that contribute to the TDMs.

A hypersensitive transition ($^{2S+1}L_J \rightarrow {}^{2S'+1}L'_{J'}$) actually contains ($2J$+1) eigenstates in the initial multiplet and ($2J'$+1) eigenstates in the final one, both of which are split by the crystal field. Individual pairs of the initial and final eigenstates carry different magnitudes of TDMs. Among these pairs, only a few pairs carry predominantly large TDMs, and their squared values contribute to τ_λ(ab) through the oscillator strengths in eq. (58). For each hypersensitive transition, the author chooses a pair of the initial and final eigenstates with the largest TDM and decompose them for theoretical analysis.

Note that these largest TDMs always belong to E*'* symmetry and the directions are in the molecular plane.

Firstly, a TDM is decomposed into nine classes based on the characters of individual MOs, such as doubly occupied MOs, active (4f) MOs, and virtual MOs as follows,

$$\begin{aligned}
\mathbf{M}_{IF} &= \sum_{i,j}^{N_{\mathrm{MO}}} \left\langle \phi_i \middle| \mathbf{r} \middle| \phi_j \right\rangle \left\langle \Psi_I \middle| \sum_{\sigma} a_{i\sigma}^{+} a_{j\sigma} \middle| \Psi_F \right\rangle = \sum_{i,j}^{N_{\mathrm{MO}}} \mathbf{m}'(i,j) \\
&= \sum_{i}^{N_{\mathrm{occ}}} \sum_{j}^{N_{\mathrm{occ}}} \mathbf{m}'(i,j) + \sum_{i}^{N_{\mathrm{occ}}} \sum_{j}^{N_{\mathrm{act}}} \mathbf{m}'(i,j) + \sum_{i}^{N_{\mathrm{occ}}} \sum_{j}^{N_{\mathrm{vir}}} \mathbf{m}'(i,j) \\
&+ \sum_{i}^{N_{\mathrm{act}}} \sum_{j}^{N_{\mathrm{occ}}} \mathbf{m}'(i,j) + \sum_{i}^{N_{\mathrm{act}}} \sum_{j}^{N_{\mathrm{act}}} \mathbf{m}'(i,j) + \sum_{i}^{N_{\mathrm{act}}} \sum_{j}^{N_{\mathrm{vir}}} \mathbf{m}'(i,j) \\
&+ \sum_{i}^{N_{\mathrm{vir}}} \sum_{j}^{N_{\mathrm{occ}}} \mathbf{m}'(i,j) + \sum_{i}^{N_{\mathrm{vir}}} \sum_{j}^{N_{\mathrm{act}}} \mathbf{m}'(i,j) + \sum_{i}^{N_{\mathrm{vir}}} \sum_{j}^{N_{\mathrm{vir}}} \mathbf{m}'(i,j) \\
&= \mu(\mathrm{occ},\mathrm{occ}) + \mu(\mathrm{occ},\mathrm{act}) + \mu(\mathrm{occ},\mathrm{vir}) + \cdots + \mu(\mathrm{vir},\mathrm{vir}) \,,
\end{aligned} \tag{59}$$

where Ψ_I and Ψ_F are the initial and final eigenstates; N_{occ}, N_{act}, N_{vir}, N_{MO} are the number of occupied, active, virtual orbitals, and the total MOs, respectively. The first and the second orbital space indices in $\mu(\mathrm{space}_I, \mathrm{space}_F)$ denote those for the initial and final state wavefunctions, respectively.

Table 4-2 : Decomposition of TDM integrals (in %) based on the MO classes and the AO centers for $PrBr_3$. [a,b]

	m(Ln,Ln)	*m*(Br,Br)	*m*(Br,Ln)	*m*(Ln,Br)	Total
μ(occ, vir)	-2.1	***41.5*** [c]	**-1.4** [d]	**0.2** [e]	38.2
μ(vir, occ)	-0.3	***42.8*** [c]	**0.0** [e]	**-2.0** [d]	40.6
μ(occ, act)	-0.9	6.0	**-1.3** [d]	1.9	5.7
μ(act, occ)	0.5	7.1	1.1	**-0.9** [d]	7.7
μ(vir, act)	**1.7** [f]	-0.5	**0.1** [e]	0.3	1.6
μ(act, vir)	**-0.3** [f]	0.1	0.0	**0.0** [e]	-0.2
μ(vir, vir)	-0.1	0.7	-0.3	-0.2	0.1
μ(act, act)	**-12.7** [f]	25.7	-6.5	-3.6	2.9
μ(occ, occ)	0.3	3.0	-0.1	0.1	3.3
Total	-13.9	126.4	-8.4	-4.1	100.0

[a] The first and second AO center indices in *m*(atom$_I$ and atom$_F$) denote those for the initial and final state wavefunctions, respectively.

[b] The first and second orbital space indices in μ(space$_I$, space$_F$) denote those for the initial and final state wavefunctions, respectively.

[c] Contributions from the matrix elements between the reference $4f^N$ configurations and intra-ligand excitation configurations (Type (ii)).

[d] Contributions from the matrix elements between the reference configurations and LMCT configurations.

[e] Contributions from the matrix elements between the reference configurations and MLCT configurations.

[f] Contributions considered in the JO theory.

An example of such a decomposition of the TDM for $PrBr_3$ are shown in Table 4-2, in which almost 80% of the TDM value comes from the two classes (excitations and de-excitations) between the occupied and virtual MOs, which are expressed as μ(occ,vir) and μ(vir,occ). In the current first-order CI scheme, these two terms originate

from the matrix elements between the reference CSFs and the CSFs representing one-electron excitations from the doubly occupied space to the virtual orbital space. If the individual occupied and virtual MOs were well localized in the Ln or ligand portions, it would be easy to characterize the physical meanings of the one-electron excitation CSFs which have a dominant contribution to TDMs. As schematically shown in Figure 4-2, the above two classes of components originate from the matrix elements between the reference CSFs and the four types of CSFs classified as Type(i) for intra-metal excitations (Ln(5s,5p) → Ln*), Type(ii) for intra-ligand excitations (Br_3(4s,4p)→Br_3*), Type(iii) for ligand to metal charge transfers (LMCT; (Br_3(4s,4p)→ Ln*)), and Type(iv) for metal to ligand charge transfers (MLCT; (Ln(5s,5p)→Br_3*)), where 'Ln*' and 'Br_3*' denote their virtual orbitals. The characteristics of the resultant TDM components are also given in Figure 4-2.

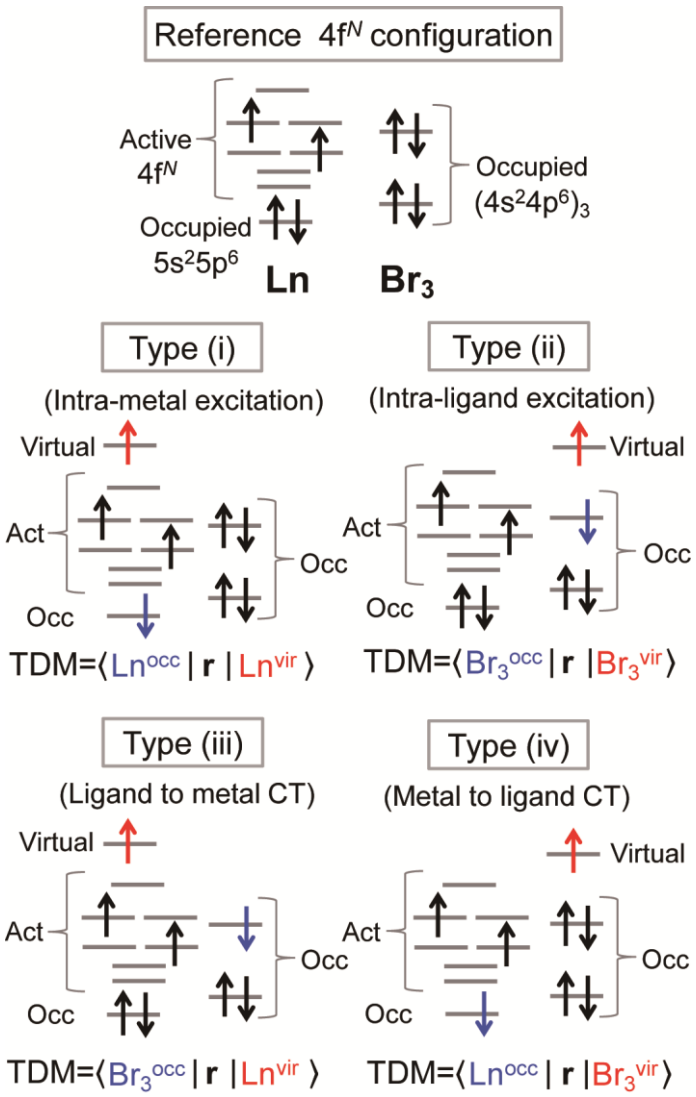

Figure 4-2. Electronic configurations of the reference $4f^N$ and one-electron excitation configurations Type (i) through Type (iv). Type (i) is a one-electron excitation from an occupied Ln orbital to a virtual Ln orbital. Type (ii) is an intra-ligand one-electron excitation. Type (iii) is a one-electron excitation from an occupied orbital in the Br_3 ligand to a virtual Ln orbital. Type (iv) is a one-electron excitation from an occupied Ln orbital to a virtual Br_3 orbital. The components of TDM matrix elements between the reference configuration and Type (i) through (iv) are also expressed as those between the two orbitals related to the one-electron excitations.

Secondly, since one-electron orbitals are not localized very well in the actual calculations, each of the nine classes of components is further decomposed into the four kinds based on the following basis transformations from MOs to atomic orbitals (AOs).

$$\mu(\text{occ, vir}) = \sum_{r,s} \left\langle \varphi_r^{\text{AO}} \middle| \mathbf{r} \middle| \varphi_s^{\text{AO}} \right\rangle \sum_{i}^{N_{\text{occ}}} \sum_{j}^{N_{\text{vir}}} c_{ri} c_{sj} \left\langle \Psi_I \middle| \sum_{\sigma} a_{i\sigma}^{+} a_{j\sigma} \middle| \Psi_F \right\rangle \equiv \sum_{r,s} m(r,s) \ , \qquad \text{where, } \ \phi_i = \sum_r c_{ri} \varphi_r^{\text{AO}} \ , \phi_j = \sum_s c_{sj} \varphi_s^{\text{AO}} \ . \tag{60}$$

The division is made by assigning the contributions of $m(r,s)$ to m(Ln,Ln), m(Br,Br), m(Br,Ln), and m(Ln, Br) based on the AO centers r and s, which are contained in the initial and final states, respectively. Specifically, m(Ln,Ln) in μ(occ,vir) and μ(vir,occ) contain Type(i) contributions, m(Br,Br) in μ(occ,vir) and μ(vir,occ) contain Type(ii) contributions, m(Br,Ln) in μ(occ,vir) and m(Ln,Br) in μ(vir,occ) contain Type(iii) contributions, and m(Ln,Br) in μ(occ,vir) and m(Br,Ln) in μ(vir,occ) contain Type(iv) contributions, respectively.

As shown in Table 4-2, Type(ii) has a largest contribution which is about 80 % to the total TDM matrix element. Type(iii) has a little contribution and Type(iv) has a negligible contribution. From this analysis, it is clarified that the TDMs of $PrBr_3$ are dominated by the DC model, and that the LMCT effect makes no significant contribution to the TMDs despite the larger magnitude of LMCT CSFs in the initial and final CI wavefunctions than that of intra-ligand excitation CSFs. Additionally, TDMs

in μ(act,act) express those caused by mixing of other components to 4f orbitals due to the presence of odd parity crystal field. For example, m(Ln,Ln) in μ(act,act) expresses TDMs between f and d components of Ln, which can be regarded as the JO theory effect. m(Ln,Ln) in μ(act,vir) and μ(vir,act) also express TDMs between reference CSFs and intra-metal (Ln(4f)→Ln*) excitation CSFs, which have little contributions.

Analyses of other $LnBr_3$ cases have shown that the general trends in the weight of each component to the TDM matrix elements are similar to those of $PrBr_3$; see Appendix.

To give an additional reason for the different behavior of τ_2(ab) and τ_2(dc), especially for $EuBr_3$, the m(Br,Br) contributions to TDMs for each of $LnBr_3$ are compared in Table 4-3. The DC model components of μ(occ,vir) and μ(vir,occ) have largest contributions in all $LnBr_3$. Another point to note, only for $EuBr_3$ and particularly for the $^7F_0 \rightarrow {}^5D_2$ transitions, is that the relative weights of μ(occ,vir) and μ(vir,occ) are reduced and those of μ(occ,act) and μ(occ,occ) are increased significantly. In this regard, it is important to point out that the weight of LMCT from the doubly occupied MOs on Br to the empty 4f orbitals (Br_3(4s,4p)→Ln*(4f)) in $EuBr_3$ is the largest among $LnBr_3$, reflecting the fact that the $4f^6$ configuration of Eu^{3+} turns to the relatively stable $4f^7$ half-filled configuration by accepting one electron from the ligand [66].

Table 4-3: Decomposition of the *m*(Br,Br) integral part of TDMs (in %) based on the MO classes for $LnBr_3$

	Pr	Nd	Pm	Sm	Eu [a]	Eu [b]	Tb	Dy	Ho	Er [c]	Tm [d]
μ(occ,vir)	***41.5***	***45.8***	***44.4***	***41.8***	***35.7***	***29.0***	***44.7***	***40.2***	***45.4***	***44.0***	***42.1***
μ(vir,occ)	***42.8***	***42.2***	***41.1***	***41.4***	***33.8***	***21.2***	***45.4***	***39.2***	***35.7***	***37.2***	***41.3***
μ(occ,act)	6.0	7.3	6.2	4.9	**11.2** [f]	**27.0** [f]	0.6	4.2	5.0	3.5	2.4
μ(act,occ)	7.1	3.5	2.3	5.4	8.1	7.8	0.3	4.8	2.3	1.1	3.0
μ(vir,act)	-0.5	-0.3	0.0	0.0	0.2	1.0	3.0	2.4	1.6	1.9	2.0
μ(act,vir)	0.1	0.4	0.4	0.4	0.1	1.9	2.8	3.1	2.4	2.4	2.5
μ(vir,vir)	0.7	0.5	0.1	0.0	0.2	-0.4	-0.5	-0.1	-0.2	-0.3	-0.3
μ(act,act)	25.7	18.0	16.4	21.9	18.1	11.2	14.4	14.6	8.1	8.1	12.1
μ(occ,occ)	3.0	2.6	0.9	1.3	**7.6** [g]	**15.3** [g]	0.9	3.7	3.8	1.9	2.0
Total	126.	119.	111.9	117.	114.	114.	111.5	112.	104.	99.7	107.

[a] Decomposition of the TDM ($^7F_0 \rightarrow {}^7F_2$) for $EuBr_3$.

[b] Decomposition of the TDM ($^7F_0 \rightarrow {}^5D_2$) for $EuBr_3$.

[c] Decomposition of the TDM ($^4I_{15/2} \rightarrow {}^4G_{11/2}$) for $ErBr_3$. See the Appendix for the TDM ($^4I_{15/2} \rightarrow {}^2H_{11/2}$) .

[d] Decomposition of the TDM ($^3H_6 \rightarrow {}^3H_4$) for $TmBr_3$. See the Appendix for the TDM ($^3H_6 \rightarrow {}^3F_4$) .

[e] Contributions from TDM integrals between the reference configurations and intra-ligand excitation configurations (Type (ii)).

[f] Contributions from TDM between doubly occupied MOs on Br and 4f active orbitals that delocalized a little to the Br portion, which represent a part of contributions considered in the DC model.

[g] Contributions from TDM integrals between two excitation configurations from different occupied orbitals of Br to an identical active or virtual orbital, mostly between two LMCT configurations (Type (v)).

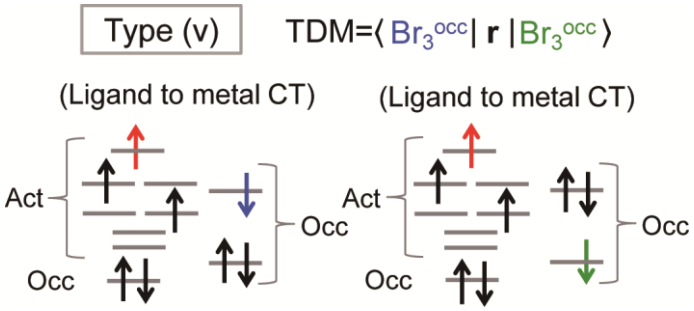

Figure 4-3: A pair of CSFs representing LMCTs from different occupied MOs on Br to an identical active or virtual orbital contribute to the μ(occ,occ) component in m(Br,Br).

The importance of this type of LMCT in $EuBr_3$ increases the magnitude of these CI coefficients, although their actual values are still much smaller than the dominant $4f^6$ reference CSFs. This increase in the LMCT in turn decreases the relative importance of the Type (ii) intra-ligand excitation CSFs and these changes in the magnitude of the first-order wavefunctions cause the following first- and second-order effects on the components of TDM in Table 4-3.

A decrease in the relative weights of μ(occ,vir) and μ(vir,occ) for $EuBr_3$, which is crucial to the decrease of τ_2(ab), is a first-order effect caused by the reduction of the importance of the Type (ii) CSFs. Similarly, an increase in μ(occ,act) for $EuBr_3$ is caused by an increased importance of the Br_3(4s,4p)→Ln*(4f) LMCT.

An increase in the relative weight of μ(occ,occ) in m(Br,Br) of $EuBr_3$ in Table 4-3 is an example of the second-order effect caused by the increase in the LMCT to Ln*(4f). Note that this increased component of μ(occ,occ) in m(Br,Br) originates from the matrix

elements between the two excitation CSFs from different occupied MOs on Br to an identical active or virtual orbital, as indicated in Type (v) in Fig. 4-3.

As discussed so far, the size reduction of τ_2(ab) from τ_2(dc) is the largest in $EuBr_3$ because, in this molecule, a part of the weight of the 'bright' intra-ligand excitation CSFs in the first-order wavefunctions is shifted to that of the 'dark' Br_3(4s,4p)→Ln*(4f) type LMCT CSFs. To study more closely, however, other effects such as LMCT to virtual Ln MOs other than 4f and the mixing of LMCT and intra-Ln excitation CSFs should be considered simultaneously.

Chapter 5

Comprehensive Analyses of Origin of f-f Oscillator Strength and Hypersensitivity

In this chapter, f-f transition intensities of hypersensitive transitions of $LnCl_3$ and LnI_3 are also calculated and are compared with those of $LnBr_3$ in chapter 4 to give a comprehensive mechanistic explanation for the origin of their intensities. To have a different perspective on the origin of f-f hypersensitive transition intensities, the spatial distributions of the transition dipole moment and transition density are examined. Furthermore, the relation between the Judd-Ofelt intensity parameters τ_2 and the average amount of LMCT is considered. The phase relation between the contributions to the transition moments from the f-d mixing and from the intra-ligand excitation configurations is also discussed.

5.1. Oscillator Strengths and Judd-Ofelt Intensity Parameters of LnX_3

5.1.1. Calculation Methods

Ab initio calculations were performed for LnX_3 (Ln = Pr, Nd, Pm, Sm, Eu, Tb, Dy, Ho,

Er, and Tm; X = Cl and I) by the MRSOCI method using the COLUMBUS program package. The MCPs by Sakai et al. were used. The valence shells of MCP-DZP are 3s3p for Cl and 4d5s5p for I. The basis sets, geometries, bond lengths, the effective nuclear charges Z_{eff}, MOs and CI spaces were determined in the same manner as in section 4.1.

5.1.2. Results and Discussion

The calculated oscillator strengths of hypersensitive transitions of LnX_3 (X = Cl and I) are shown in Table 5-1 along with those of $LnBr_3$ obtained in section 4.1. They are in reasonable agreement with the experimental ones [11] though the values are as small as from 10^{-6} to 10^{-4}. The Judd-Ofelt (JO) parameters τ_2 were evaluated with two methods; τ_2(ab) were calculated inversely in terms of eq. (58) using the excitation energies and oscillator strengths calculated with *ab initio* methods, and τ_2(dc) were calculated in terms of eq. (29); these parameters are shown in Figure 5-1. The polarizabilities of the halogen anions calculated with the MCP method and used in the calculation of τ_2(dc) were $\alpha(I^-)$ = 59 and $\alpha(Cl^-)$ = 27 a.u. These are in reasonable agreement with the experimental ones, $\alpha(I^-)$ = 47 and $\alpha(Cl^-)$ = 20 a.u. [58].

Table 5-1 : Excitation energies ΔE (cm^{-1}) and oscillator strengths $f \times 10^6$ of LnX_3

Ln	Transitions	f ($LnCl_3$)		f ($LnBr_3$)		f (LnI_3)	
		Calc.	Expl.[a]	Calc.[b]	Expl.[a]	Calc.[b]	Expl.[a]
Pr $4f^2$	$^3H_4 \rightarrow {}^3F_2$	27.8	15	36.1	20	74.9	40.0
Nd $4f^3$	$^4I_{9/2} \rightarrow {}^4G_{5/2}$	135.0	120	195.4	330	444.0	530.0
Pm $4f^4$	$^5I_4 \rightarrow {}^5G_2$	104.7	--	125.3	--	260.0	--
Sm $4f^5$	$^6H_{5/2} \rightarrow {}^6F_{1/2}$	10.7	--	15.8	--	15.7	--
Eu $4f^6$	$^7F_0 \rightarrow {}^7F_2$	7.7	--	9.2	--	10.6	--
	$^7F_0 \rightarrow {}^5D_2$	0.4	--	0.5	--	0.90	--
Tb $4f^8$	$^7F_6 \rightarrow {}^7F_5$	4.8	--	6.0	--	10.0	--
Dy $4f^9$	$^6H_{15/2} \rightarrow {}^6F_{11/2}$	34.6	32	43.9	--	86.3	--
Ho $4f^{10}$	$^5I_8 \rightarrow {}^5G_6$	138.7	178	174.6	--	358.5	500.0
Er $4f^{11}$	$^4I_{15/2} \rightarrow {}^2H_{11/2}$	18.7	34	28.3	58	67.9	95.5
	$^4I_{15/2} \rightarrow {}^4G_{11/2}$	78.2	85	99.3	99	237.9	--
Tm$4f^{12}$	$^3H_6 \rightarrow {}^3H_4$	8.2	--	9.6	12	14.7	10.7
	$^3H_6 \rightarrow {}^3F_4$	13.5	12	15.6	15.3	32.6	25.3

[a] Experimental excitation energies are from Ref. [11].

[b] These data are the same as those in Table 4-1.

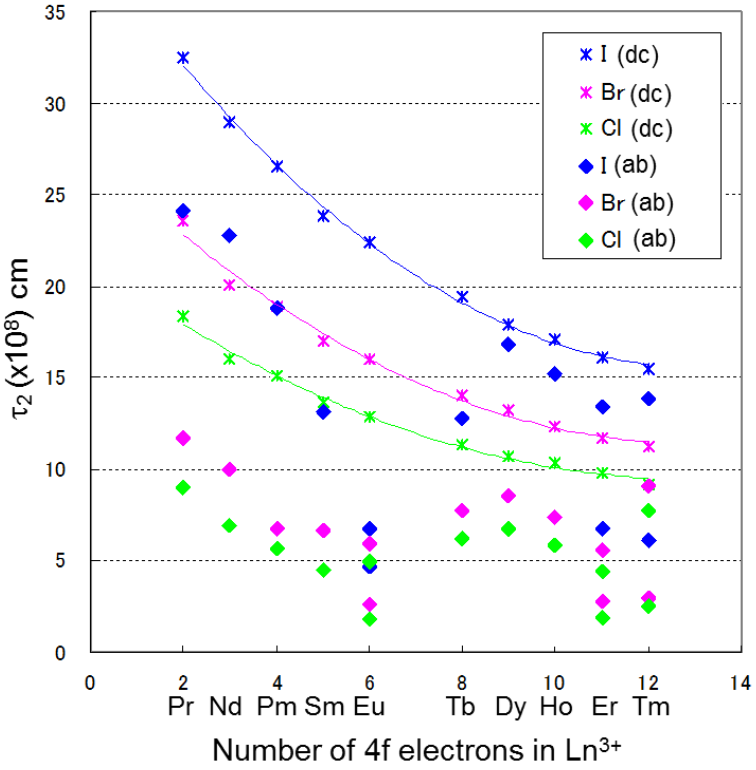

Figure 5-1: JO intensity parameters τ_2(dc) and τ_2(ab) of LnX_3 as functions of the number of 4f electrons

As shown in Figure 5-1, the τ_2(dc) value increases monotonically with the atomic number of halogen, because the polarizability of halogen increases monotonically. In comparison with τ_2(dc), τ_2(ab) values have similar halogen dependence, that is, both τ_2(dc) and τ_2(ab) increase as halogen changes from Cl to Br and to I. As mentioned in section 4.1.2, τ_2(ab) values have smaller than τ_2(dc) due to the polarization shielding effect, and the Ln dependence is different especially between Eu and Tb for all LnX_3 series.

It should be mentioned that the values of τ_2(ab) depend on the relative phase of each contribution because they are proportional to the squares of TDMs, which are expressed as $(\mathbf{M}^{IF}(\mathrm{JO}) + \mathbf{M}^{IF}(\mathrm{DC}) + \mathbf{M}^{IF}(\mathrm{LMCT}) + \cdots)^2$. Therefore, in the following section, the relation between the effect of the DC model and other effects is studied to demonstrate the cause of different behavior of the two kinds of τ_2.

Here, the relative weights given in Tables 4-2 and 4-3 and Figure 3-2 depend on basis sets, especially for those of matrix elements between Ln and X_3. In these analyses, they were calculated with a smaller basis set to represent only their valence space and to avoid ambiguity of determination of the region of Ln and X_3. However, it is impossible to leave no ambiguity in the division of transition populations. Therefore, other theoretical tools, which depend on the basis sets as little as possible, are devised and applied in the following sections.

5.2. Spatial Distribution of Integrand of Transition Density and Transition Dipole Moment

5.2.1. Calculation Methods

The author focuses on the spatial distribution of transition density and integrand of transition dipole moment (TDM) to minimize the basis set dependence. The transition

density and the integrand of the TDM are calculated for a pair of eigenstates which carries the largest TDM as in section 4.2.2.

The one-electron transition density function $\rho^{IF}(\mathbf{r})$ between the initial state Ψ_I and the final states Ψ_F of an *N*-electron system is defined as follows,

$$\rho^{IF}(\mathbf{r}_1) = N\int \Psi_I(\{\mathbf{r}_i\sigma_i\})\Psi_F(\{\mathbf{r}_i\sigma_i\})d\mathbf{r}_2\cdots d\mathbf{r}_N d\sigma_1\cdots d\sigma_N \tag{61}$$

Here, $\{\mathbf{r}_i\sigma_i\}$ stands for the electron coordinates collectively. To examine two-dimensional planar distribution of the transition density function, it is integrated in a direction perpendicular to the LnX_3 molecular plane to have a two-dimensional transition density function *D*(*x*,*y*) as follows,

$$D(x,y) = \int_{-\infty}^{\infty} \rho^{IF}(x,y,z)dz \tag{62}$$

The initial and final electronic wavefunctions Ψ_I and Ψ_F are calculated in the MRSOCI method and the above transition density functions are expanded with the basis of atomic orbitals (AOs) as follows,

$$\rho^{IF}(\mathbf{r}) = \sum_{t,s} \psi_t(\mathbf{r})\psi_s(\mathbf{r})\rho_{ts}^{IF} \tag{63}$$

where, the expansion coefficients ρ_{ts}^{IF} defined in eq. (63) are called the transition density matrix elements.

$$\rho_{ts}^{IF} = \sum_{i,j}^{\mathrm{MO}} c_{ti}c_{sj}\left\langle \Psi_I \left| \sum_{\sigma} a_{i\sigma}^{+}a_{j\sigma} \right| \Psi_F \right\rangle \tag{64}$$

In the same manner, two-dimensional transition density function *D*(*x*,*y*) can be expressed as follows,

$$D(x,y)=\sum_{t,s}^{\mathrm{AO}}\int_{-\infty}^{\infty}\left\{\psi_t(\mathbf{r})\,\psi_s(\mathbf{r})\rho_{ts}^{IF}\right\}dz\ . \tag{65}$$

Once these transition density functions are available, the x component TDM, for example, can be obtained by the following integrations,

$$\begin{aligned} M_x^{IF} &= \int x\rho^{IF}(x,y,z)\,dxdydz \\ &= \int xD(x,y)\,dxdy \end{aligned} \tag{66}$$

If these transition density functions are expressed in terms of AOs, the TDM can be expressed by the trace operation of the AO-basis transition density matrices and AO-basis dipole moment integrals, as follows,

$$M_x^{IF}=\sum_{t,s}^{\mathrm{AO}}\left\langle\psi_t\middle|x\middle|\psi_s\right\rangle\rho_{ts}^{IF}\ . \tag{67}$$

To examine the spatial distribution of the integrand of TDM, the integrand of the above AO-basis transition density matrices is integrated over the angular part to have a radial distribution function $r^2P(r)$ as follows,

$$\begin{aligned} M_x^{IF} &= \int_0^{\infty}\int_0^{\pi}\int_0^{2\pi}\sum_{t,s}^{\mathrm{AO}}\left\{\psi_t(\mathbf{r})\left(r\sin\theta\cos\phi\right)\psi_s(\mathbf{r})\rho_{ts}^{IF}\right\}r^2\sin\theta dr d\theta d\phi \\ &= \int_0^{\infty} r^2P(r)\,dr\ . \end{aligned} \tag{68}$$

Furthermore, these functions can be decomposed into three kinds of components based on the AO centers as follows,

$$D(x,y) = \int \sum_{t,s}^{\mathrm{AO}} \left\{ \psi_t(\mathbf{r})\, \psi_s(\mathbf{r}) \rho_{ts}^{IF} \right\} dz = \sum_{t,s}^{\mathrm{AO}} D_{t,s}(x,y)$$
$$= D_{\mathrm{LL}}(x,y) + D_{\mathrm{LX}}(x,y) + D_{\mathrm{XX}}(x,y)\,. \tag{69}$$

$$r^2 P(r) = \int_0^{\pi} \int_0^{2\pi} \sum_{t,s}^{\mathrm{AO}} \left\{ \psi_t(\mathbf{r}) \left(r \sin\theta \cos\phi \right) \psi_s(\mathbf{r}) \rho_{ts}^{IF} \right\} r^2 \sin\theta d\theta d\phi = \sum_{t,s}^{\mathrm{AO}} r^2 P_{t,s}(r)$$
$$= r^2 P_{\mathrm{LL}}(r) + r^2 P_{\mathrm{LX}}(r) + r^2 P_{\mathrm{XX}}(r)\,. \tag{70}$$

The values of the radial distribution functions of integrands of TDMs were calculated at 0.1 a.u. intervals for radial part and π/180 radian intervals for angular part, and then integrated numerically over the angular part. Those of the planar distribution functions of the transition densities were calculated at 0.1 a.u. intervals, and then integrated numerically over the perpendicular (*z*) direction. All the integrations were performed with the Wolfram Mathematica 7.0 program.

5.2.2. Results and Discussion

The planar distribution functions of the transition densities $D(x, y)$ of $PrBr_3$ are shown in Figure 5-2. Because the irreducible representation of the transition which carries the largest TDM is E*'*, the transition density functions $D(x,y)$ for the two kinds of transitions, called Type (x) and Type (y), are shown. The directions of TDMs are *x* and *y* for Type (x) and Type (y) transitions, respectively. Both of the transition densities have large values only around the position of Ln, which is located on the origin, because the initial and final state wavefunctions in the f-f transitions typically have reference

($4f^N$) weights higher than 0.95, as mentioned in section 4.2.2. The shapes of $D(x, y)$ suggest that they consist of transition quadrupole moments with components of x^2-y^2 and xy.

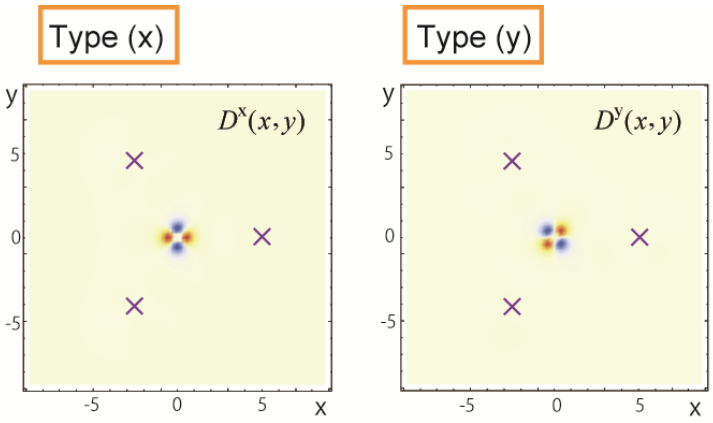

Figure 5-2: The planar distribution functions of transition densities $D(x, y)$ of $PrBr_3$. Red and blue areas represent positive and negative values, respectively. The x-marks represent the positions of Br atoms.

To observe the distribution of $D(x,y)$ around the halogen atoms more closely, those in the three regions (1), (2) and (3) are extended in Figure 5-3. As shown in Figure 5-3, the transition density in the regions (2) and (3) contains the components of the TDMs in the direction to the origin, but the sum of these two components cancel each other and the remaining components are shown as arrows in (2) and (3) in this Figure. Therefore, the transition moments on Br generate the crystal fields in the directions of x and y for Types (x) and (y) transitions, respectively. Moreover, the distribution of $D_{XX}(x,y)$, which is the components of $D(x,y)$ on the base of AOs on the ligands, is shown in Figure 5-4. The transition densities generated from intra-ligand transitions $D_{XX}(x,y)$ are

localized on the positions of three Br atoms and can be represented only by the intra-ligand excitations. These directions of the crystal fields are the same as those of the TDMs of f-f transitions. It suggests that the origin of f-f hypersensitive transition intensities can be understood by “the intensity borrowing” from the electric dipole transition intensities on the ligands.

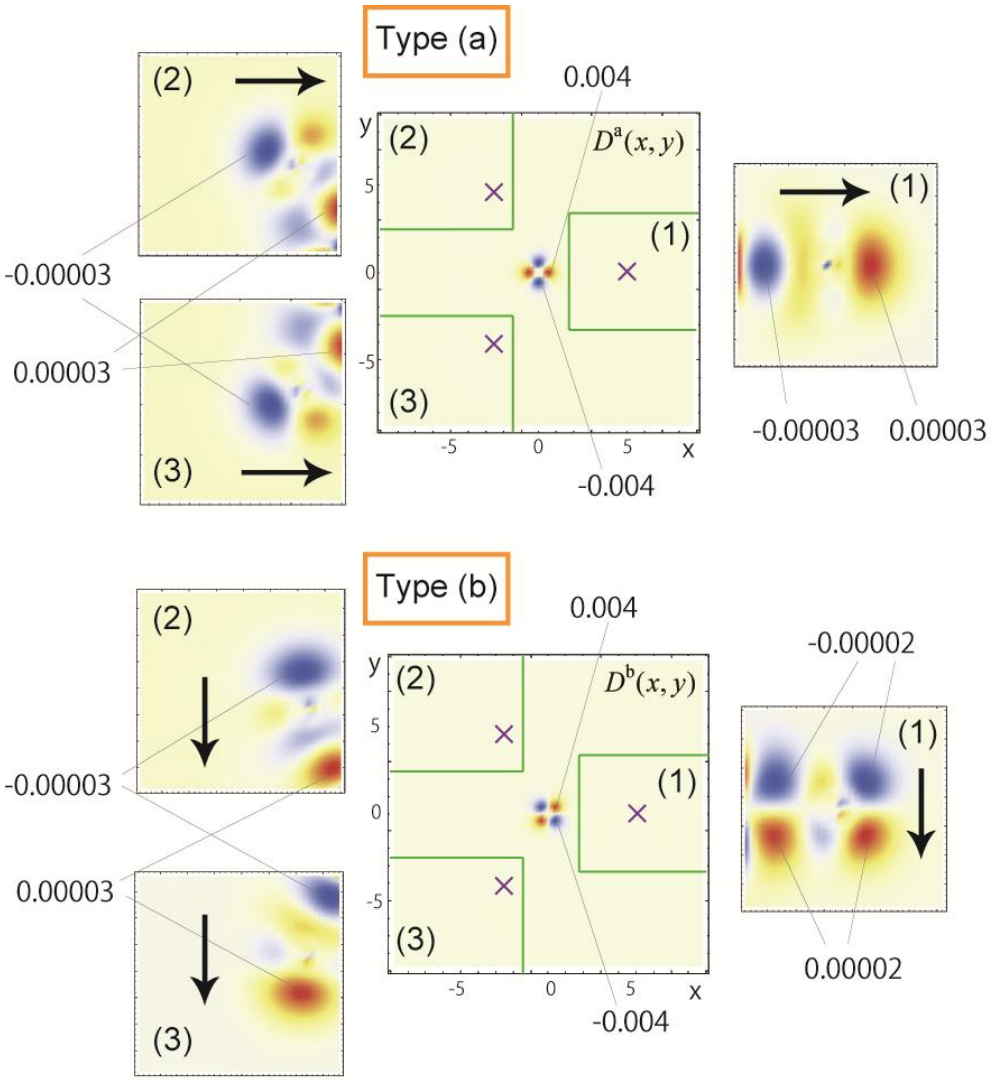

Figure 5-3: The extended views of $D(x,y)$ of $PrBr_3$. The x-marks represent the positions of Br atoms. The directions of arrows represent those of transition moments on Br atoms.

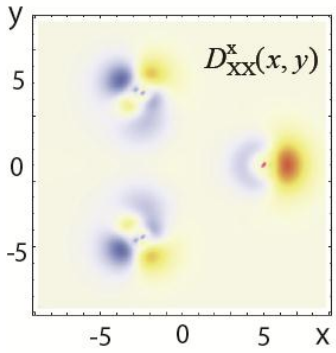

Figure 5-4: The planar distribution function of $D_{XX}(x,y)$ of $PrBr_3$ for Type (x) transition.

Recalling the coupling scheme in the DC model mentioned in section 2.1.3, the structures of the transition density around the Pr and Br atoms are quite similar to the structures shown in Figure 2-1 for the dynamic-coupling scheme caused by the periodically oscillating induced dipole moments on the ligands. This similarity of structures of the transition density between in Figure 5-3 and in Figure 2-1 is not a coincidence, since these two pictures express the same thing using the time-independent and time-dependent languages, respectively. If the time dependent wave functions of the initial and final states are denoted by

$$\Phi_I(\{\mathbf{r}_i\sigma_i\},t) = \Psi_I(\{\mathbf{r}_i\sigma_i\})\exp(-iE_I t/\hbar)\,, \tag{71}$$

$$\Phi_F(\{\mathbf{r}_i\sigma_i\},t) = \Psi_F(\{\mathbf{r}_i\sigma_i\})\exp(-iE_F t/\hbar)\,, \tag{72}$$

respectively, during the electronic excitation, the expectation value of the coordinate of a transient electron oscillates with the amplitude proportional to the following matrix element,

$$
\begin{aligned}
< \mathbf{r}(t) > &= \left\langle \Phi_F(\{\mathbf{r}_i\},t) \middle| \sum_i \mathbf{r}_i \middle| \Phi_I(\{\mathbf{r}_i\},t) \right\rangle \\
&= \left\langle \Psi_F(\{\mathbf{r}_i\}) \middle| \sum_i \mathbf{r} \middle| \Psi_I(\{\mathbf{r}_i\}) \right\rangle \exp\{i(E_F - E_I)t/\hbar\} ,
\end{aligned}
\tag{73}
$$

that is, for the *x* coordinate,

$$
\begin{aligned}
< x(t) > &= \iiint x\rho^{FI}(\mathbf{r}) d\mathbf{r} \cdot \exp\{i(E_F - E_I)t/\hbar\} \\
&= \iint xD^{x}(x,y) dxdy \cdot \exp\{i(E_F - E_I)t/\hbar\} \\
&= M_x^{IF} \cdot \exp\{i(E_F - E_I)t/\hbar\} .
\end{aligned}
\tag{74}
$$

where, E_F and E_I are the electronic energies of the final and initial states, respectively. As shown in eq. (74), the transient electron can oscillate when the TDM M_x^{IF} has a non-zero value, which has been confirmed from the above CI calculations. Therefore, the resonant excitation between the initial and final states can occur.

Next, the integrands of the TDMs are examined. As mentioned in section 5.2.1, the TDM can be expressed as a spatial integral of $D^{x}(x,y)$ multiplied by coordinate *x* or that of $D^{y}(x,y)$ multiplied by coordinate *y*. The planar distribution function of $xD^{x}(x,y)$ has large values around the localized region of Ln as shown in Figure 5-5. However, it can be considered from the shape of $xD^{x}(x,y)$ that the contribution from this region to the TDM is essentially zero, because the angular integration around this region must be canceled. Therefore, by integration over the angular part, the contribution from the regions (1), (2), and (3) may become relatively large.

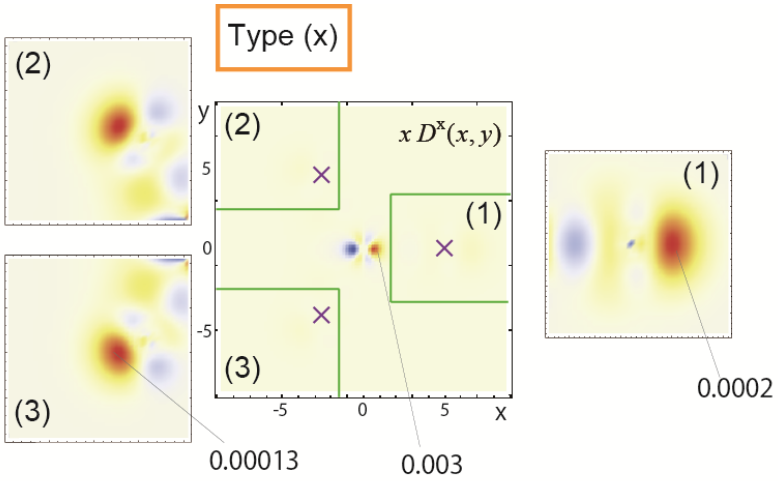

Figure 5-5: The planar distributions of $xD(x, y)$ of $PrBr_3$ for Type (x) transition.

From the above reason, the author focuses on the radial distribution functions of the integrand of TDM, which can be obtained by the multiplying $D(x, y)$ and the dipole operator x or y and integrating it over the angular part. It should be noted that the shape of radial distribution $r^2P(r)$ of Type (x) transition is exactly the same as that of Type (y) transition. The radial distribution functions $r^2P(r)$ of PrX_3 (X = Cl, Br, I) are shown in Figure 5-6. The nuclei are located at r = 0.0 for Pr, r = 4.8 for Cl, r = 5.1 for Br, and r = 5.5 a.u. for I, respectively. As shown in Figure 5-6, the curves of $r^2P(r)$ are not smooth around the position of the three halogen nuclei because the wavefunctions vary sharply near the nuclei. Comparing these functions suggests the general feature is independent of the halogens, that is, the values of $r^2P(r)$ are negative in the region of $0.8 < r < 3.5$ a.u., and are positive and large around in the region of $6 < r < 8$ a.u.

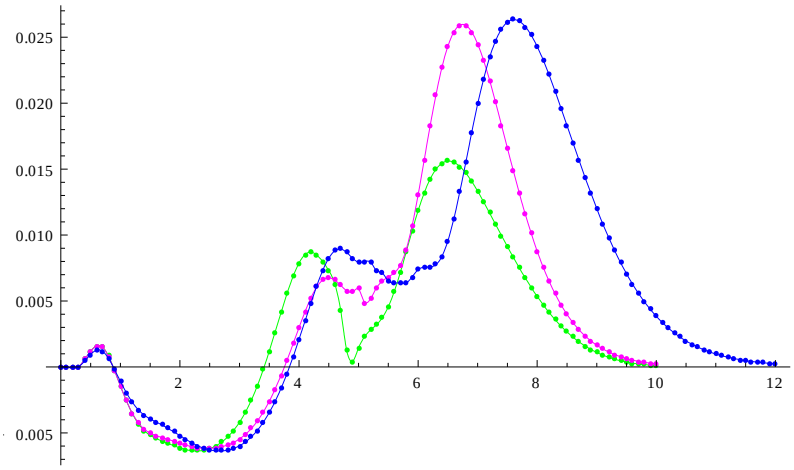

Figure 5-6 : Plots of the radial distribution functions $r^2P(r)$ vs r (in a.u.). Green, pink, and blue lines are those of $PrCl_3$, $PrBr_3$, and PrI_3, respectively.

To examine these functions more closely, they are decomposed into three components based on the AO centers, and shown in Figure 5-7. Here, the large values of $r^2P(r)$ in the region of 6 < r < 8 a.u. come from those of r^2P_{XX} (r), that is the contribution from the intra-ligand excitations.

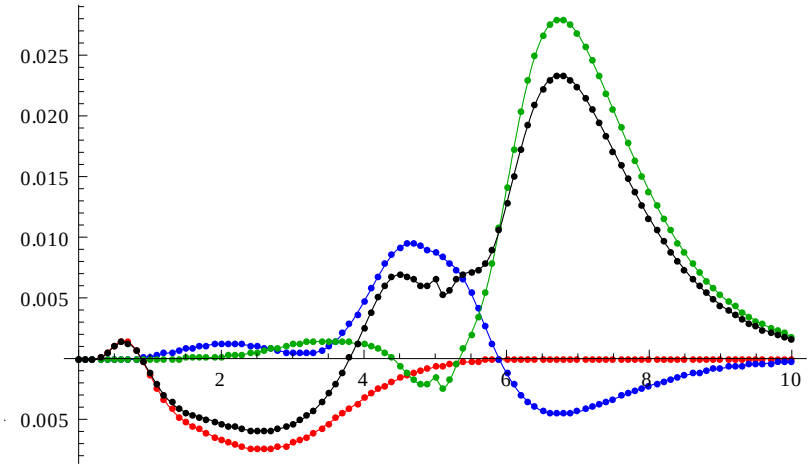

Figure 5-7 : Plots of $r^2P(r)$ and its components for $PrBr_3$. Red, blue, green, and black lines are those of $r^2P_{LL}(r)$, $r^2P_{LX}(r)$, $r^2P_{XX}(r)$ and their sum of $r^2P(r)$, respectively.

It should be noted that the area between the $r^2P(r)$ curve and the horizontal axis expresses the value of TDM because TDM can be obtained by integration of $r^2P(r)$ over r. Therefore, the region where $r^2P(r)$ has a positive value has a positive contribution to the TDM, and vice versa. It is also applies to the decomposed ones $r^2P_{t,s}(r)$. The areas of $r^2P_{\mathrm{LL}}(r)$, $r^2P_{\mathrm{LX}}(r)$ and $r^2P_{\mathrm{XX}}(r)$ represent the values of m(Ln,Ln), m(Ln,Br) + m(Br,Ln) and m(Br,Br) in Table 4-2, respectively.

Based on the above explanation, it can be noticed that the effect of m(Ln,Ln) has an opposite contribution against that of m(X,X) because the areas of $r^2P_{\mathrm{LL}}(r)$ and $r^2P_{\mathrm{XX}}(r)$ have opposite values. It suggests that the effect considered in the JO theory has an opposite contribution against that considered in the DC model. This sign relation has been pointed out in other studies based on experiments [67] or semi-empirical calculations using the crystal field theory [63],[68],[69].

The values of $r^2P_{\mathrm{LX}}(r)$ are very small in the region between Ln and Br. However, they are positive near the position of the ligands ($4 < r < 6$ a.u.), and are negative in the region outside the position of the ligands ($r > 6$ a.u.). In the current CI calculation, the AOs on Ln have non-zero population tail on the position of the ligands in a small measure. Therefore, the area of $r^2P_{\mathrm{LX}}(r)$ in the region of $r > 4$ a.u. can be regarded as a part of the effect considered in the DC model and the effect of the overlap between Ln and the ligands can be considered to be small. This result is consistent with the

assumption in the JO theory and the DC model where the effect of orbital overlap between metal and ligand, caused by back donation from X_3 to Ln, namely LMCT, was neglected. However, the importance of this effect was pointed out by Henrie *et al.* [30]. It may be considered that the qualitative difference between τ_2(ab) and τ_2 (dc) were partly caused by the effect of the orbital overlap.

Since the meaningful calculation of the overlap population is very difficult using basis set expansion methods, the author focuses attention on the Ln dependence on the shape of $r^2P(r)$. It can be expected that the shape of $r^2P(r)$ depends on Ln because the amount of LMCT configuration mixing is different among Ln, and are largest especially in Eu systems, as mentioned in section 4.2.2. To observe the dependence on Ln, $r^2P(r)$ for other $LnBr_3$ are shown in Figure 5-8. Contrary to the original expectation, the shape of $r^2P(r)$ is very similar among all the $LnBr_3$. Note that the ordinate of each figure is largely different reflecting the different magnitude of their oscillator strengths. The similarity of these functional forms suggests that the explicit effect on the TDM from the difference of the amount of LMCT is not large. Therefore, the author examines the effect of LMCT in a different perspective in the following section.

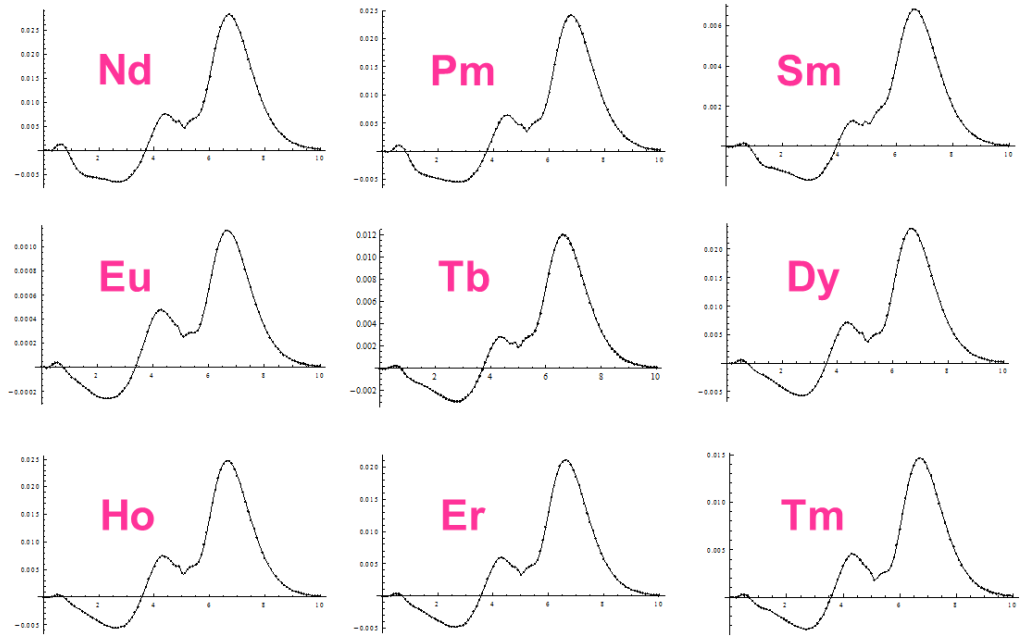

Figure 5-8 : Plots of $r^2P(r)$ for $LnBr_3$.

5.3. Effect of Ligand-to-Metal Charge Transfer

5.3.1. Definition of the Weight of Mixing of Ligand-to-Metal Charge Transfer

The author next tries to investigate the relation between τ_2(ab) and the amount of mixing of LMCT CSFs into the final state wavefunctions of the hypersensitive transitions. However, it was difficult to evaluate the amount of mixing directly because the virtual MOs had typically both components of Ln and Br. Additionally, the amount of mixing is too small to be analyzed because that of reference $4f^N$ CSFs is more than 0.95. Therefore, to remove the dominant 4f components, the author focuses attention on

the $N_{\mathrm{occ}} \times (N_{\mathrm{act}} + N_{\mathrm{vir}})$ rectangular block of transition density matrix elements T_{ij} which couple an initial state with a final state,

$$T_{ij} = \langle \Psi_I | \sum_{\sigma} a_{i\sigma}^{+} a_{j\sigma} | \Psi_F \rangle, \quad (i = 1, \cdots, N_{\mathrm{occ}},\ j = 1, \cdots, N_{\mathrm{act}} + N_{\mathrm{vir}}). \tag{75}$$

The rectangular block contains the relevant quantity associated with products of CI coefficients of the pairs of CSFs which are reference CSFs in Ψ_I and those for one-electron excitations from occupied MOs to (active + virtual) MOs in Ψ_F. As shown in section 4.2.2, about 90% of the total TDM comes from the classes between occupied and (active + virtual) MOs. It should be noted that in the following the author will focus on transition density, whereas in section 4.2.2, the author has focused on the product of transition density and dipole moment.

To represent the rectangular block transition density matrix **T** as compact as possible, "corresponding orbital" [70] or "natural transition orbital" [71] transformation [72] is carried out based on a singular value decomposition,

$$\left[\mathbf{U}^{+}\mathbf{T}\mathbf{V}\right]_{ij} = \lambda_i \delta_{ij}, \tag{76}$$

where $\mathbf{U} = (\mathbf{u}_1, \mathbf{u}_2, \cdots, \mathbf{u}_{N_{\mathrm{occ}}})$ and $\mathbf{V} = (\mathbf{v}_1, \mathbf{v}_2, \cdots, \mathbf{v}_{N_{\mathrm{act}}+N_{\mathrm{vir}}})$ are unitary matrices which can be determined by solving the eigenvalue equations as

$$\begin{aligned} (\mathbf{T}\mathbf{T}^{+})\mathbf{u}_i &= \lambda_i^2 \mathbf{u}_i \quad (i = 1, \cdots, N_{\mathrm{occ}}) \\ (\mathbf{T}^{+}\mathbf{T})\mathbf{v}_i &= \lambda_i^2 \mathbf{v}_i \quad (i = 1, \cdots, N_{\mathrm{act}} + N_{\mathrm{vir}}) \end{aligned}. \tag{77}$$

Here, the new set of occupied and (active + virtual) orbitals ψ_i, ψ'_i are obtained by using unitary transformations,

$$\begin{aligned}(\psi_1, \psi_2, \cdots, \psi_{N_{\mathrm{occ}}}) &= (\phi_1, \phi_2, \cdots, \phi_{N_{\mathrm{occ}}})\mathbf{U}, \\ (\psi'_1, \psi'_2, \cdots, \psi'_{N_{\mathrm{act}}+N_{\mathrm{vir}}}) &= (\phi'_1, \phi'_2, \cdots, \phi'_{N_{\mathrm{act}}+N_{\mathrm{vir}}})\mathbf{V}.\end{aligned} \tag{78}$$

These orbital sets (ψ_i, ψ'_i) whose matrix elements of $(\mathbf{U}^{+}\mathbf{T}\mathbf{V})_{ii}$ are λ_i are called particle-hole pairs. The importance of a particular particle-hole transition to the overall rectangular matrix **T** is reflected in the magnitude of the associated eigenvalue λ_i^2.

Next, the author evaluates a quantity of charge transfer from occupied orbitals of Br_3 in Ψ_I to active and virtual orbitals of Ln in Ψ_F. This quantity γ is evaluated by averaging the change of the charge population on Ln Δp_i^{Ln} with the associated weight of λ_i^2 as follows,

$$\begin{aligned}\gamma = \sum_i^{N_{\mathrm{occ}}} \lambda_i^2 \Delta p_i^{\mathrm{Ln}} \Big/ \sum_i^{N_{\mathrm{occ}}} \lambda_i^2 &= \sum_i^{N_{\mathrm{occ}}} \lambda_i^2 \left(p_i^{\mathrm{Ln}}(\mathrm{Final}) - p_i^{\mathrm{Ln}}(\mathrm{Initial})\right) \Big/ \sum_i^{N_{\mathrm{occ}}} \lambda_i^2 \\ &= -\sum_i^{N_{\mathrm{occ}}} \lambda_i^2 \left(p_i^{\mathrm{Br_3}}(\mathrm{Final}) - p_i^{\mathrm{Br_3}}(\mathrm{Initial})\right) \Big/ \sum_i^{N_{\mathrm{occ}}} \lambda_i^2\end{aligned}, \tag{79}$$

where p_i^{Ln} and $p_i^{\mathrm{Br_3}}$ are population of Ln and Br_3. The parameter γ of $LnBr_3$ takes a positive value because the amount of mixing of LMCT CSFs is much larger than that of MLCT CSFs. This weight of λ_i^2 is a 'diagonalized' transition density matrix element and has the information of the products of the CI coefficients between the reference CSFs in Ψ_I and those for intra-ligand excitations, LMCTs and so on in Ψ_F. With these weight factors, those LnX_3 with larger magnitude of LMCT CSFs are expected have a large value for γ.

Therefore it represents the weight of products of CI coefficients of the reference CSFs in Ψ_I and those for LMCT in Ψ_F whose TDMs have non-zero values. Additionally, the weight of products of CI coefficients of the reference CSFs in Ψ_I and those for other one-electron excitations in Ψ_F, especially intra-ligand excitations which have dominant contribution to TDMs, decreases relatively as γ increases.

5.3.2. Calculation of the Weight

The vales of γ along with τ_2(ab) for $LnBr_3$ are shown in Table 5-2. It can be seen that γ increases with the atomic number except between Eu and Tb. In general, the transition energies of the LMCT excited states in Ln systems become stabilized from Pr to Eu and once destabilized at Gd and then become stabilized again from Tb to Tm [66]. It was explained that those of Eu systems tend to be most stabilized because 4f electron configuration of Eu^{3+} becomes the $4f^7$ half-closed shell configuration by accepting one electron from ligands. It can be interpreted that γ increases as the energy gap between the final state of hypersensitive transition and LMCT state decreases.

Additionally, it can also be seen in Table 5-2 that τ_2(ab) decreases as γ increases. Here, the author focuses on the relation between TDMs and CI coefficients because τ_2(ab) are proportional to the squares of TDMs calculated with *ab initio* method. The CI coefficients of CSFs for LMCT from occupied orbitals of the Br_3 portion to 4f empty

orbitals of Ln have largest values among the LMCT CSFs. The TDMs between these LMCT CSFs and reference CSFs can be expressed as those between 4f orbitals and occupied orbitals of the Br_3 portion.

Table 5-2 : Relation between the weights of LMCT configurations in final states of hypersensitive transitions γ and $\tau_2(\mathrm{ab}) \times 10^8$ of $LnBr_3$

Ln	Transitions	γ	τ_2(ab)
Pr $4f^2$	$^3H_4 \rightarrow {}^3F_2$	0.22	11.7
Nd $4f^3$	$^4I_{9/2} \rightarrow {}^4G_{5/2}$	0.28	10.0
Pm $4f^4$	$^5I_4 \rightarrow {}^5G_2$	0.29	6.8
Sm $4f^5$	$^6H_{5/2} \rightarrow {}^6F_{1/2}$	0.33	6.7
Eu $4f^6$	$^7F_0 \rightarrow {}^7F_2$	0.34	5.9
	$^7F_0 \rightarrow {}^5D_2$	0.69	2.6
Tb $4f^8$	$^7F_6 \rightarrow {}^7F_5$	0.17	7.7
Dy $4f^9$	$^6H_{15/2} \rightarrow {}^6F_{11/2}$	0.25	8.6
Ho $4f^{10}$	$^5I_8 \rightarrow {}^5G_6$	0.37	7.4
Er $4f^{11}$	$^4I_{15/2} \rightarrow {}^2H_{11/2}$	0.35	2.9
	$^4I_{15/2} \rightarrow {}^4G_{11/2}$	0.38	5.6
Tm $4f^{12}$	$^3H_6 \rightarrow {}^3H_4$	0.21	9.1
	$^3H_6 \rightarrow {}^3F_4$	0.29	2.9

Because TDMs caused by LMCT have values reflecting overlaps between the two orbitals, their values depend on the size of these orbitals. The radial expectation values of 4f orbital of Pr^{3+} and 4p orbital of Br^- were 1.0 and 1.9 bohr, respectively, and in reasonable agreement with relativistic ones by Desclaux [73], 1.1 and 2.1 bohr.

Considering the distance between Ln and Br which is about 5 bohr, these orbitals have little overlap. Therefore TDMs between these orbitals are negligibly small compared to those for intra-ligand excitations within Br_3. To sum up, the TDM decreases as γ increases because as the weights of LMCT CSFs with a negligibly small contribution to TDMs increase, those of intra-ligand excitation CSFs having large TDMs decrease as discussed briefly in section 4.2.2.

By taking these factors into account, the reason why τ_2(ab) of $EuBr_3$ has a smaller value than that of $TbBr_3$ can be explained by the fact that the relative importance of the intra-ligand excitation CSFs is reduced by the increase of the 'dark' LMCT CSFs, especially those from occupied orbitals of ligands to 4f orbitals of Ln. As seen above, the values of TDMs and τ_2(ab) cannot be explained only by the DC model and the mixing of LMCT CSFs to $4f^N$ states should be considered simultaneously.

Recalling the explanation for Figures 5-7, the amount of contribution from the region of the overlap between Ln and the ligands ($1 < r < 4.5$ a.u.) was independent of Ln, though the mixing of LMCT CSFs should depend on Ln. It can be understood that the difference of the amount of LMCT from occupied orbitals of the Br_3 portion to 4f empty orbitals of Ln cannot affect the values of TDM and the radial distribution functions $r^2P(r)$ because of the negligible small overlap between these orbitals.

To summarize the analysis so far, the relative phase between each contribution to the TDM is expressed as

$$\mathbf{M}^{IF}(\mathrm{ab}) = \left|\mathbf{M}^{IF}(\mathrm{DC})\right| - \left|\mathbf{M}^{IF}(\mathrm{JO})\right| + \cdots, \tag{80}$$

and the CSFs which represent LMCT from X_3 to 4f empty orbitals of Ln and intra-Ln transition from occupied 5s and 5p orbitals to virtual orbitals of Ln contribute to the TDM as "drak" states. Here, it should be noted about the relation of energy levels of excited states of LMCT and $4f^{N-1}nd$. It is well known that the excitation energies of LMCT excited states become stabilized from Pr to Eu and once destabilized from Eu to Tb and stabilized again from Tb to Tm. On the other hand, those of $4f^{N-1}5d$ states are known to display an opposite behavior. They become destabilized from Pr to Eu and once stabilized from Eu to Tb and destabilized again from Tb to Tm. Considering the behavior of τ_2(ab), the difference of the LMCT excitation energies across Ln has more strong impact to TDMs than that of $4f^{N-1}5d$ states. This phenomenon can be understood because the LMCT excitation energies are lower than those of $4f^{N-1}5d$ states. Taken altogether, the difference of the excitation energies of $4f^{N-1}5d$ and LMCT states could affect the behavior of τ_2(ab) and it is considered that the behaviors of τ_2(ab) depend on the Ln systems because the difference of these excitation energies depends heavily on the systems. Therefore, it is clarified that the mixing of LMCT and intra-Ln excitation configurations also affects the intensities and they must be considered simultaneously.

Chapter 6

General Conclusions

In this study, the oscillator strengths of f-f transitions of lanthanide trihalide LnX_3 (Ln = Pr, Nd, Pm, Sm, Eu, Tb, Dy, Ho, Er, Tm; X = Cl, Br, I) molecules were calculated with the multi-reference spin-orbit configuration interaction method. First of all, a program to compute the transition density matrix with the graphical unitary group approach (GUGA) was coded and attached to the COLUMBUS program package. The oscillator strengths of both hypersensitive transitions and non-hypersensitive ones could be obtained quantitatively with this program even though the values are as small as 10^{-6} to 10^{-4}.

Secondly, the origin of f-f transition intensities was examined by focusing on the effect of molecular vibration and f-d mixing and it was concluded that these effects had negligibly small contributions. Thirdly, the oscillator strengths were decomposed into four types of matrix elements to clarify which matrix elements have a major contribution to the oscillator strengths, and it was clarified that the matrix elements

between two atomic orbitals on halogens had dominant contributions to the oscillator strengths for most f-f transitions including hypersensitive ones. It suggests that the matrix elements between the reference $4f^N$ configurations and intra-ligand excitation configurations had dominant contributions to the oscillator strengths and this is consistent with the explanation of the dynamic-coupling (DC) model.

To investigate the origin of f-f transition intensities in more detail, the Judd-Ofelt intensity parameters were evaluated with two methods: τ_2(ab) obtained with the MRSOCI method and τ_2(dc) obtained based on the dynamic-coupling model. Although τ_2(dc) had larger values than τ_2(ab) due to the neglect of the polarization shielding effect, their overall Ln dependence was similar except between Eu and Tb. It is suggested that the origin of f-f transition intensities could be explained mostly with the DC model.

To look more closely, the planar distribution functions of transition density were examined and it can be confirmed that the current time-independent CI calculation can contain the effect of time-dependent crystal field mentioned in the DC model. Additionally, the radial distribution functions of transition dipole moment contained in hypersensitive transitions were examined and it is concluded that the origin of f-f intensities are independent of the kinds of Ln and halogens and the contributions generated by the point charges on the ligands, which are described by the Judd-Ofelt

theory, are smaller and opposite sign compared with those by the oscillating induced dipole moments on the ligands.

Furthermore, the amount of configuration mixing of LMCT was investigated, and it can be explained that the differences between τ_2(ab) and τ_2(dc) are largest in EuX_3 because the configuration mixing of LMCT from X_3 to 4f empty orbitals of Ln, whose matrix elements of TDM is negligibly small, is largest in EuX_3 and the contributions from the DC model are reduced due to the decrease of configuration mixing of intra-ligand excitations.

As seen so far, the dominant mechanism is the dynamical polarization effects within X_3 and to a lesser extent, the intra-Ln excitation and LMCT mechanism. It can be understood that the excitation energies are insensitive to a change of surrounding environment because the dominant configurations of $4f^N$ states are reference $4f^N$ configurations. On the other hands, the intensities of hypersensitive transitions are sensitive to a small change of environment because the minor configurations such as intra-ligand excitations, which are reflected directly by a change of surrounding environment, have dominant contributions to the oscillator strengths. Additionally, the reason why hypersensitive transitions of gaseous LnX_3 are about 100 times stronger than those in aquo can be explained from the formula of τ_2(dc), which contains the inverse of internuclear distance between lanthanide and ligands and the polarizability of

ligands. In general, these internuclear distances are larger in Ln^{3+} in solutions than in molecules containing Ln, and the polarizability of water are smaller than that of typical ligand molecules. Therefore, the Coulomb correlation between transition quadrupole moment of Ln and induced dipole moment of ligands must be weaker in aquo. It can be understood that this effect is one of the examples of near-field effects, which have recently gained much attention in the field of surface chemistry.

These findings will be applied for the theoretical calculation of realistic large molecules containing Ln, such as biosensors. Recently, the hybrid quantum mechanics/ molecular mechanics (QM/MM) approaches are used extensively in the case of large systems whose computational efforts are too large to be calculated with high accuracy *ab initio* methods. When such hybrid calculation methods are carried out, the effect of surrounding environment should be considered efficiently. In other words, the essential quality of f-f transition should be represented with the MM calculation, which contains the crystal field effect generated by the point charges around Ln. However, the essential quality of f-f transition intensities must not be represented without the MM calculation, which contains the crystal field effect generated by the induced dipole moments around Ln.

As seen so far, the author succeeded in calculation of f-f hypersensitive transition intensities and clarified their comprehensive mechanisms with high accuracy *ab initio* method for the first time.

References

[1] P. A. M. Dirac, Proc. Roy. Soc. A 123 (1929) 714.

[2] S. V. Eliseeva, J.-C. G. Bünzli, Chem. Soc. Rev. 39 (2010) 189.

[3] K. Binnemans, Chem. Rev. 109 (2009) 4283.

[4] J.-C. G. Bünzli, S. Comby, A.-S. Chauvin, D. B. Vandevy, J. Rare Earths 25 (2007) 257.

[5] S. Cotton, *Lanthanide And Actinide Chemistry*, John Wiley & Sons, Chichester, U. K., 2006.

[6] B. R. Judd, Phys. Rev. 127 (1962) 750.

[7] G. S. Ofelt, J. Chem. Phys. 37 (1962) 511.

[8] C. Görller-Varland, K. Binnemans, Spectral intensities of f-f transitions. In *Handbook on the Physics and Chemistry of Rare-Earths*; K. A. Gschneider, L. Eyring Eds.; Elsevier: Amsterdam, 1998; vol. 25, pp. 101-264.

[9] C. K. Jørgensen, B. R. Judd, Mol. Phys. 8 (1964) 281.

[10] D. M. Gruen, C. W. DeKock, J. Chem. Phys. 45 (1966) 455.

[11] D. M. Gruen, C. W. DeKock, R. L. McBeth, Adv. Chem. Ser. 71 (1967) 102.

[12] S. F. Mason, R. D. Peacock, B. Stewart, Mol. Phys. 30 (1975) 1829.

[13] S. F. Mason, R. D. Peacock, B. Stewart, Chem. Phys. Lett. 29 (1974) 149.

[14] R. D. Peacock, Mol. Phys. 33 (1977) 1239.

[15] R. D. Peacock, J. Mol. Struct. 46 (1978) 203.

[16] T. R. Cundari, S. O. Sommerer, L. A. Strohecker, L. Tippett, J. Chem. Phys. 103 (1995) 7058.

[17] L. Joubert, G. Picard, J-J. Legendre, Inorg. Chem. 37 (1998) 1984.

[18] T, Tsuchiya, T. Taketsugu, H. Nakano, K. Hirao, J. Mol. Struct. (Theochem) 461-462 (1999) 203.

[19] C. Clavaguéra, J.-P. Dogonon, P. Pyykkö, Chem. Phys. Lett. 429 (2006) 8.

[20] G. Lanza, Z. Varga, M. Kolonits, M. Hargittai, J. Chem. Phys. 128 (2008) 074301.

[21] S. Tsukamoto, H. Mori, H. Tatewaki, E. Miyoshi, Chem. Phys. Lett. 474 (2009) 28.

[22] A. B. Muńoz-Garcia, J. L. Pascual, Z. Barandiarán, L. Seijo, Phys. Rev. B 82 (2010) 064114.

[23] Y. Yang, R. M. Pitzer, J. Phys. Chem. A 114 (2010) 7117.

[24] K. Balasubramanian, *Relativistic Effects in Chemistry Part A. Theory & Techniques*, John Wiley & Sons, New York, 1997.

[25] S. Yabushita, Z. Zhang, R. M. Pitzer, J. Phys. Chem. A 103 (1999) 5791.

[26] B. R. Judd, J. Chem. Phys. 44 (1966) 839.

[27] W. C. Nieuwport, G. Blasse, Solid State Commun. 4 (1966) 227.

[28] D. E. Henrie, G. R. Choppin, J. Chem. Phys. 49 (1968) 477.

[29] R. D. Peacock, Struct. Bonding 22 (1975) 83.

[30] D. E. Henrie, G. R. Coord. Chem. 18 (1976) 199.

[31] E. G. Höhn, O. E. Weigang Jr. J. Chem. Phys. 48 (1968) 1127.

[32] S. F. Mason, G. W. Vane, J. Chem. Soc. (B) (1966) 370.

[33] W. T. Carnall, P. R. Firlds, K. Rajnak, J. Chem. Phys. 49 (1968) 4424.

[34] W. T. Carnall, P. R. Firlds, K. Rajnak, J. Chem. Phys. 49 (1968) 4447.

[35] W. T. Carnall, P. R. Firlds, K. Rajnak, J. Chem. Phys. 49 (1968) 4450.

[36] W. T. Carnall, P. R. Firlds, B. G. Wybourne, J. Chem. Phys. 42 (1965) 3797.

[37] P. Jørgensen, J. Simons, *Second Quantization-Based Methods in Quantum Chemistry*, Academic Press, New York, 1981.

[38] J. Paldus, Unitary Group Approach to Many-Electron Correlation Problem. In *The Unitary Group for the Evaluation of Electronic Energy Matrix Elements*; Hinze, J., Ed.; Lecture Notes in Chemistry 22; Springer: Berlin, 1981; 1−50.

[39] I. Shavitt, The Graphical Unitary Group Approach and its Application to Direct Configuration Iinteraction Calculations. In *The Unitary Group for the Evaluation of Electronic Energy Matrix Elements*; Hinze, J., Ed.; Lecture Notes in Chemistry 22; Springer: Berlin, 1981; 51−99.

[40] I. Shavitt, Unitary group approach to configuration interaction calculations of the electronic structure of atoms and molecules. In *Mathematical Frontiers in Computational Chemical Physics*; Truhlar, D. G., Ed.; Springer: Berlin, 1988; pp 300−349.

[41] T. Inui, Y. Tanabe, K. Onodera, *Ouyou Gunron,* Shoukabou, Toko, 1980 (in Japanese).

[42] R. Shepard, I. Shavitt, R. M. Pitzer, D. C. Comeau, M. Pepper, H. Lischka, P. G. Szalay, R. Ahlrichs, F. B. Brown, J.-G. Zhao, Int. J. Quantum Chem. Symp. 22 (1988) 149.

[43] M. Hargittai, Coord. Chem. Rev. 91 (1988) 35.

[44] M. W. Schmidt, K. K. Baldridge, J. A. Boatz, S. T. Elbert, M. S. Gordon,J. H. Jensen, S. Koseki, N. Matsunaga, K. A. Nguyen, S. Su, T. L. Windus, M. Dupuis, J. A. Montgomery, J. Comput. Chem. 14 (1993) 1347.

[45] Y. Sakai, E. Miyoshi, H. Tatewaki, J. Mol. Struct.: THEOCHEM 451 (1998) 143.

[46] E. Miyoshi, Y. Sakai, K. Tanaka, M. Masamura, J. Mol. Struct: THEOCHEM 451 (1998) 73.

[47] MCP online library: http://meg.cube.kyushu-u.ac.jp/~meg/MCP1.html

[48] W. R. Wadt, Chem. Phys. Lett. 89 (1982) 245.

[49] W. C. Martin, R. Zalubas, L. Hagan, *Atomic Energy Levels - The Rare-Earth Elements : The Spectra of Lanthanum, Cerium, Praseodymium, Neodymium, Promethium, Samarium, Europium, Gadolinium, Terbium, Dysprosium, Holmium, Erbium, Thulium, Ytterbium, and Lutetium*; National Bureau of Standards, Washington D. C., 1978.

[50] C. E. Moore, *Atomic energy levels as derived from the analysis of optical spectra vol. 2-3*; National Bureau of Standards: Washington D. C., 1971.

[51] K. Saito, Y. Eishiro, Y. Nakao, H. Sato, S. Sakaki, Annual Meeting of Japan Society for Molecular Science 2008, 1E18 (in Japanese) : and the private discussion.

[52] E. A. McCullough, R. E. Wyatt, J. Chem. Phys. 54 (1971) 3578.

[53] C. Cerjan, K. C. Kulander, Comput. Phys. Commun. 63 (1991) 529.

[54] Sugawara, M.; Kato, M.; Fujimura, Y. Chem. Phys. Lett. 184 (1991) 203.

[55] N. I. Giricheva, G. V. Girichev, S. A. Shlykov, A. V. Krasnov, A. V. Zakharov, O. G. Krasnova, J. Struct. Chem. 45 (2004) 47.

[56] MCP online library: http://setani.sci.hokudai.ac.jp/sapporo/

[57] E. Sanoyama, H. Kobayashi, S. Yabushita, J. Mol. Struct (Theochem) 451 (1998) 189.

[58] A. Dalgarno, Advances in Phys. 11 (1962) 281.

[59] S. S. Jaswal, T. P. Sharma, J. Phys. Chem. Solids 34 (1973) 509.

[60] C. J. Lenander, E. Y. Wong, J. Chem. Phys. 38 (1963) 2750.

[61] A. J. Freeman, R. E. Watson, Phys. Rev. 139 (1965) A1606.

[62] B. R. Judd, J. Chem. Phys. 70 (1979) 4830.

[63] O. L. Malta, S. J. L. Ribeiro, M. Faucher, P. Porcher, J. Phys. Chem. Solids 52 (1991) 587.

[64] J. Blok, D. A. Shirley, Phys. Rev. 143 (1966) 278.

[65] R. M. Sternheimer, Phys. Rev. 146 (1966) 140.

[66] P. Dorenbos, J. Alloys. Compd. 488 (2009) 568.

[67] O. L. Malta, M. A. Couto dos Santos, L. C. Thompson, N. K. Ito, J. Lumin. 69 (1996) 77.

[68] S.-D. Xia, M. F. Reid, J. Phys. Chem. Sol.54 (1993) 777.

[69] L. Smentek-Mielczarek, Phys. Rev. B 48 (1993) 9273.

[70] A. Amos, G. G. Hall, Proc. R. Soc. A 263 (1961) 483.

[71] R. L. Martin, J. Chem. Phys. 118 (2003) 4775.

[72] I. Mayer, Chem. Phys. Lett. 437 (2007) 284.

[73] J. P. Desclaux, At. Data Nucl. Data Tables 12 (1973) 311.

Appendix

A table of decomposition of TDM integrals (in %) based on the MO classes and the AO centers for $PrBr_3$ is give as Table 4-2 in chapter 4.2.2. The same type of tables for other $LnBr_3$ (Ln = Nd, Pm, Sm, Eu, Tb, Dy, Ho, Er, and Tm) are given in this appendix. Notations and footnotes in each table are the same as Table 4-2.

Table A-1：Decomposition of TDM integrals (in percent) based on the MO classes and the AO centers for $NdBr_3$. [a,b]

	m(Ln,Ln)	*m*(Br,Br)	*m*(Br,Ln)	*m*(Ln,Br)	Total
μ(occ, vir)	-4.0	***45.8*** [c]	**3.9** [d]	**1.4** [e]	47.0
μ(vir, occ)	-2.0	***42.2*** [c]	**-0.5** [e]	**-3.6** [d]	36.1
μ(occ, act)	-0.9	7.3	**-1.3** [d]	2.1	7.2
μ(act, occ)	0.0	3.5	1.1	**-0.5** [d]	4.2
μ(vir, act)	**1.9** [f]	-0.3	**-0.1** [e]	0.2	1.7
μ(act, vir)	**-1.5** [f]	0.4	-0.2	**0.0** [e]	-1.3
μ(vir, vir)	0.0	0.5	-0.2	-0.2	0.0
μ(act, act)	**-9.1** [f]	18.0	-3.7	-2.9	2.2
μ(occ, occ)	0.2	2.6	0.1	0.2	3.0
Total	-15.4	119.9	-1.1	-3.5	100.0

Table A-2： Decomposition of TDM integrals (in percent) based on the MO classes and the AO centers for $PmBr_3$. [a,b]

	m(Ln,Ln)	*m*(Br,Br)	*m*(Br,Ln)	*m*(Ln,Br)	Total
μ(occ, vir)	-4.0	***44.4*** [c]	**8.0** [d]	**2.7** [e]	51.1
μ(vir, occ)	-3.0	***41.1*** [c]	**0.2** [e]	**-2.6** [d]	35.7
μ(occ, act)	-0.1	6.2	**-0.7** [d]	1.7	7.1
μ(act, occ)	0.0	2.3	1.0	**-0.4** [d]	2.9
μ(vir, act)	**1.0** [f]	0.0	**-0.1** [e]	0.1	1.0
μ(act, vir)	**-2.1** [f]	0.4	-0.3	**0.0** [e]	-1.9
μ(vir, vir)	-0.2	0.1	-0.1	-0.1	-0.3
μ(act, act)	**-7.9** [f]	16.4	-2.3	-3.2	3.0
μ(occ, occ)	0.1	0.9	0.1	0.1	1.3
Total	-16.2	111.9	5.9	-1.6	100.0

Table A-3 : Decomposition of TDM integrals (in percent) based on the MO classes and the AO centers for $SmBr_3$. [a,b]

	m(Ln,Ln)	*m*(Br,Br)	*m*(Br,Ln)	*m*(Ln,Br)	Total
μ(occ, vir)	-2.3	***41.8*** [c]	**3.1** [d]	**1.3** [e]	43.8
μ(vir, occ)	-3.1	***41.4*** [c]	**0.6** [e]	**-0.8** [d]	38.1
μ(occ, act)	0.2	4.9	**-0.5** [d]	1.8	6.4
μ(act, occ)	-0.8	5.4	1.2	**-1.1** [d]	4.7
μ(vir, act)	**0.9** [f]	0.0	**-0.1** [e]	0.2	1.0
μ(act, vir)	**-1.0** [f]	0.4	-0.2	**0.0** [e]	-0.8
μ(vir, vir)	-0.2	0.0	-0.1	-0.1	-0.4
μ(act, act)	**-8.4** [f]	21.9	-2.8	-5.1	5.6
μ(occ, occ)	-0.1	1.3	0.1	0.3	1.6
Total	-14.7	117.0	1.2	-3.5	100.0

Table A-4 : Decomposition of TDM integrals (in percent) based on the MO classes and the AO centers for $EuBr_3$ for $^7F_0 \rightarrow {}^7F_{2.}$ [a,b]

	m(Ln,Ln)	*m*(Br,Br)	*m*(Br,Ln)	*m*(Ln,Br)	Total
μ(occ, vir)	-1.7	***35.7*** [c]	**2.2** [d]	**1.4** [e]	37.6
μ(vir, occ)	-2.8	***33.8*** [c]	**0.9** [e]	**-0.5** [d]	31.3
μ(occ, act)	0.2	11.2	**-1.1** [d]	0.8	11.2
μ(act, occ)	-1.6	8.1	1.0	**-1.7** [d]	5.7
μ(vir, act)	**0.5** [f]	0.2	**-0.1** [e]	0.0	0.6
μ(act, vir)	**0.0** [f]	0.1	-0.1	**0.1** [e]	0.0
μ(vir, vir)	-0.1	0.2	-0.2	-0.2	-0.3
μ(act, act)	**-6.0** [f]	18.1	-1.7	-4.6	5.9
μ(occ, occ)	0.1	7.6	0.2	0.2	8.0
Total	-11.4	114.9	1.0	-4.5	100.0

Table A-5 : Decomposition of TDM integrals (in percent) based on the MO classes and the AO centers for $EuBr_3$ for $^7F_0 \rightarrow {}^5D_{2.}$ [a,b]

	m(Ln,Ln)	*m*(Br,Br)	*m*(Br,Ln)	*m*(Ln,Br)	Total
μ(occ, vir)	-2.1	***29.0*** [c]	**5.2** [d]	**2.4** [e]	34.5
μ(vir, occ)	-1.4	***21.2*** [c]	**0.4** [e]	**-1.2** [d]	19.0
μ(occ, act)	-0.5	27.0	**-3.3** [d]	-0.5	22.7
μ(act, occ)	-0.9	7.8	-0.2	**-1.3** [d]	5.4
μ(vir, act)	**0.6** [f]	1.0	**-0.1** [e]	-0.7	0.9
μ(act, vir)	**-1.7** [f]	1.9	-1.2	**-0.3** [e]	-1.2
μ(vir, vir)	-0.8	-0.4	0.2	0.5	-0.5
μ(act, act)	**-3.7** [f]	11.2	-1.4	-2.4	3.7
μ(occ, occ)	-0.1	15.3	0.2	0.2	15.6
Total	-10.7	114.1	-0.2	-3.3	100.0

Table A-6 : Decomposition of TDM integrals (in percent) based on the MO classes and the AO centers for $TbBr_3$. [a,b]

	m(Ln,Ln)	*m*(Br,Br)	*m*(Br,Ln)	*m*(Ln,Br)	Total
μ(occ, vir)	-3.2	***44.7*** [c]	**5.4** [d]	**0.0** [e]	46.9
μ(vir, occ)	-4.9	***45.4*** [c]	**0.1** [e]	**2.5** [d]	43.1
μ(occ, act)	0.3	0.6	**0.0** [d]	0.3	1.2
μ(act, occ)	-0.4	0.3	0.5	**-0.1** [d]	0.3
μ(vir, act)	**0.2** [f]	3.0	**-0.3** [e]	-1.6	1.3
μ(act, vir)	**-0.8** [f]	2.8	-1.0	**-0.4** [e]	0.6
μ(vir, vir)	-0.3	-0.5	0.4	0.4	0.0
μ(act, act)	**-4.2** [f]	14.4	-1.0	-3.4	5.8
μ(occ, occ)	-0.1	0.9	0.0	0.0	0.8
Total	-13.4	111.5	4.2	-2.2	100.0

Table A-7 : Decomposition of TDM integrals (in percent) based on the MO classes and the AO centers for $DyBr_3$. [a,b]

	m(Ln,Ln)	*m*(Br,Br)	*m*(Br,Ln)	*m*(Ln,Br)	Total
μ(occ, vir)	-3.1	***40.2*** [c]	**1.3** [d]	**2.0** [e]	40.4
μ(vir, occ)	-1.7	***39.2*** [c]	**1.7** [e]	**1.6** [d]	40.9
μ(occ, act)	-0.9	4.2	**-0.8** [d]	0.4	2.9
μ(act, occ)	0.0	4.8	-0.1	**-0.5** [d]	4.2
μ(vir, act)	**0.3** [f]	2.4	**-0.4** [e]	-1.0	1.2
μ(act, vir)	**0.1** [f]	3.1	-1.7	**-0.3** [e]	1.2
μ(vir, vir)	0.0	-0.1	0.1	0.1	0.1
μ(act, act)	**-4.7** [f]	14.6	-3.2	-1.4	5.3
μ(occ, occ)	0.0	3.7	0.0	0.1	3.8
Total	-10.1	112.1	-3.0	1.0	100.0

Table A-8 : Decomposition of TDM integrals (in percent) based on the MO classes and the AO centers for $HoBr_3$. [a,b]

	m(Ln,Ln)	*m*(Br,Br)	*m*(Br,Ln)	*m*(Ln,Br)	Total
μ(occ, vir)	-4.6	***45.4*** [c]	**7.8** [d]	**3.6** [e]	52.2
μ(vir, occ)	-2.3	***35.7*** [c]	**1.0** [e]	**-0.2** [d]	34.2
μ(occ, act)	-1.0	5.0	**-0.8** [d]	0.5	3.7
μ(act, occ)	-0.2	2.3	0.0	**-0.3** [d]	1.8
μ(vir, act)	**0.6** [f]	1.6	**-0.3** [e]	-0.7	1.3
μ(act, vir)	**-0.2** [f]	2.4	-1.2	**-0.3** [e]	0.8
μ(vir, vir)	0.0	-0.2	0.1	0.1	0.1
μ(act, act)	**-3.5** [f]	8.1	-1.6	-1.1	2.0
μ(occ, occ)	0.0	3.8	0.1	0.1	4.0
Total	-11.2	104.2	5.2	1.8	100.0

Table A-9 : Decomposition of TDM integrals (in percent) based on the MO classes and the AO centers for $ErBr_3$ for $^4I_{15/2} \rightarrow {}^2H_{11/2}$. [a,b]

	m(Ln,Ln)	*m*(Br,Br)	*m*(Br,Ln)	*m*(Ln,Br)	Total
μ(occ, vir)	-3.7	***43.2*** [c]	**10.7** [d]	3.6 [e]	53.8
μ(vir, occ)	-2.8	***38.0*** [c]	**1.1** [e]	**0.0** [d]	36.4
μ(occ, act)	-0.1	2.7	**-0.2** [d]	0.4	2.9
μ(act, occ)	-0.2	1.9	0.1	**-0.3** [d]	1.5
μ(vir, act)	**0.4** [f]	1.7	**-0.3** [e]	-0.7	1.0
μ(act, vir)	**-1.0** [f]	2.3	-1.0	**-0.2** [e]	0.0
μ(vir, vir)	-0.1	-0.2	0.1	0.1	-0.1
μ(act, act)	**-3.3** [f]	8.2	-1.1	-1.6	2.2
μ(occ, occ)	0.0	2.1	0.1	0.1	2.3
Total	-11.0	99.8	9.7	1.5	100.0

Table A-10：Decomposition of TDM integrals (in percent) based on the MO classes and the AO centers for $ErBr_3$ for $^4I_{15/2} \rightarrow {}^4G_{11/2.}$ [a,b]

	m(Ln,Ln)	*m*(Br,Br)	*m*(Br,Ln)	*m*(Ln,Br)	Total
μ(occ, vir)	-3.8	***44.0*** [c]	**11.7** [d]	**3.9** [e]	55.9
μ(vir, occ)	-2.6	***37.2*** [c]	**1.0** [e]	**-0.7** [d]	34.9
μ(occ, act)	-0.2	3.5	**-0.3** [d]	0.3	3.3
μ(act, occ)	-0.1	1.1	0.1	**-0.2** [d]	0.9
μ(vir, act)	**0.3** [f]	1.9	**-0.3** [e]	-0.8	1.1
μ(act, vir)	**-1.2** [f]	2.4	-1.0	**-0.2** [e]	-0.1
μ(vir, vir)	-0.1	-0.3	0.1	0.2	-0.1
μ(act, act)	**-3.3** [f]	8.1	-1.1	-1.6	2.1
μ(occ, occ)	0.0	1.9	0.1	0.1	2.0
Total	-11.0	99.7	10.3	1.0	100.0

Table A-11：Decomposition of TDM integrals (in percent) based on the MO classes and the AO centers for $TmBr_3$ for $^3H_6 \rightarrow {}^3H_{4.}$ [a,b]

	m(Ln,Ln)	*m*(Br,Br)	*m*(Br,Ln)	*m*(Ln,Br)	Total
μ(occ, vir)	-2.0	***42.1*** [c]	**4.0** [d]	**2.3** [e]	46.5
μ(vir, occ)	-2.9	***41.3*** [c]	**1.6** [e]	**0.7** [d]	40.8
μ(occ, act)	0.2	2.4	**-0.2** [d]	0.4	2.8
μ(act, occ)	-0.5	3.0	0.1	**-0.5** [d]	2.1
μ(vir, act)	**0.3** [f]	2.0	**-0.3** [e]	-0.9	1.1
μ(act, vir)	**-0.7** [f]	2.5	-1.1	**-0.3** [e]	0.4
μ(vir, vir)	-0.1	-0.3	0.1	0.1	-0.1
μ(act, act)	**-3.8** [f]	12.1	-1.2	-2.7	4.4
μ(occ, occ)	-0.1	2.0	0.1	0.1	2.2
Total	-9.5	107.0	3.3	-0.8	100.0

Table A-12：Decomposition of TDM integrals (in percent) based on the MO classes and the AO centers for $TmBr_3$ for $^3H_6 \rightarrow {}^3F_4$. [a,b]

	m(Ln,Ln)	*m*(Br,Br)	*m*(Br,Ln)	*m*(Ln,Br)	Total
μ(occ, vir)	-2.2	***42.0*** [c]	**6.0** [d]	**2.7** [e]	48.5
μ(vir, occ)	-2.7	***39.0*** [c]	**1.3** [e]	**0.3** [d]	38.0
μ(occ, act)	0.2	4.3	**-0.4** [d]	0.3	4.4
μ(act, occ)	-0.6	2.9	0.1	**-0.5** [d]	1.9
μ(vir, act)	**0.3** [f]	1.8	**-0.3** [e]	-0.9	1.0
μ(act, vir)	**-1.1** [f]	2.5	-1.1	**-0.3** [e]	0.0
μ(vir, vir)	-0.2	-0.4	0.2	0.3	-0.1
μ(act, act)	**-3.6** [f]	10.8	-1.0	-2.3	3.8
μ(occ, occ)	-0.1	2.4	0.1	0.1	2.5
Total	-10.0	105.4	5.0	-0.4	100.0